

**Evolution of the Seismic Structure of the  
Incoming/Subducting Oceanic  
Nazca Plate off South Central Chile**

**Dissertation**

zur Erlangung des Doktorgrades  
der Mathematisch-Naturwissenschaftlichen Fakultät  
der Christian-Albrechts-Universität zu Kiel

vorgelegt von

**Eduardo Contreras-Reyes**

Kiel, 2008

Referent: PD. Dr. I. Grevemeyer  
Koreferent: Prof. Dr. W. Rabbel  
Tag der mündlichen Prüfung:

Zum Druck genehmigt: Kiel,

Der Dekan  
gez.





# Abstract

The release of fluids in subduction zones is believed to be an important process controlling earthquakes both in the downgoing plate and in the seismogenic megathrust fault zone. Depending on the depth of slab dehydration, water may nurture rupture propagation and trigger arc magmatism. Growing number of geophysical evidence suggest that alteration and hydration of the oceanic plate is most vigorous at the trench-outer rise, where extensional bending-related faulting affects the hydrogeology of the oceanic crust and mantle. To better understand the processes of hydration and alteration affecting the oceanic lithosphere prior to and during subduction, I have studied the seismic velocity structure of the oceanic Nazca plate offshore of southern central Chile.

A combination of swath bathymetric, wide-angle and reflection seismic data was used to derive 2D velocity-depth models, using joint refraction and reflection travel-time tomography along two main corridors: (i) offshore Isla de Chiloe ( $\sim 43^\circ\text{S}$ ) and (ii) southern Arauco peninsula ( $\sim 38^\circ\text{S}$ ). The study area corresponds to the southern central accretionary Chile margin, where the trench is heavily filled with up to 2.2 km of sediments. The velocity models show P-wave velocities typical for mature fast-spreading crust in the seaward section of the profiles, with uppermost mantle velocities as fast as 8.3-8.4 km/s. Approaching the Chile trench seismic velocities are significantly reduced, however, suggesting that the structure of both the oceanic crust and uppermost mantle have been altered, possibly due to a certain degree of fracturing and hydration. The decrease of the velocities roughly starts at the outer rise;  $\sim 100$  km from the deformation front, and continues into the trench.

Anomalously low heat flow values near outcropping basement highs were founded at the outer rise offshore Isla de Chiloe, suggesting an efficient inflow of cold seawater into the oceanic crust. Hydration and crustal cracks, activated by extensional tectonic stresses, are suggested to govern the reduced velocities in the vicinity of the trench. Considering typical flow distances of 50 km, water might be redistributed over most of the trench-outer rise area. In addition, Poisson's ratios at the lowermost crust and uppermost mantle reach values of  $\sim 0.26$  and  $\sim 0.29$ , respectively. These features can be explained by an oceanic crust partially weathered, altered and fractured. Relatively high Poisson's ratios in the

uppermost mantle may be likely related to partially serpentized mantle. On the other hand, the comparison of the uppermost mantle P-wave velocities at the crossing point between perpendicular profiles at  $\sim 43^\circ\text{S}$  ( $\sim 90$  km seaward from the trench axis) reveals a low degree of  $P_n$  anisotropy ( $< 2\%$ ).

Offshore southern Arauco peninsula, the Mocha Fracture Zone is obliquely subducting underneath the South American plate and coincides with an area of even slower velocities and thinning of the oceanic crust (10-15 % thinning), suggesting that the incoming fracture zone may enhance the flux of the chemically-bound water into the subduction zone. The low  $P_n$  velocities found in the outer rise area span along the subducting plate and reach a maximum depth of 6-8 km in the uppermost mantle, suggesting that as the oceanic plate subducts at the trench, bending and faulting continues to affect the oceanic lithosphere. The restoring to 'normal' mantle velocities of  $\sim 8.4$  km/s coincide with the 400-430°C isotherm. This depth is interpreted as the depth limit of hydro-alteration within the upper part of the oceanic lithosphere, where extensional stresses dominate.

# Zusammenfassung

Die Freisetzung von Fluiden in Subduktionszonen gilt als ein wichtiger Prozess, der die Erbenen sowohl in der abtauchenden Platte als auch in der seismogenen Megathrust-Bruchzone steuert. In Abhängigkeit von der Entwässerungstiefe der abtauchenden Platte kann Wasser die Ausbreitung von Brüchen fördern und Bogenmagmatismus auslösen. Geophysikalische Anzeichen legen zunehmend nahe, dass die stärkste Veränderung und Hydratation der ozeanischen Platte im Tiefseeegraben-Outer Rise vorkommt, wo ausdehnende Biegungsbrüche die Hydrogeologie von ozeanischer Kruste und Mantel beeinflussen. Um die Hydrations- und Veränderungsprozesse, die die ozeanische Lithosphäre beeinflussen, vor und während der Subduktion besser zu verstehen, habe ich die Geschwindigkeitsstruktur der ozeanischen Nazca-Platte vor Süd-Zentral-Chile untersucht.

Eine Kombination von Fächerecholot-Bathymetrie und seismischen Weitwinkel- und Reflexionsdaten wurde verwendet, um 2D-Geschwindigkeitsmodelle unter Benutzung von gemeinsamer Refraktions- und Reflexionslaufzeit-tomographie entlang zweier Hauptkorridore, (i) vor der Chiloe Insel ( $\sim 43^\circ\text{S}$ ) und (ii) vor der südlichen Arauco-Halbinsel ( $\sim 38^\circ\text{S}$ ) herzuleiten. Das Arbeitsgebiet entspricht dem südlichen zentralen akkretionären Chile Margin, wo der Tiefseeegraben mit bis zu 2,2 km mächtigen Sedimenten gefüllt ist. Die Geschwindigkeitsmodelle zeigen P-Wellengeschwindigkeiten typisch für vollentwickelte schnell-spreizende Kruste in der seewärtigen Sektion der Profile, von bis zu 8,3-8,4 km/s im oberen Mantel. Zum Chile-Tiefseeegraben hin sind die seismischen Geschwindigkeiten jedoch erheblich reduziert, was auf eine veränderte Struktur sowohl der ozeanischen Kruste als auch des oberen Mantels hinweist, möglicherweise durch einen bestimmten Grad der Zerklüftung und Hydratation hervorgerufen. Die Abnahme der Geschwindigkeiten beginnt grob am Outer Rise  $\sim 100$  km vor der Deformationsfront und setzt sich bis in den Tiefseeegraben fort.

Ungewöhnlich niedrige Wärmestromwerte in der Nähe von anstehendem Krustengestein wurden am Outer Rise vor Chiloe Insel gefunden, was auf ein effizientes Einströmen von kaltem Meerwasser in die ozeanische Kruste hinweist. Hydratation und durch tektonischen Dehnungsspannung hervorgerufene Krustenrisse werden als Ursache für die reduzierten

Geschwindigkeiten in der Umgebung des Tiefseegrabens angesehen. Mit typischen Ausbreitungsdistanzen von 50 km kann Wasser über den Großteil des Gebiets vom Tiefsee graben-Outer Rise umverteilt werden. Außerdem erreichen die Poisson-Zahlen in der untersten Kruste und im oberen Mantel Werte von  $\sim 0,26$  bzw.  $\sim 0,29$ . Diese Merkmale können durch teilweise verwitterte, veränderte und zurklüftete ozeanische Kruste erklärt werden. Relativ hohe Poisson-Zahlen im oberen Mantel können wahrscheinlich mit einem teilweise serpentinisierten Mantel in Beziehung gesetzt werden. Auf der anderen Seite zeigt ein Vergleich der oberen Mantelgeschwindigkeiten an den Kreuzprofilen bei  $\sim 43^\circ\text{S}$  ( $\sim 90$  km seewärts von der Tiefsee grabenachse) einen geringen Grad von  $P_n$ -Anisotropie ( $< 2\%$ ).

Vor der südlichen Arauco-Halbinsel subduziert die Mocha-Bruchzone schräg unter die südamerikanische Platte und überschneidet sich mit einem Gebiet von noch langsameren Geschwindigkeiten und verdünnter ozeanische Kruste (10-15% dünner), was darauf hinweist, dass die hereinkommende Bruchzone den Fluss von chemisch gebundenem Wasser in die Subduktionszone verstärkt. Die niedrigen  $P_n$ -Geschwindigkeiten am Outer Rise breiten sich entlang der subduzierenden Platte aus und erreichen eine Maximaltiefe von 6-8 km im obersten Mantel, was anzeigt, dass während die ozeanische Platte am Tiefsee graben subduziert das Biegen und Brechen weiter fortschreitet und die ozeanische Lithosphäre beeinflusst. Das Zurücksetzen zu 'normalen' Mantelgeschwindigkeiten auf  $\sim 8,4$  km/s fällt mit der  $400-430^\circ\text{C}$ -Isotherme zusammen. Diese Tiefe wird als die untere Grenze der Hydroverwitterung des oberen Teils der ozeanischen Lithosphäre interpretiert, wo Dehnungsspannungen vorherrschen.



# Resumen

Se piensa que la deshidratación de la placa oceánica durante subducción es un importante proceso que controla terremotos tanto en la placa subductante como en la zona sísmogénica. Dependiendo de la profundidad de deshidratación de la placa subductante, agua expulsada puede gatillar ruptura e inducir arco magmatismo. Recientes estudios geofísicos en zonas de subducción sugieren que procesos de alteración e hidratación afectando la placa oceánica son más vigorosos en el outer rise, donde procesos de fallamiento inducidos por la flexión de la placa afectan la hidrogeología de la corteza y el manto oceánico. Con el objeto de entender mejor los procesos de evolución de la litosfera oceánica antes y durante su subducción, he estudiado la estructura sísmica de la placa oceánica de Nazca en la costa del sur-centro de Chile.

Datos batimétricos, sísmicos de refracción de gran ángulo y reflexión fueron combinados para obtener modelos bi-dimensionales de velocidad y profundidad a través de una inversión conjunta de tiempos de llegadas de refracciones y reflexiones a lo largo de dos perfiles: (i) en la costa de la Isla de Chiloé ( $\sim 43^\circ\text{S}$ ) y (ii) en la costa sur de la península de Arauco ( $\sim 38^\circ\text{S}$ ). El área de estudio corresponde al margen acrecionario del sur-centro de Chile, donde la fosa está pesadamente llenada con un máximo espesor de 2,2 km de sedimentos. En la parte occidental del perfil, el modelo de velocidad muestra que las velocidades de onda P son características de una corteza oceánica generada en una dorsal con rápida tasa de expansión, en donde las velocidades del manto superior son tan rápidas como 8,3-8,4 km/s. Sin embargo, más próximo a la fosa, una significativa reducción de velocidades sísmicas es observada, lo cual sugiere que la estructura de la corteza y el manto oceánico han sido alterada, lo cual es posiblemente debido a un cierto grado de fracturamiento e hidratación. La reducción de velocidades empieza aproximadamente en el outer rise,  $\sim 100$  km mar adentro del frente de deformación, y se expande hacia la fosa.

Bajas y anómalas medidas de flujo calórico cerca de un alto de basamento fueron encontradas en el outer rise en la costa de la Isla de Chiloé, lo cual sugiere una eficiente infiltración de agua fría dentro de la corteza oceánica. Las bajas velocidades encontradas en la vecindad de la fosa son interpretadas como procesos de hidratación y activación

de fisuras corticales debido al fallamiento asociado a la flexión de la placa. Agua podría estar siendo re-distribuida en la mayor parte de la región del trench-outer rise si se consideran típicas distancias de circulación hidrotermal dentro de la corteza superior ( $\sim 50$  km). Además, razones de Poisson en el fondo de la corteza inferior y borde superior del manto alcanzan valores de  $\sim 0,26$  y  $\sim 0,29$ , respectivamente. Estos valores pueden ser explicados como el resultado de una corteza oceánica considerablemente hidratada, alterada y fracturada. Relativas altas razones de Poisson en el manto superior reflejan que este podría estar parcialmente serpentizado. Por otra parte, la comparación de ondas P de velocidades en el manto superior entre dos perfiles sísmicos perpendiculares localizados a  $\sim 43^\circ\text{S}$  ( $\sim 90$  km mar adentro de la fosa) revela un bajo grado de anisotropía del manto superior ( $< 2\%$ ).

En la costa sur de la península de Arauco, la zona de fractura Mocha se encuentra oblicuamente subduciendo bajo la placa Sudamericana y coincide con un área de velocidades sísmicas aún más bajas y un adelgazamiento de la corteza oceánica (10-15 % de adelgazamiento), lo cual sugiere que la presencia de la zona de fractura podría aumentar la cantidad de fluidos que son transportados hacia la zona de subducción. Bajas velocidades en el manto superior fueron encontradas en el área del outer rise y también a lo largo de la placa subductante con una profundidad máxima de 6-8 km en el manto superior. Esto sugiere que procesos de flexión y fallamiento continúan afectando la placa oceánica, la cual ya fue debilitada y alterada antes de empezar a subducir. La restauración de velocidades "normales" en el manto ( $\sim 8,4$  km/s) es alcanzada a una profundidad que coincide con la isoterma de  $400-430^\circ\text{C}$ . Esta máxima profundidad es interpretada como la profundidad límite del frente de hidro-alteración dentro de la parte superior de la litosfera oceánica, la cual es dominada por un régimen extensional de estreses.

# Contents

<b>Abstract</b>	<b>v</b>
<b>Zusammenfassung</b>	<b>vii</b>
<b>Resumen</b>	<b>ix</b>
<b>1 Introduction</b>	<b>9</b>
1.1 Outline and objectives of the thesis . . . . .	11
1.2 Regional plate tectonics . . . . .	15
1.3 Southern central Chile: a heavily sedimented margin . . . . .	17
<b>2 Alteration of the subducting oceanic lithosphere at the southern central Chile trench-outer rise</b>	<b>19</b>
2.1 Introduction . . . . .	20
2.2 Tectonic setting . . . . .	22
2.3 Seismic data . . . . .	24
2.4 Travel time tomography scheme . . . . .	26
2.4.1 Sedimentary section tomography . . . . .	29
2.4.2 Oceanic crust tomography . . . . .	31
2.4.3 Upper mantle tomography . . . . .	34
2.5 Discussion . . . . .	38
2.5.1 Seismic structure of the oceanic lithosphere . . . . .	38
2.5.2 Water pathways . . . . .	40
2.5.3 Volatiles stored in the oceanic subducting lithosphere . . . . .	43
2.6 Conclusions . . . . .	44
<b>3 Effect of bending-related faulting on seismic Poisson's ratio and mantle anisotropy: a case study offshore of southern central Chile</b>	<b>47</b>
3.1 Introduction . . . . .	48
3.2 Tectonic setting . . . . .	50
3.3 Wide angle seismic data . . . . .	50

3.4	P-wave travel time modelling scheme . . . . .	52
3.4.1	Oceanic crust tomography . . . . .	55
3.4.2	$P_n$ travel-time tomography . . . . .	57
3.5	S-wave travel time modelling scheme . . . . .	58
3.6	Poisson's ratio . . . . .	61
3.7	Results and Discussion . . . . .	61
3.7.1	Seismic structure of the oceanic lithosphere . . . . .	61
3.7.2	Hydrothermal activity at the southern central Chile outer rise . . .	66
3.7.3	$P_n$ anisotropy at the outer rise . . . . .	66
3.7.4	Conclusions . . . . .	69
<b>4</b>	<b>Seismic structure of the incoming/subducting oceanic Nazca plate off-shore the southern Arauco Peninsula, Chile at <math>\sim 38^\circ</math> S</b>	<b>71</b>
4.1	Introduction . . . . .	72
4.2	Geodynamic setting . . . . .	73
4.3	Seismic reflection and bathymetric data . . . . .	74
4.3.1	The trench-outer rise area . . . . .	77
4.4	Wide-angle seismic data . . . . .	78
4.5	Travel-time tomography scheme . . . . .	83
4.5.1	Reference model and inversion parameters . . . . .	84
4.5.2	Final and uncertainty velocity models . . . . .	85
4.5.3	Resolution test . . . . .	88
4.6	Results and Discussion . . . . .	89
4.6.1	Alteration of the oceanic crust . . . . .	89
4.6.2	Alteration of the oceanic mantle prior to subduction . . . . .	90
4.6.3	Hydro-alteration processes affecting the subducting oceanic lithosphere . . . . .	91
4.6.4	The role of the Mocha FZ . . . . .	92
4.7	Conclusions . . . . .	93
<b>5</b>	<b>Conclusions and Outlook</b>	<b>95</b>
5.1	Discussion and Conclusions . . . . .	95
5.2	Outlook . . . . .	98
<b>A</b>	<b>Monte Carlo Test</b>	<b>101</b>
<b>B</b>	<b><math>S_n</math> Traveltime sensitivity</b>	<b>103</b>
<b>C</b>	<b>Amplitude Modelling</b>	<b>105</b>

<b>D Structure of the accretionary convergent margin offshore of southern Arauco Peninsula, Chile at <math>\sim 38^\circ</math> S</b>	<b>107</b>
D.1 Introduction . . . . .	107
D.2 Characterization of geological structures from seismic reflection and bathymetric data . . . . .	109
D.2.1 The frontal accretionary prism . . . . .	109
D.2.2 The forearc basin . . . . .	109
D.3 Results and Discussion . . . . .	110
D.3.1 Seismic segmentation of the accretionary margin . . . . .	110
D.3.2 Subduction of sediments - the subduction channel . . . . .	114
D.3.3 Comparison with the northern erosional Chile margin . . . . .	114
D.4 Summary . . . . .	116
<b>Bibliography</b>	<b>117</b>



# List of Figures

1.1	The TIPTEQ Experiment . . . . .	13
1.2	Geodynamic setting . . . . .	16
1.3	Age of the oceanic Nazca plate . . . . .	17
1.4	The Chile trench . . . . .	18
2.1	Tectonic Setting . . . . .	23
2.2	Seismic profile P05 . . . . .	24
2.3	OBH 68 and 11 . . . . .	26
2.4	OBH 60 and 48 . . . . .	27
2.5	OBH 40 . . . . .	28
2.6	Sedimentary tomographic inversion . . . . .	30
2.7	Crustal tomographic inversion . . . . .	33
2.8	Resolution test . . . . .	34
2.9	Mantle tomographic inversion . . . . .	35
2.10	Detailed forward analysis . . . . .	37
2.11	Heat flow model . . . . .	42
3.1	Tectonic Setting offshore Isla de Chiloe . . . . .	51
3.2	OBH 17 and 13 . . . . .	53
3.3	OBS 02 and 03 (hydrophone component) . . . . .	54
3.4	Final P-wave velocity models (STA 1) . . . . .	57
3.5	Final S-wave velocity and Poisson's ratio models . . . . .	60
3.6	$V_p - V_s$ graphic . . . . .	64
3.7	High-resolution bathymetric image of the trench-outer rise area ( $\sim 43^\circ\text{S}$ ) . . . . .	67
4.1	Location of seismic profiles . . . . .	75
4.2	Seismic profile P09 . . . . .	76
4.3	Seismic reflection data (trench outer-rise area) . . . . .	78
4.4	Seismic wide-angle data (OBH 250 and 230) . . . . .	80
4.5	Seismic wide-angle data (OBH 45 and 38) . . . . .	81

4.6	Seismic wide-angle data (OBS 28) . . . . .	82
4.7	Velocity-Depth Model (Corridor 1) . . . . .	86
4.8	Uncertainty models (Corridor 1) . . . . .	87
4.9	Resolution test (Corridor 1) . . . . .	89
A.1	Velocity reference models (STA1) . . . . .	102
B.1	Detailed forward analysis of $S_n$ travel time . . . . .	104
C.1	1D P- and S-wave models determined from the amplitude analysis . . . . .	106
C.2	Synthetic seismograms OBS 03 (Hydrophone component) . . . . .	106
D.1	The forearc basin and frontal prism offshore Arauco peninsula . . . . .	111
D.2	Seismic segmentation of the southern central Chile margin . . . . .	113
D.3	Accretion v/s Erosion off Chile . . . . .	115



# List of Tables

3.1	Summary of arrivals time picks (STA 1) . . . . .	56
3.2	Results of P-wave crustal velocity inversion (STA 1) . . . . .	58
3.3	Results of $P_n$ velocity inversion (STA 1) . . . . .	58
3.4	Results of S-wave velocity inversion (STA 1) . . . . .	59
4.1	Summary of arrivals time picks (Corridor 1) . . . . .	88
5.1	Degree of serpentinization for different subduction zones. . . . .	96



# Chapter 1

## Introduction

The release of fluids from the oceanic subducting slab has been inferred both to trigger the formation of magmatic arcs [Gill, 1981; Ulmer and Trommsdorff, 1995] and to induce intraslab intermediate-depth earthquakes [Peacock, 2001; Tibi et al., 2002]. Dewatering of subducting sediments leads to hydration of the mantle wedge at depths  $< 20$  km [ANCORP Working Group, 1999, Ruepke et al., 2004]. Metamorphic dehydration processes of the subducting oceanic crust increase pore pressure and decrease effective confining pressure, thereby promoting intraslab seismicity ( $\sim 60$ -80 km depth) [Peacock, 2001; Hacker et al., 2003]. Similarly, at depths  $> 100$  km, the subducting lithospheric mantle dehydrates [Ruepke et al., 2004] and trigger intraplate seismicity [Yuan et al., 2000; Peacock, 2001]. Typically at these depths ( $\sim 100$  km) the released fluids cause partial melting and lead to arc volcanism [Ruepke et al., 2004]. In this regard, the amount of volatiles stored within the subducting oceanic lithosphere play a crucial role on the subduction zone water cycle.

The amount of fluids stored within the incoming/subducting oceanic plate is linked to the processes of hydration and alteration experienced during its lifetime (before subduction). Hydration and alteration commence at the genesis of the oceanic lithosphere at the mid-ocean ridge. Oceanic lithosphere created at slow spreading centres is characterized by an oceanic crust and uppermost mantle pervasively fractured and hydrated [e.g., Carbotte and Scheirer, 2004]. In contrast, oceanic lithosphere created at moderate to fast spreading mid-ocean ridges, such as most of the oceanic plates consumed at Circumpacific subduction zones, are characterized by pervasive fracturing and hydrothermal activity largely confined to upper crustal levels [e.g., Carbotte and Scheirer, 2004; Karson, 1998]. Lower crust and mantle rocks are therefore relatively dry and undeformed. However, growing number of observational evidence suggest that this condition of relative "dry" and "undeformed" oceanic lithosphere can be dramatically perturbed at the outer rise seaward of a trench [Peacock, 1990; Ranero et al., 2003; Grevemeyer et al., 2007]. These authors have suggested that much of the hydration will occur at the trench-outer rise area, when

reactivated shallow faults and new faults, grow to penetrate across the crust into the upper mantle.

The outer rise is formed when the oceanic lithosphere approaches a subduction zone and bends upwards by the plate stresses, thus a prominent outer bulge seaward of the trench axis is formed. The bending of the plate is associated with tension in the upper part of the lithosphere, where outer rise earthquakes, caused by tensional failure induced by the bending of the oceanic plate are common [Chapple and Forsyth, 1979; Clouard *et al.*, 2007; Lefeldt and Grevenmeyer, 2008]. Most of the near-trench intraplate earthquakes show normal-fault focal mechanisms, consistent with mapped bending-related normal faults [Ranero *et al.*, 2005]. Outer rise earthquakes are possibly linked to the rupture of the upper oceanic lithosphere [Kanamori, 1971; Christensen and Ruff, 1983], creating a pervasive tectonic fabric of horst-and-graben structures that may cut across the crust [e.g., Masson, 1991], penetrating deep into the uppermost mantle [Ranero *et al.*, 2003]. This process may lead to a large scale formation of serpentinite in the upper mantle of the downgoing plate [Peacock, 1990; Ranero *et al.*, 2003]. Hydration of the mantle lithosphere at the outer rise can, potentially, more than double the amount of water carried by the downgoing slab [Ruepke *et al.*, 2004]. Ranero *et al.* [2003; 2005], and Ranero and Sallares [2004] have suggested that the isotherm of 600°C (the depth limit of the brittle lithosphere) corresponds to a good proxy for the maximum depth of mantle's alteration. However, this depth as a limit for the lithospheric hydro-alteration has not yet been constrained by active seismic studies. Estimating the maximum depth of hydro-alteration is important to quantify the water input into the subduction zone, and hence its impact on intra-slab seismicity and arc magmatism.

The percolation of large amounts of fluids alter dramatically the chemical composition and seismic structure of the oceanic lithosphere. According to Christensen, [1996], dry peridotite rocks have typical seismic velocities faster than 8.2 km/s at 200 MPa (typical Moho depths), with increasing degree of serpentinization seismic velocities are forced to change to  $\sim 4.7$  km/s in serpentinite. Partially serpentinized peridotites have seismic velocities that fall between these limiting values. Usually, in-situ measurements of seismic velocities through wide-angle seismic experiments do not represent a direct quantification of the degree of hydration. This is due to the fact that the increase of fracture porosity of the oceanic lithosphere also change considerably its seismic structure. Fracturing and hydration are processes acting simultaneously and it might be difficult to separate their effects on seismic properties. Nevertheless, measuring of anomalously low seismic velocities in subduction zones provides crucial information for hydro-alteration processes within the oceanic lithosphere, and provides an upper bound for the degree of hydration.

In addition, mapping of the spatial distribution of the low velocity zones provides important information regarding the processes which lead to hydro-alteration of the oceanic lithosphere.

## 1.1 Outline and objectives of the thesis

This dissertation focuses on the study of the evolution of seismic properties of the oceanic Nazca plate prior to and during subduction offshore of southern central Chile. This region hosted the greatest ever recorded 1960 Chilean earthquake ( $M_w=9.5$ ) [Cifuentes *et al.*, 1989; Barrientos and Ward, 1990; Cisternas *et al.*, 2005], which propagated for more than 900 km starting at  $\sim 38^\circ\text{S}$  and stopping at  $\sim 46^\circ\text{S}$  (Figure 1.1). In this region, seismic data were acquired on board of the German vessel R/V Sonne during the course of the TIPTEQ (from The Incoming Plate to mega-Thrust EarthQuakes process) project [Schervath *et al.*, 2006a]. The seismic refraction experiment consists of five major corridors (Figure 1.1). All transects were covered with seismic wide-angle refraction, vertical incidence reflection data, and the northern four transects also featured with heat flow measurements either on or near the lines. In addition, the seafloor was mapped throughout the entire survey area using a multibeam system [Schervath *et al.*, 2006a]. For the propose of this thesis, the two northernmost corridors were processed in order to characterize the seismic structure of the oceanic Nazca plate (see Figure 1.1 for location). A combined analysis of seismic reflection and wide-angle and refraction data was applied to derive 2D velocity models using joint refraction and reflection travel-time tomography [Korenaga *et al.*, 2000].

In chapter 2, I studied the seismic structure of the incoming Nazca plate prior to subduction offshore Isla de Chiloe (corridor 2 in Figure 1.1). Here, the trench is filled with up to  $\sim 2.2$  km of sediments and the plate age at the trench axis is  $\sim 14.5$  Ma [Tebbens *et al.*, 1997]. Turbidites fill the whole trench basin and flow seaward up to  $\sim 200$  km from the trench axis. Thus the top of the igneous crust in the trench-outer rise area is well covered by sediments. Sediment thickness on top of the igneous oceanic crust is believed to be an important parameter controlling the local hydrogeological regime of the oceanic lithosphere. The sedimentary cover is though to limit seawater from communicating with the underlying oceanic crust and thus limit hydration. However, Fisher *et al.*, [2003b] demonstrated that circulation through basement outcrops separated up to 50 km can be sustained. In this chapter, I studied the interrelationship between sedimentary cover and hydration. To achieve this, I have integrated seismic refraction and wide-angle data, complemented by seismic reflection imaging of sediments together with heat flow data in order to study the hydrothermal activity and its impact on seismic velocities at the trench-outer

rise area.

An additional key parameter for understanding hydration and faulting mechanisms is the Poisson's ratio. Offshore Isla de Chiloe, a short term array (STA1) composed by a series of short wide-angle seismic profiles was installed at the outer rise (Figure 1.1). Here, P- and S-waves of excellent quality were recorded, additionally providing the opportunity to map the Poisson's ratio structure of the oceanic lithosphere. I performed two independent P- and S-waves travel time tomographies to construct a 2D Poisson's ratio model at the outer-rise region. The results are presented in chapter 3, and are discussed in terms of cracks and hydration mechanisms. In addition, seismic information recorded along two perpendicular crossing wide-angle profiles provide the opportunity to study seismic mantle anisotropy in the outer rise region. These results are compared with measurements obtained by refractions experiments performed seaward from the outer rise area.

In chapter 4, I present a 2D velocity model along corridor 1 (Figure 1.1). The seismic stations sited on the seaward section of the profile were deployed during the course of the TIPTEQ project. In order to study the seismic structure of the oceanic Nazca plate during subduction, I have extended the velocity model landward of the trench (up to the coast) using seismic data acquired during the course of the SPOC (Subduction Process Off Chile) project. Some stations sited on the continental shelf recorded mantle refractions of long offsets ( $>100$  km) imaging the subducting oceanic mantle. This data set provides information regarding the depth limit of the hydro-alteration front within the oceanic lithosphere. These results are crucial to assess the amount of water carried for the downgoing slab to the deeper subduction zone, and the impact of the incoming lithosphere on seismogenesis.

In chapter 5, I discussed and summarized the main results of the dissertation. In addition, the results of this thesis are compared with other seismic studies carried out in the outer-rise areas offshore northern and central Chile and middle America. This thesis work also left several open issues that should be addressed in the future throughout new studies, as proposed in the outlook of this dissertation.

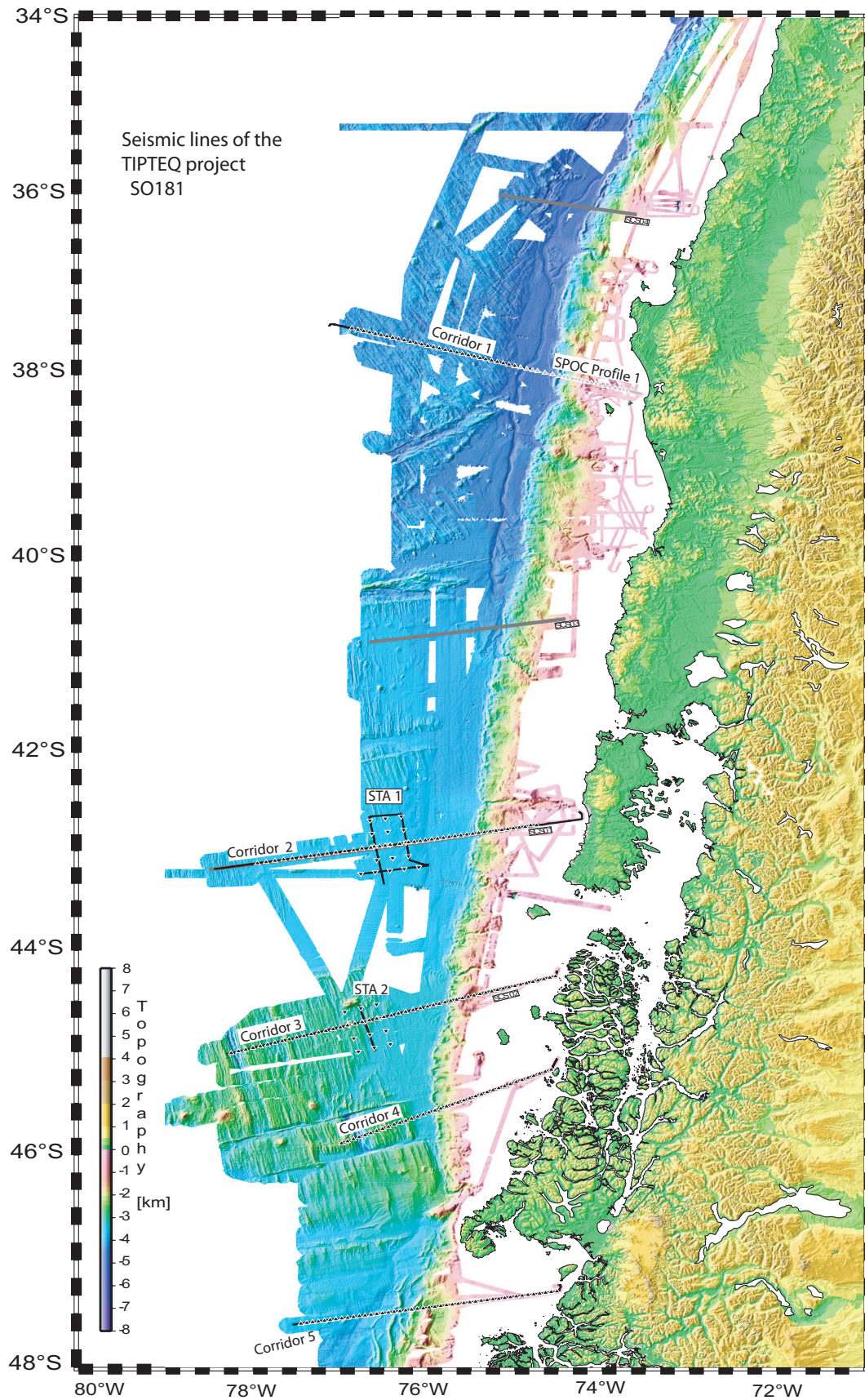


Figure 1.1: Map of TIPTEQ working area with all new TIPTEQ corridors plus the 2001 SPOC profile. High resolution bathymetry of the area were acquired during TIPTEQ and SPOC cruises, and from Bourgois et al., [2000].

The chapters 2-4 have been written as stand-alone scientific papers. Chapters 2 and 3 are already published in *Geochemistry, Geophysics, Geosystems (G-cubed)* <sup>1</sup> and in *Geophysical Journal International* <sup>2</sup>, respectively. In chapter 4, the results along corridor 1 regarding to the oceanic lithosphere are presented and were extracted from a third paper entitled "Upper lithospheric structure of the subduction zone offshore southern Arauco Peninsula, Chile at  $\sim 38^{\circ}S$ " <sup>3</sup>, which was accepted in April, 2008 in *Journal of Geophysical Research*. This paper shows additionally the seismic results of the southern central Chile continental margin, which are presented in the Appendix D.

---

<sup>1</sup>Contreras-Reyes, E., I. Grevemeyer, E. R. Flueh, M. Scherwath, and M. Heesemann (2007), Alteration of the subducting oceanic lithosphere at the southern central Chile trench-outer rise, *Geochem. Geophys. Geosyst.*, 8, Q07003, doi:10.1029/2007GC001632.

<sup>2</sup>Contreras-Reyes, E., I. Grevemeyer, E. R. Flueh, M. Scherwath, and J. Bialas (2008), Effect of trench-outer rise bending-related faulting on seismic Poisson's ratio and mantle anisotropy: a case study offshore of southern central Chile, *Geophys. J. Int.*, 173, 142-156.

<sup>3</sup>Contreras-Reyes, E., I. Grevemeyer, E. R. Flueh, and C. Reichert (2008), Upper lithospheric structure of the subduction zone offshore southern Arauco Peninsula, Chile at  $\sim 38^{\circ}S$ , *J. Geophys. Res.*, doi:10.1029/2007JB005569, in press.



## 1.2 Regional plate tectonics

The oceanic Nazca plate currently subducts at  $\sim 6.6$  cm/yr beneath South America with a relatively high convergence azimuth of  $\sim 78^\circ\text{E}$  [Angermann *et al.*, 1999]. Nazca plate was formed at two different spreading centers: north of the Valdivia Fracture Zone (FZ) the oceanic lithosphere was formed at the Pacific-Farallon spreading center more than 20 Myr ago [Mueller *et al.*, 1997], whereas south of the Valdivia FZ it was created at the Chile Rise within the past 20 Ma [Herron, 1981] (Figure 1.3). The boundaries of the two parts of the Nazca plate are defined by the onset of the Mocha FZ in the north and the Valdivia FZ in the south. Mocha FZ is currently obliquely subducting at  $\sim 38^\circ\text{S}$  (Figure 1.2), and corresponds roughly to the northern limit of the rupture area of the largest ever recorded 1960 Chile earthquake [Cifuentes, 1990]. The age of the oceanic Nazca plate [Tebbens and Cande., 1997; Mueller *et al.*, 1997] along the Peru-Chile trench increases from 0 Ma at the Chile Triple Junction (CTJ) with the Antarctic and South American plates ( $\sim 46.4^\circ\text{S}$ ) to a maximum of  $\sim 48$  Ma around  $20^\circ\text{S}$  (Figure 1.3). North of this latitude, the continental margin changes its orientation from NNE to NW, a feature known as the Arica bend. Further to the north, the plate age decreases along the trench up to  $\sim 28$  Ma at  $5^\circ\text{S}$ .

Fracture zones cut the Chile Rise into several segments (Figure 1.2), resulting in abrupt changes of thermal states along the plate boundary. These segments bounded by these FZs are roughly parallel to the trench strike (Figure 1.2). The Antarctic plate moves at  $\sim 1.8$  cm/yr and it is fairly perpendicular to the trench between  $\sim 46$  and  $53^\circ\text{S}$ , but south of this, it is quite oblique to the margin [DeMets *et al.*, 1990]. The CTJ is moving northward [Cande and Leslie, 1986], and volcanism along the austral Andes south of the Triple Junction is less active than in the northern segment but extends essentially to the tip of South America.

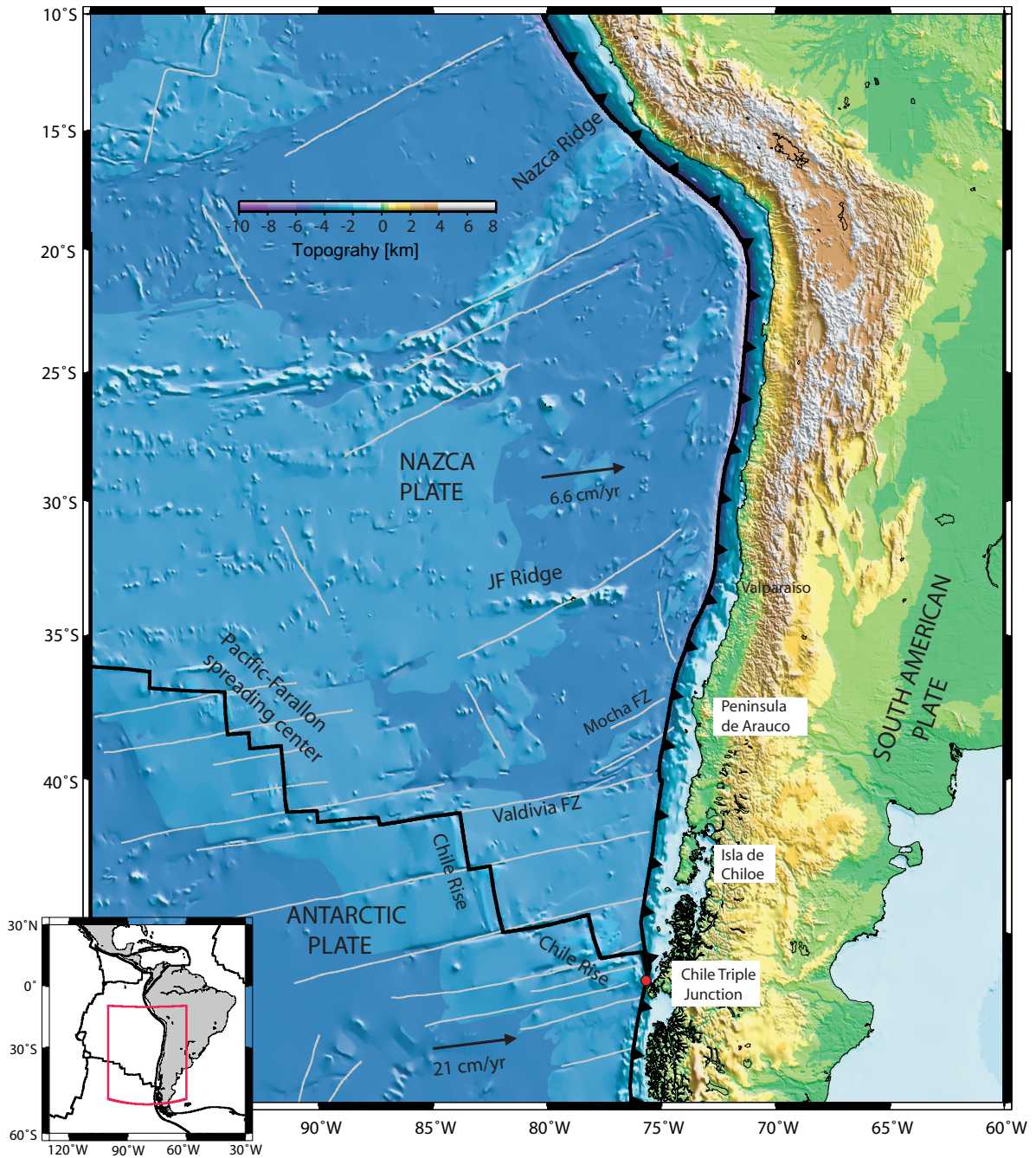


Figure 1.2: Geodynamic setting of Nazca, Antarctic, and South American plates. These plates join at the Chile Triple Junction (CTJ), where the Chile Rise is currently subducting at  $\sim 46.4^\circ\text{S}$ . The oceanic Nazca plate is segmented by several fracture zones (FZs), resulting in a strong variability of the age of the subducting plate. The heavily sedimented south-central Chilean trench is confined between two main oceanic features: the Juan Fernandez Ridge and the Chile Rise.

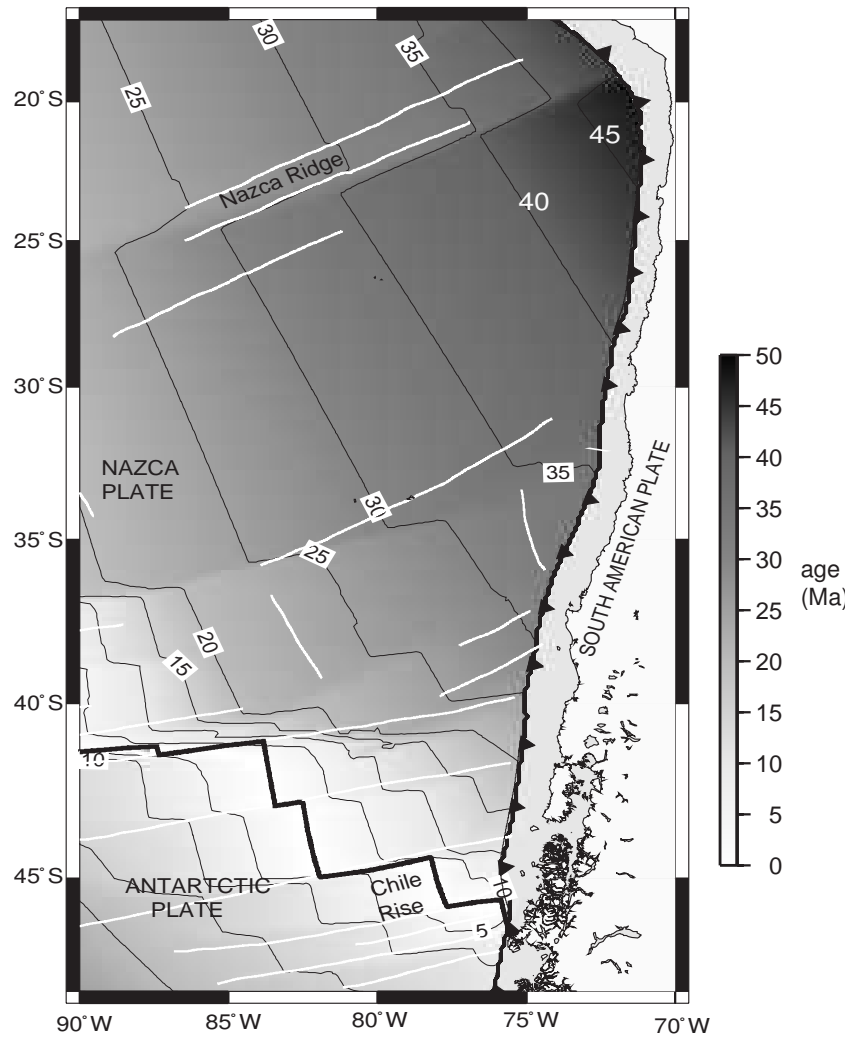


Figure 1.3: Black contour lines in the offshore region are isochrones of the oceanic Nazca plate [Mueller *et al.*, 1997] with ages in million of years.

### 1.3 Southern central Chile: a heavily sedimented margin

The southern central Chile trench between 34°S and 45.5°S is a heavily sedimented, the result of sediments delivered by the rivers and rapid glaciation denudation of the Andes [Thornburg *et al.*, 1990; Bangs and Cande, 1997; Bourgois, 2000]. Sediment transport from the continent to the trench is controlled by submarine landslides, submarine canyons, and turbidity currents [Voelker *et al.*, 2006]. Within the trench, turbidites migrate to the north as the seafloor depth becomes deeper with the plate age (Figure 1.3). Figure 1.4 shows the depths of the seafloor and top of the oceanic basement at the Chile trench axis between 20° and 48°S. The seafloor is only 3 km-depth in the vicinity of the incoming Chile Rise, where the plate age is 0 Ma. Here, the trench fill is almost devoid of sediments, which is explained by the migration of the sediments towards the south and north due

to topographic gradients of the oceanic basement. As the oceanic plate becomes older to the north, seafloor depth increase rapidly reaching a depth of  $\sim 3.5$  km at  $33^\circ\text{S}$  and  $\sim 5.8$  km at  $33^\circ\text{S}$  (Figure 1.4). The trench fill thickness between  $34^\circ$  and  $\sim 45^\circ\text{S}$  ranges between 1.5 and 2.5 km, while north of the Juan Fernandez Ridge (JFR) sedimentary thickness is only about 0.4-0.5 km [von Huene *et al.*, 1997]. Further northward, the trench deepens progressively to 8 km off Antofagasta at  $\sim 22^\circ\text{S}$  and has little sediment fill (Figure 1.4). The JFR behaves like a barrier for trench turbidites transport separating a sediment-starved trench axis to the north from a sediment-flooded axis to the south [Flueh *et al.*, 1998; von Huene *et al.*, 1997]. The shallow and buoyant Chile Rise "displaces" sediments to the north, confining thus between these two main oceanic features a thick sedimentary cover along the southern central Chile trench (Figure 1.4).

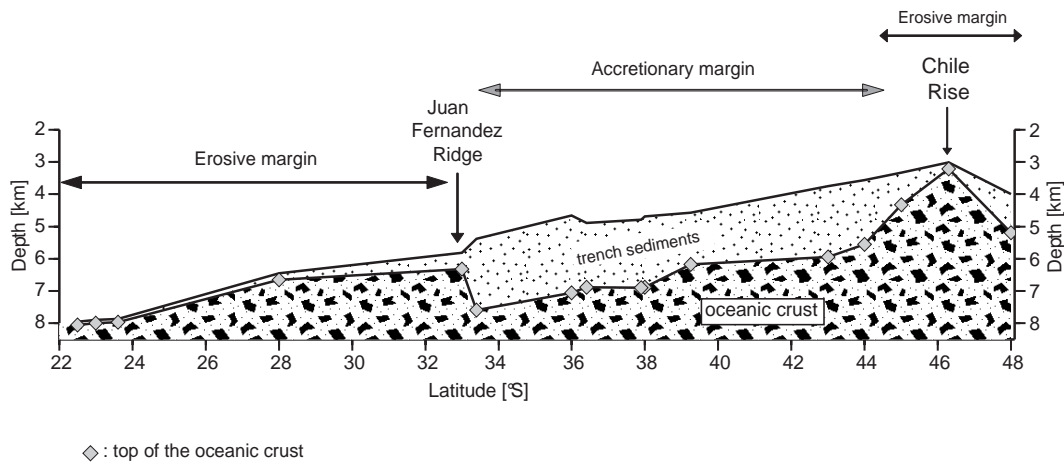


Figure 1.4: The seafloor depth was taken from the high resolution bathymetry data. Trench fill thicknesses were taken from [von Huene and Ranero, 2003] in north Chile, [von Huene *et al.*, 1997; Flueh *et al.*, 1998] in central Chile, [Diaz-Naveas, 1999; Scherwath *et al.*, 2006a, Voelker *et al.*, 2006] in south-central Chile, and [Burgois *et al.*, 2000] in south Chile.

## Chapter 2

# Alteration of the subducting oceanic lithosphere at the southern central Chile trench-outer rise

Hydrothermal circulation and brittle faulting processes affecting the oceanic lithosphere are usually confined to the upper crust for oceanic lithosphere created at intermediate to fast spreading rates. Lower crust and mantle rocks are therefore relatively dry and undeformed. However, recent studies at subduction zones suggest that hydration of the oceanic plate is most vigorous at the trench-outer rise where extensional bending-faulting affects the hydrogeology of the oceanic crust and mantle. To understand the degree of hydration, we studied the seismic velocity structure of the incoming Nazca plate offshore of southern central Chile ( $\sim 43^{\circ}\text{S}$ ); here the deep-sea trench is heavily filled with up to 2 km of sediments. Seismic refraction and wide-angle data, complemented by seismic reflection imaging of sediments, are used to derive a 2D velocity model using joint refraction and reflection travel time tomography. The seismic profile runs perpendicular to the spreading ridge and trench axes. The velocity model derived from the tomography inversion consists of a  $\sim 5.3\text{-km}$  thick oceanic crust and shows P-wave velocities typical for mature fast-spreading crust in the seaward section of the profile, with uppermost mantle velocities as fast as  $\sim 8.3\text{ km/s}$ . Approaching the Chile trench seismic velocities are significantly reduced, however, suggesting that the structure of both the oceanic crust and uppermost mantle have been altered, possibly due to a certain degree of fracturing and hydration. The decrease of the velocities roughly starts at the outer rise;  $\sim 120\text{ km}$  from the deformation front, and continues into the trench. Even though the trench is filled with sediment, basement outcrops in the outer rise frequently pierce the sedimentary blanket.

Anomalously low heat flow values near outcropping basement highs indicate an efficient inflow of cold seawater into the oceanic crust. Hydration and crustal cracks activated by extensional bending-related faulting are suggested to govern the reduced velocities in the vicinity of the trench. Considering typical flow distances of 50 km, water might be redistributed over most of the trench-outer rise area. Where trapped in faults, seawater may migrate down to mantle depth causing up to  $\sim 9\%$  of serpentinization in at least the uppermost  $\sim 2$  km of the mantle between the outer rise and the trench axis.

## 2.1 Introduction

Oceanic lithosphere created at moderate to fast spreading mid-ocean ridges is characterized by a ridge-parallel fault pattern. Pervasive fracturing and hydrothermal activity, however, are largely confined to crustal levels [e.g., *Carbotte and Scheirer*, 2004; *Karson*, 1998]. As the crust ages, cracks and pore spaces inherently related to the formation of crust are clogged by precipitation of secondary hydrothermal alteration products in the extrusive lava pile [e.g., *Alt et al.*, 1986; *Wilkins et al.*, 1991; *Grevenmeyer and Bartetzko*, 2004]. Global compilations of seismic refraction velocities for the uppermost oceanic crust [*Grevenmeyer and Weigel*, 1996; *Carlson*, 1998] and dedicated seismic refraction experiments [e.g., *Grevenmeyer and Weigel*, 1997; *Grevenmeyer et al.*, 1999] have established an empirical relationship between lithospheric age and seismic velocity. The global trend suggests that uppermost P-wave velocities of layer 2 increase rapidly close to the spreading axis and within  $\sim 8$  Ma reach values of mature oceanic crust ( $> 4.5$  km/s) [*Carlson*, 1998; *Grevenmeyer and Bartetzko*, 2004]. Within this context, we will refer to "normal" mature oceanic lithosphere typical of fast spreading structures if: (i) hydration is confined to the permeable upper lava pile, (ii) the ridge flank hydrothermal circulation system has largely ceased, and (iii) the oceanic lithosphere is positioned away from anomalous regions such as fracture zones and hotspots regions [e.g., *White et al.*, 1992].

Growing observational evidence in subduction zones suggest that this condition of "normal" and "unaltered" ocean lithosphere can be dramatically perturbed at the outer rise seaward of deep sea trenches [e.g., *Peacock*, 2004; *Ranero et al.*, 2003]. The outer rise is formed when the ocean lithosphere approaches a subduction zone and bends into the trench; thus, producing a prominent outer bulge seaward of the trench axis. Here, outer rise earthquakes are linked to bending-related normal faulting [*Chapple and Forsyth*, 1979] and possibly rupture the oceanic mantle [e.g., *Kanamori*, 1971; *Christensen and Ruff*, 1983], creating a pervasive tectonic fabric that may cut across the crust, penetrating deep into the uppermost mantle [e.g., *Peacock*, 2001; *Ranero et al.*, 2003]. Moreover, new crustal

cracks and fissures are caused by bending-related faulting seaward of the trench axis, modifying the structure of the crust. Therefore, bending-related faulting plays a crucial role for the alteration of oceanic lithosphere; it affects the porosity and permeability structure of the entire oceanic crust and consequently generates pathways for fluids down to mantle depth.

One key factor controlling the local hydrogeological regime of the oceanic lithosphere is the thickness of the sedimentary blanket. Convergent margins such as central America, north and central Chile are poorly sedimented, and seawater can easily enter the igneous oceanic crust where the permeable basement rocks are widely exposed (e.g., surface-cutting tectonic faults or outcropping basement highs). These subduction zones have been suggested to be characterized by a high degree of hydration at the outer rise [Ranero *et al.*, 2003; Ranero and Sallares, 2004; Grevemeyer *et al.*, 2005; 2007]. In contrast, in well sedimented margins (Cascadia, Makran and southern central Chile), a thick sedimentary cover is believed to hinder interaction between the ocean and basement. Therefore, the degree of hydration is expected to be lower than in poorly sedimented trenches, although mechanisms by which fluids may bypass thick sediments remain still under debate. In general, the hydrothermal activity in the oceanic crust is controlled by faulting and the presence of outcropping basement highs. Heat flow data suggest that hydrothermal circulation is more vigorous at trenches where bending-related normal faults breach the seafloor and thus facilitate fluid flow into the crust [Grevemeyer *et al.*, 2005]. Outcropping basement also play a crucial role, since it may act as transmissive pathway for fluids and heat in areas where the surrounding basement is blanketed by sediments, as it has been evidenced by anomalous low heat flow values near seamounts, indicating an efficient inflow of cold seawater into the oceanic crust [Villinger *et al.*, 2002; Fisher *et al.*, 2003a, 2003b]. Isolated basement outcrops penetrating through thick sediments might guide hydrothermal circulation between sites separated by large distances [Fisher *et al.*, 2003a]. Once cold seawater is infiltrated and bounded in the upper oceanic crust, tectonic faulting may allow fluids trapped within crustal pores spaces to enter the lower crust and perhaps even the upper mantle [e.g., Grevemeyer *et al.*, 2005].

To better understand the transition from "normal" and "dry" to deformed and hydrated subducting lithosphere and its degree of hydration in the trench-outer rise area, we studied the velocity structure of the incoming oceanic Nazca plate offshore of south-central Chile. Seismic wide-angle reflection and refraction data are used to derive an accurate 2D tomography velocity model of a  $\sim 250$  km long seismic profile located oceanward from the Chile trench axis. We present new geophysical evidence documenting changes in the seismic structure of the incoming oceanic plate from the outer rise to just before its sub-

duction in the deep sea trench. A nonlinear Monte Carlo uncertainty analysis is performed to estimate a posteriori model variance of the tomography velocity model. In addition, heat flow data recorded at the outer rise are used to study the distribution of temperature along the sediment/crust boundary. The data were acquired during the R/V Sonne cruise SO181 as part of the TIPTEQ (from The Incoming Plate to Mega-thrust Earthquake processes) project [Flueh and Grevemeyer, 2005].

## 2.2 Tectonic setting

Along the south-central Chile trench the southern Nazca plate subducts at a relatively high convergence rate of  $\sim 6.6$  cm/yr beneath the South American plate, with a convergence azimuth of  $\sim 78^\circ\text{E}$  [Angermann *et al.*, 1999] (Figure 2.1). The southern Nazca plate has been formed at the Chile Rise (a fast mid-ocean spreading ridge). Fracture zones (FZs) cut the Chile Rise into several segments (Figure 2.1), resulting in abrupt changes of thermal states along the plate boundary. The spreading center segments bounded by these fracture zones are roughly parallel to the trench strike (Figure 2.1). At  $\sim 46.4^\circ\text{S}$  the Chile Rise is currently subducting, defining the Chile Triple Junction (CTJ) of the subducting Nazca and Antarctic plates, and the continental South American plate. North of the CTJ occur a series of age jumps across several fracture zones, from 0 Ma up to 18.5 Ma at the Valdivia FZ (Figure 2.1). The south-central Chile trench is filled by terrigenous sediments sourced from the Andes [Thornburg and Kulm, 1987]. Sediment within the trench are redistributed from south to the north [Thornburg *et al.*, 1990], which is explained by the slight northward dip of the trench floor [e.g., Thornburg *et al.*, 1990]. Trench fans ( $33\text{--}41^\circ\text{S}$ ) are built at the mouths of major submarine canyons and channels which act as point sources of sediment supply [Thornburg and Kulm, 1987]. South of  $41^\circ\text{S}$ , sheet turbidites extend across the entire width of the trench [Thornburg and Kulm, 1987].



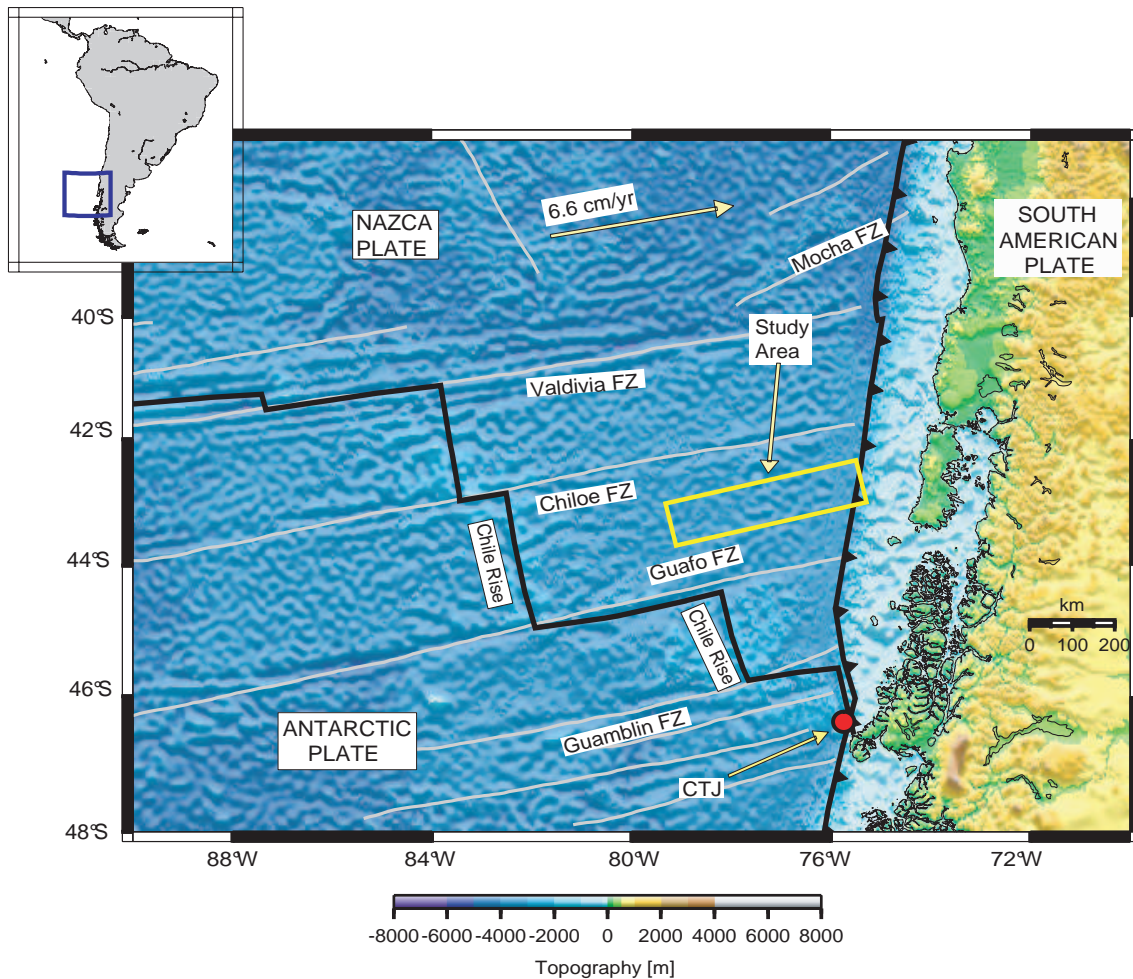


Figure 2.1: Geodynamic setting of Nazca, Antarctic, and South American plates. These plates join at the Chile Triple Junction (CTJ), where the Chile Rise is currently subducting at  $\sim 46.4^\circ\text{S}$ . The oceanic Nazca plate is segmented by several fracture zones (FZs), resulting in a strong variability of the age of the subducting plate. The study area is located between two Fracture Zones: Chiloe FZ and Guafo FZ, and its plate age ranges from 18.5 to 10 Ma along the Chile trench.

The westward terminus of the seismic wide-angle profile studied here is located approximately 280 km eastward of the Chile Rise on 9 Ma old crust [Tebbens *et al.*, 1997], the line orientation being parallel to the plate motion vector (Figure 2.1). The profile is located between Chiloe and Guafo FZs (Figure 2.1), where the plate age decrease from 18.5 to 10 Ma. along the Chile trench, and the half-spreading rate ranges between 45 and 35 mm/yr [Tebbens *et al.*, 1997]. The trench basin is broad, owing to the large extension of turbidite deposits seaward [Voelker *et al.*, 2006]. Further to the west, the Nazca plate is covered by a few hundred meters of hemipelagic and pelagic sediments, whereas towards the trench, the sedimentary cover becomes thicker due to the turbiditic deposits filling the trench with a total thickness of  $\sim 2$  km [Scherwath *et al.*, 2006]. The continental slope

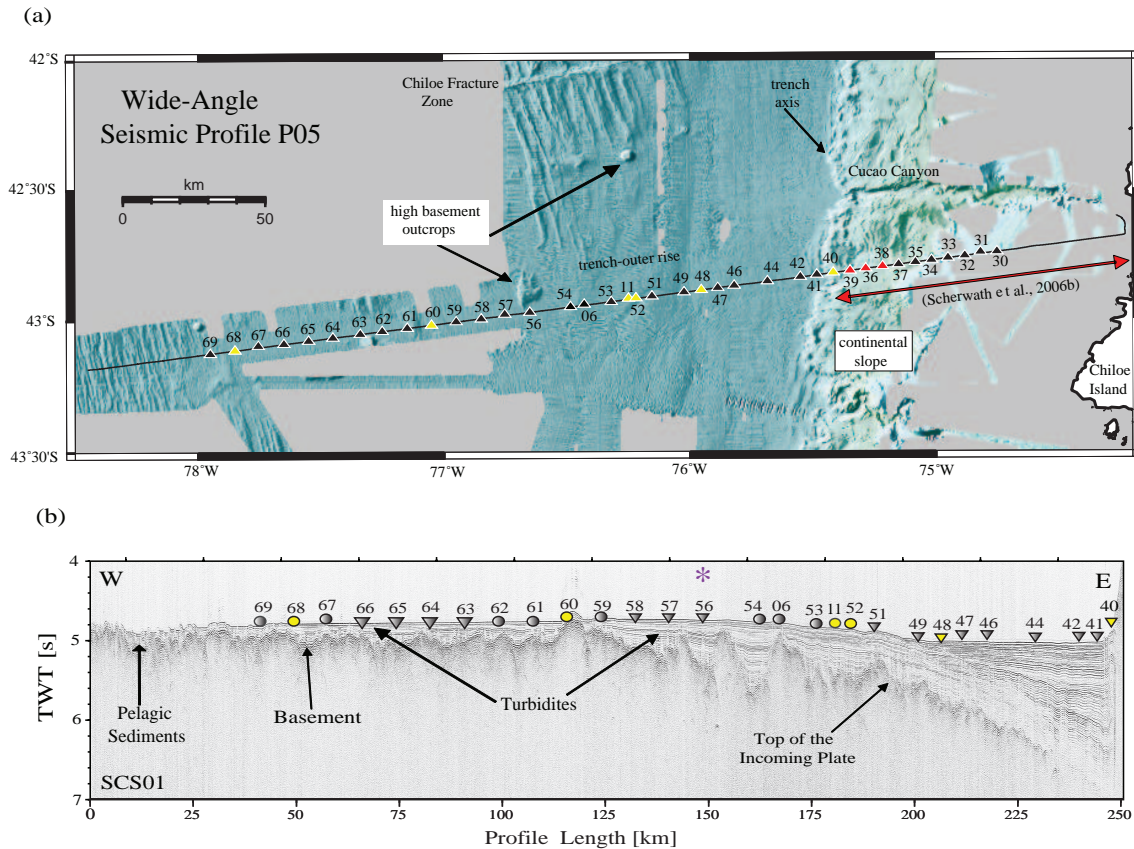


Figure 2.2: (a) High-resolution bathymetric image and wide-angle seismic profile P05. The seismic line begins  $\sim 280$  km from the Chile Rise (see Figure 2.1) and it extends up to the deep sea trench and part of the continental slope. Yellow triangles indicate the six stations of which data examples are shown in Figures 2.3-2.5 and 2.10. Red dots indicate the three stations positioned on the continental slope [Scherwath et al., 2006b], which are included in our tomographic model. (b) High resolution seismic line SCS01 coincident with wide seismic profile P05. Locations of OBH are shown by solid circles and OBS by solid triangles. Location of the high basement outcrop is denoted by asterisk. Some tensional normal faults are reflected by offsets in the trench-outer rise region.

is steep and is characterized by the presence of the submarine Cucao Canyon (Figure 2.2a), while the continental shelf is broad and probably trapped large volume of Pliocene sediments [Reichert et al., 2002].

## 2.3 Seismic data

From December 2004 to February 2005, the TIPTEQ project investigated the subduction zone offshore south-central Chile between  $35^\circ$  and  $48^\circ\text{S}$  aboard of the German R/V Sonne. During the cruise seismic wide-angle reflection and refraction data, high-resolution seismic reflection data, seismological data, heat flow, and multibeam bathymetry were acquired in this region [Flueh and Grevemeyer, 2005; Scherwath et al., 2006a] to study the

physical properties of the incoming Nazca plate and its impact on seismogenesis, offshore of the rupture area of the 1960 Chile megathrust earthquake. In this paper, we present seismic wide-angle data that were collected along the profile P05 located seaward of the trench axis on the oceanic Nazca plate, supplemented by high-resolution swath bathymetric images of the surrounding seafloor (Figure 2.2a). Shots were recorded with 38 OBS (Ocean Bottom Seismometers) [Bialas and Flueh, 1999] and OBH (Ocean Bottom Hydrophones) [Flueh and Bialas, 1996] spaced at a distance of  $\sim 5.5$  km. Coincident seismic reflection data were also collected along this profile (Figure 2.2b). For the reflection investigation a 100-m-long 16-channel streamer and a Generator/Injector (GI) gun with a volume of 1.5 liters were used, providing high resolution images of the sedimentary sequences blanketing the incoming plate. From the 38 seismic ocean bottom stations, 28 were deployed on the oceanic plate and the rest along the continental slope. In order to study the seismic structure of the oceanic Nazca plate, we used the OBH/S deployed seaward of the trench. Three stations on the continental slope were also included in the inversion approach to constrain the velocity structure and Moho depth below the trench (see Figure 2.2.a).

The seismic source for the refraction work was a cluster of 8x8-liters G-guns, providing a total volume of 64 liters for each shot. This source was fired at a time interval of 60 s, which corresponds to an average shot spacing of  $\sim 150$  m. The record sections were interpreted after bandpass filtering and predictive deconvolution. The signal-to-noise ratio obtained for most of the stations is high (Figures 2.3-2.5). Crustal refractions ( $P_g$ ), Moho reflections ( $P_mP$ ) and upper mantle refractions ( $P_n$ ) were recorded on almost all stations with excellent quality. Five examples of seismic record sections are shown in Figures 2.3-2.5, with their respective seismic phases identified. Apparent velocities, which are influenced by the trench-sediment, decrease towards the trench. Refractions through trench-sediment  $P_s$ , and reflections from the top of the igneous crust ( $P_bP$ ) start to appear at approximately profile-km 200 and hence 50 km from the trench axis. Figure 2.5e shows  $P_s$  and  $P_bP$  of good quality at OBH 40 at the trench. Those travel times complement the high-resolution seismic reflection data (Figure 2.2b) and are used to constrain the sedimentary section in this part of the model.

Picking of the seismic phases was done manually, and picking errors were assigned on the basis of the dominant period of the phase. A total of 5048 first arrivals ( $P_g$  and  $P_n$ ), and 1721 Moho reflections ( $P_mP$ ) were picked from 31 record sections. For the sedimentary section only stations located to the east of  $x=200$  km were utilized, because clear  $P_s$  and  $P_bP$  phases are confined to the trench basin. A total of 1456  $P_s$  and 654  $P_bP$  were picked from these stations. Typically, errors were assumed to be half a period of one arrival,

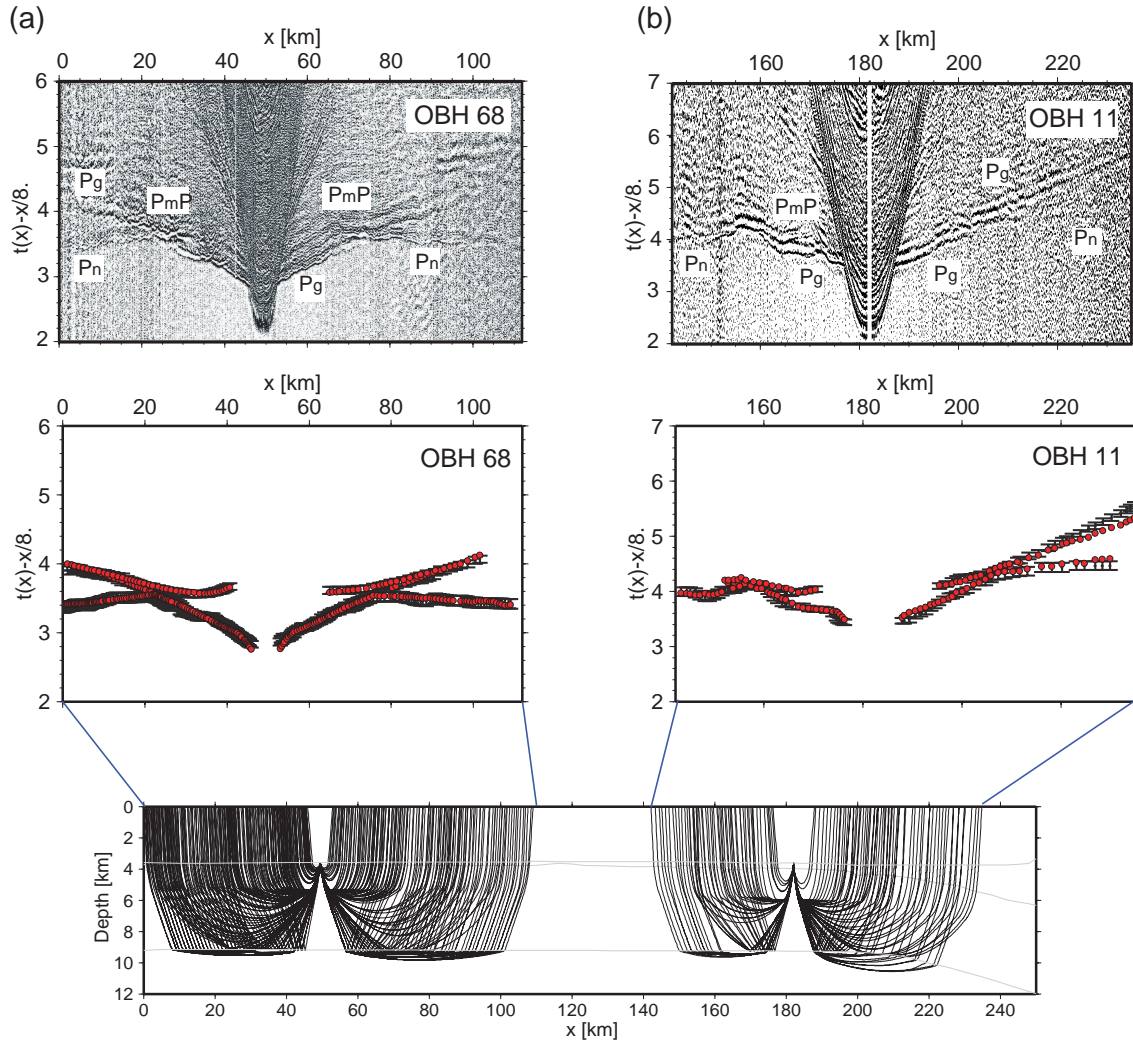


Figure 2.3: Examples of wide-angle seismic data with picked (solid circle with pick error) and predicted (red circles) travel times. Calculated travel times are based on the velocity model presented in Figure 2.9a, and corresponding ray paths are also plotted at the bottom. (a) OBH 68 and (b) OBH 11.

to account for a possible systematic shift in the arrival identification, and were weighted according to the phase quality. Average picking uncertainties are  $\sim 50$  ms at near offsets and  $\sim 70$  ms at far offsets for refracted arrivals, and  $\sim 50$  ms and  $\sim 70$  ms for  $P_bP$  and  $P_mP$  phases, respectively.

## 2.4 Travel time tomography scheme

The velocity-depth model was derived using the joint refraction and reflection travel time inversion method of *Korenaga et al.*, [2000]. This method allows simultaneous refraction and reflection travel times inversion for a 2-D velocity field that is parameterized as a sheared mesh hanging beneath the seafloor and where node spacings can vary laterally

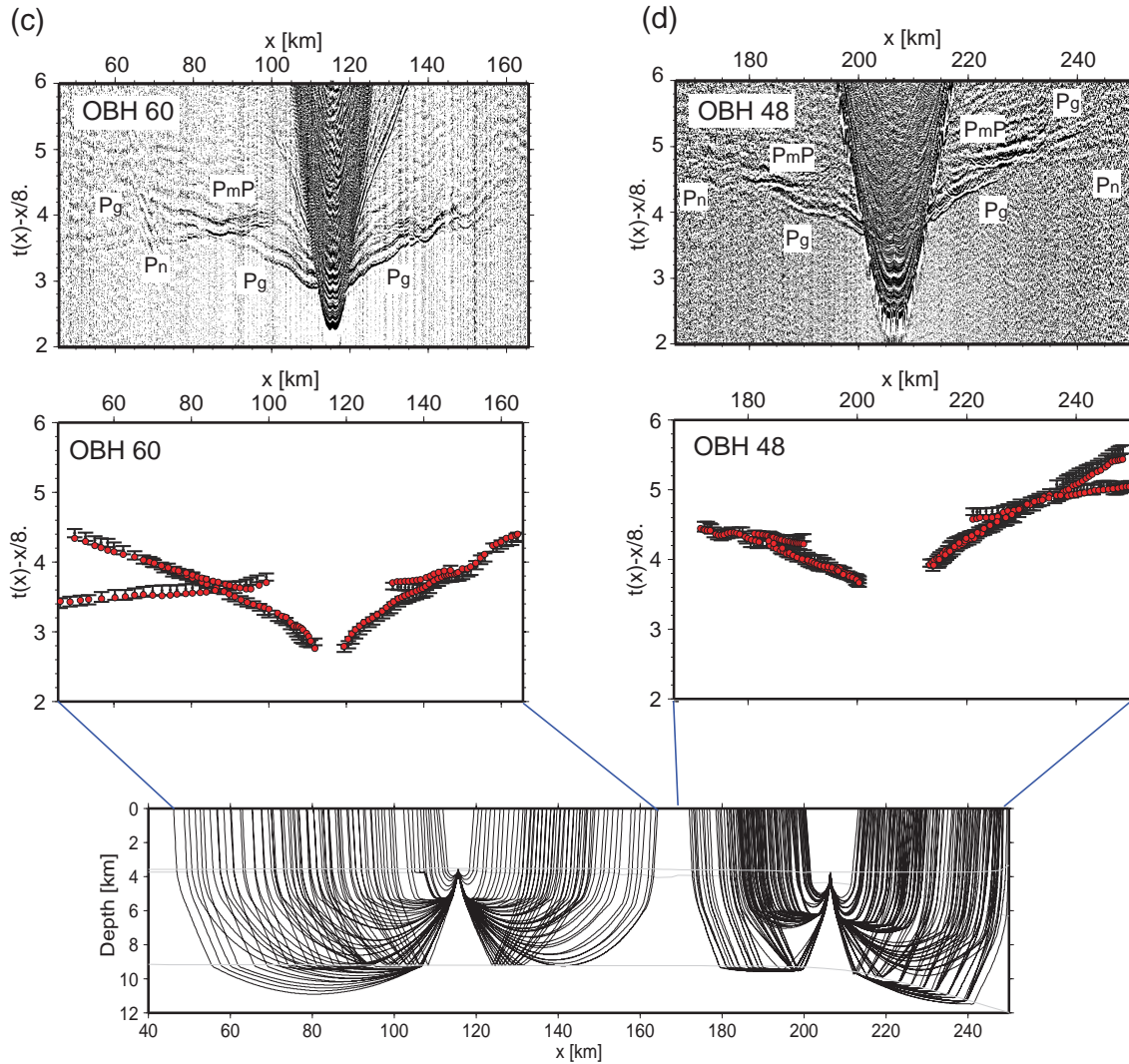


Figure 2.4: (continued) (c) OBH 60 and (d) OBH 48.

and vertically. The floating reflector is represented as an array of linear segments whose nodal spacing is independent of that used in the velocity grid and it has just one degree of freedom (vertical direction). Travel times and ray paths are calculated by utilizing a hybrid raytracing scheme based on the graph method and local ray-bending refinement [van Avendonk *et al.*, 1998]. Smoothing constraints using predefined correlation lengths (average-smoothness window) and optimized damping constraints for the model parameters are employed to regularize an iterative linearized inversion [Korenaga *et al.*, 2000]. We use a hybrid approach of multi-step tomography using four layers, (1) water, (2) sedimentary section, (3) oceanic crust and (4) upper mantle. To derive the velocity depth model, the water depths were taken from the multibeam bathymetry, which remained fixed during the inversion. The vertical incidence reflection data, sediment refracted  $P_s$  and reflected  $P_bP$  phases were used to invert for the velocities and thickness of the sedimentary trench

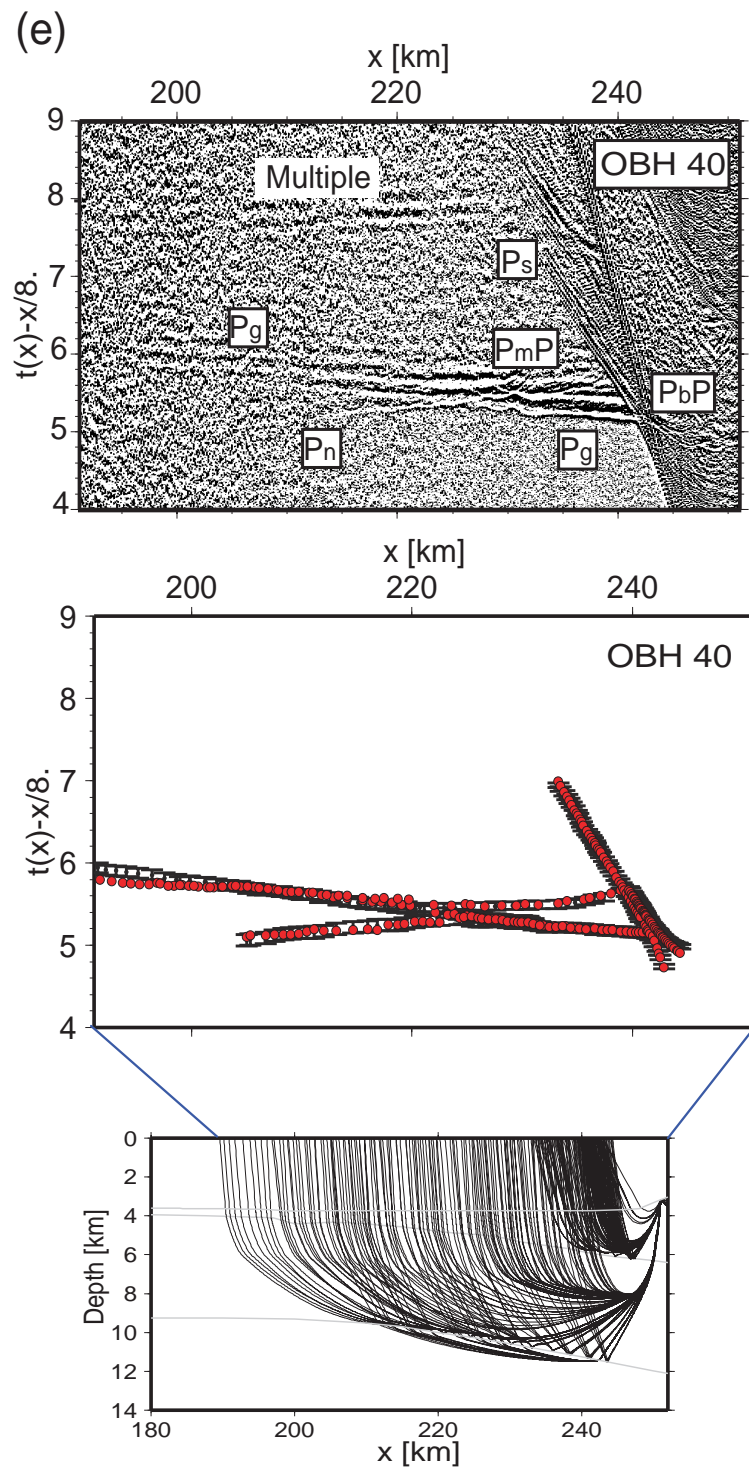


Figure 2.5: (continued) (e) OBH 40

fill and hence the geometry of the top of the downgoing plate. Sedimentary velocities and basement depth were then held fixed in the following iterative inversions. The oceanic crust was inverted using  $P_g$  and  $P_mP$  phases in order to derive the velocity field and

Moho depth, and similarly, the crustal velocities and Moho depth remained fixed for the next inversion. Finally, the upper mantle velocities were inverted using  $P_n$  phases. The applied hybrid scheme uses both first and second arrivals to constrain the velocity model, without the need to disregard for example secondary arrivals such as lower crustal  $P_g$ , phases which become secondary arrivals where  $P_n$  arrivals overtake  $P_g$ .

Horizontal grid spacing of the model used for the velocity inversion is 0.5 km, whereas the vertical grid spacing is varied from 0.05 km at the top of the model to 0.5 km at the bottom. Depth nodes defining the reflectors are spaced at 2 km. We used horizontal correlation lengths ranging from 2 km at the top to 10 km at the bottom of the model, and vertical correlation lengths varying from 0.4 km at the top to 2.5 km at the bottom. Depth and velocity nodes are equally weighted in the joint refraction and reflection travel time inversion.

### 2.4.1 Sedimentary section tomography

Seaward from the trench, the basement was derived by picking and converting the vertical incidence reflections from two-way-time (TWT) data to depth using a constant velocity of 1.7 km/s. Approaching the trench (up to profile distance km 200), a 2-km deep trench basin has been developed with incoming pelagic sediments and turbidites (Figure 2.2b). Here, refracted  $P_s$  phases and reflected  $P_bP$  phases (Figure 2.5) were used to invert the velocity structure of the sediments in the trench and the top of the oceanic crust. The starting model for the sedimentary trench fill and lower continental slope is shown in Figure 2.6a and was set up using the semi forward modeling approach of *Zelt and Smith, [1992]*. The starting model includes the known bathymetry; the velocity at the top of the sedimentary layer is set to 1.7 km/s. Below the seafloor the velocity varies depending on the depth using a constant vertical velocity gradient of  $1 \text{ s}^{-1}$ . The starting reflector is directly computed by converting the TWT data of the corresponding basement reflector to depth. For this reference model, the initial root-mean-square (RMS) travel time misfits for  $P_s$  and  $P_bP$  are 407 ms and 567 ms, respectively. As the crustal phases were omitted in this step, the input model still contains sedimentary velocity below the sediment-crust boundary (Figure 2.6a).

Tests with several starting models converge to nearly the same final model. In order to study the accuracy of the final model, we employed the Monte Carlo method [e.g., *Korenaga et al., 2000*]. The uncertainty of a nonlinear inversion can be expressed in terms of the posterior model covariance matrix [e.g., *Tarantola, 1987*], which can be approximated by the standard deviation of a large number of Monte Carlo realizations assuming that all the realizations have the same probability [e.g., *Tarantola, 1987*]. The uncertainty estimated by this method should be interpreted as the uncertainty for our model parameters (i.e.,

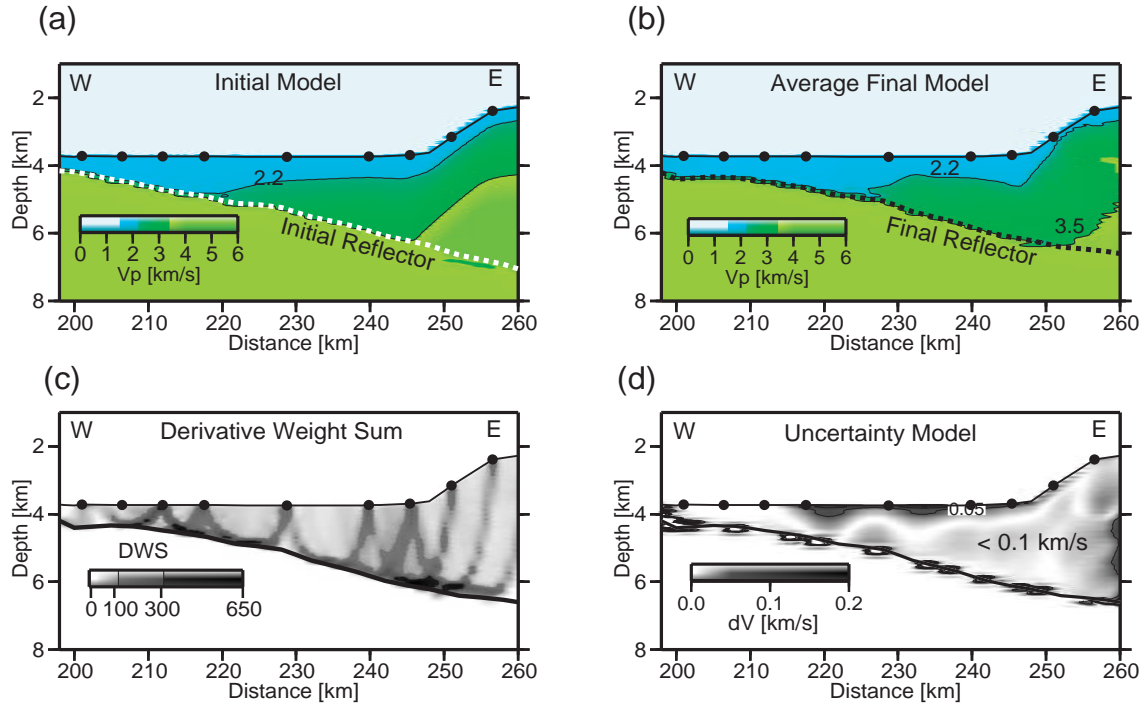


Figure 2.6: Result of sedimentary tomographic inversion using  $P_s$  and  $P_bP$  phases, and reflection data. (a) Initial velocity model used as a reference for the Monte Carlo analysis and for velocity inversion. (b) Final average model of the Monte Carlo ensembles. (c) Derivative Weight Sum DWS for rays traveling throughout model shown in (b). (d) Velocity depth uncertainty model after Monte Carlo type realizations

starting velocity model and smoothing constraints). The procedure to estimate velocity uncertainties consisted of randomly perturbing velocities of our reference model (Figure 2.6a). We generated 100 random initial velocity models by adding smooth perturbations randomly distributed (maximum velocity perturbations of  $\pm 0.1$  km/s at the top and  $\pm 0.4$  km/s at the bottom of the model, with wavelength perturbations of 5 km horizontally and 0.5 km vertically). The basement reflector depth was found by converting the TWT data of the reflector into depth using the velocity distribution of every initial model. In addition to the perturbed reference models we produced 100 so-called noisy arrival time sets constructed by adding random phase errors ( $\pm 50$  ms) and common receiver errors ( $\pm 50$  ms) to the original data set [Korenaga *et al.*, 2000]. Then we performed a tomographic inversion for each velocity model with one noisy data set, in order to estimate not only the dependence of the solution on the reference model but also the effect of phase arrival time picking errors. The mean deviation of all realizations of such an ensemble is considered to be a statistical measure of the model parameter uncertainties [e.g., Tarantola, 1987]. All of the Monte Carlo inversions converged in less than 10 iterations to  $\chi^2 = 1$ , where  $\chi^2$  is the normalized sum of the RMS misfits divided by the corresponding picking uncertainties; a value of 1 means that the model error is equal to the data uncertainty. Figure 2.6b shows



the average model from the 100 final models. The RMS error was reduced to  $\sim 50$  ms for refractions and  $\sim 55$  ms for reflections. Figure 2.6c shows the derivative weight sum (DWS), which is a statistical parameter indicating the model resolution and ray density. The standard deviation of the calculated velocities for most of the model is below 0.1 km/s and for the reflector depth  $< 0.1$  km, except at the right edge of the model (Figure 2.6d) where the velocity uncertainty increases to values larger than 0.2 km/s and for the depth uncertainty to values of  $\sim 0.3$  km due to the reduced data coverage.

### 2.4.2 Oceanic crust tomography

For the determination of the crustal part of the velocity model we held the previously determined sedimentary section fixed by using spatial damping [Korenaga *et al.*, 2000]. We inverted the oceanic crust by including all crustal phases (first and later arrivals) to their maximum offset, and the depth of the floating reflector (Moho) was identified using the mantle phases  $P_mP$  simultaneously in the tomographic inversion [Korenaga *et al.*, 2000]. As with the inversion of sedimentary layer, we use the Monte Carlo scheme for determining the crust velocities and thicknesses, and therefore a suite of starting models was required.

#### Reference model

The 2-D starting velocity models were obtained by hanging 1-D crustal velocity profiles beneath the basement (see Figure 2.7c). The reference 1-D velocity depth model was composed of oceanic upper crust (layer 2) and the lower crust (layer 3). Minimum values for top, mid, and bottom velocities were 3.0, 6.0, and 6.5 km/s, while corresponding maximum values were 5.0, 7.0, and 7.5 km/s, respectively. The upper crustal thickness could vary from 1 to 3 km, and the lower crustal thickness could vary from 3 to 5 km. The initial geometry of the Moho boundary was chosen as the sum of the obtained smoothed basement geometry in the previous sedimentary modeling and a given crustal thickness, which allowed variations between 4 and 8 km. Different tests showed that variation of the starting model within this model space did not affect significantly the solution. Figure 2.7a shows the final velocity model derived by averaging all Monte Carlo ensembles.

#### Model uncertainty, Monte Carlo-type analysis

Velocity and Moho-depth uncertainties of the model parameters in the oceanic plate were estimated by performing a Monte Carlo-type analysis [e.g., Tarantola, 1987], as we described above. Figure 2.7c shows the area covered for the 100 initial two-layer crustal velocity profiles and the 100 starting Moho reflectors underneath the basement. Initial RMS travel time misfits were generally higher than 900 ms, and  $\chi^2$  was initially greater

than 100. The stopping criterion for each inversion was  $\chi^2 \sim 1.0$ , which was reached typically after 5 iterations. Using the 100 realizations, the final average crustal velocity model and its standard deviation were computed (Figure 2.7d). The standard deviation of the velocities is lower than 0.1 km/s in the upper crust and the main part of the lower crust as well, increasing to values of 0.1-0.15 km/s in the deepest region of the lower crust. Velocity and Moho depth uncertainties are larger at the western edge of the model where the ray coverage is poor. Moho depth uncertainties in the middle of the model are as low as 0.15 km and reach 0.4 km at the edges of the velocity model. At the trench, velocities and Moho depth are well constrained with the inclusion of stations on the continental slope [Schervath *et al.*, 2006b]. The DWS for the model is shown in Figure 2.7b, which shows excellent ray coverage.

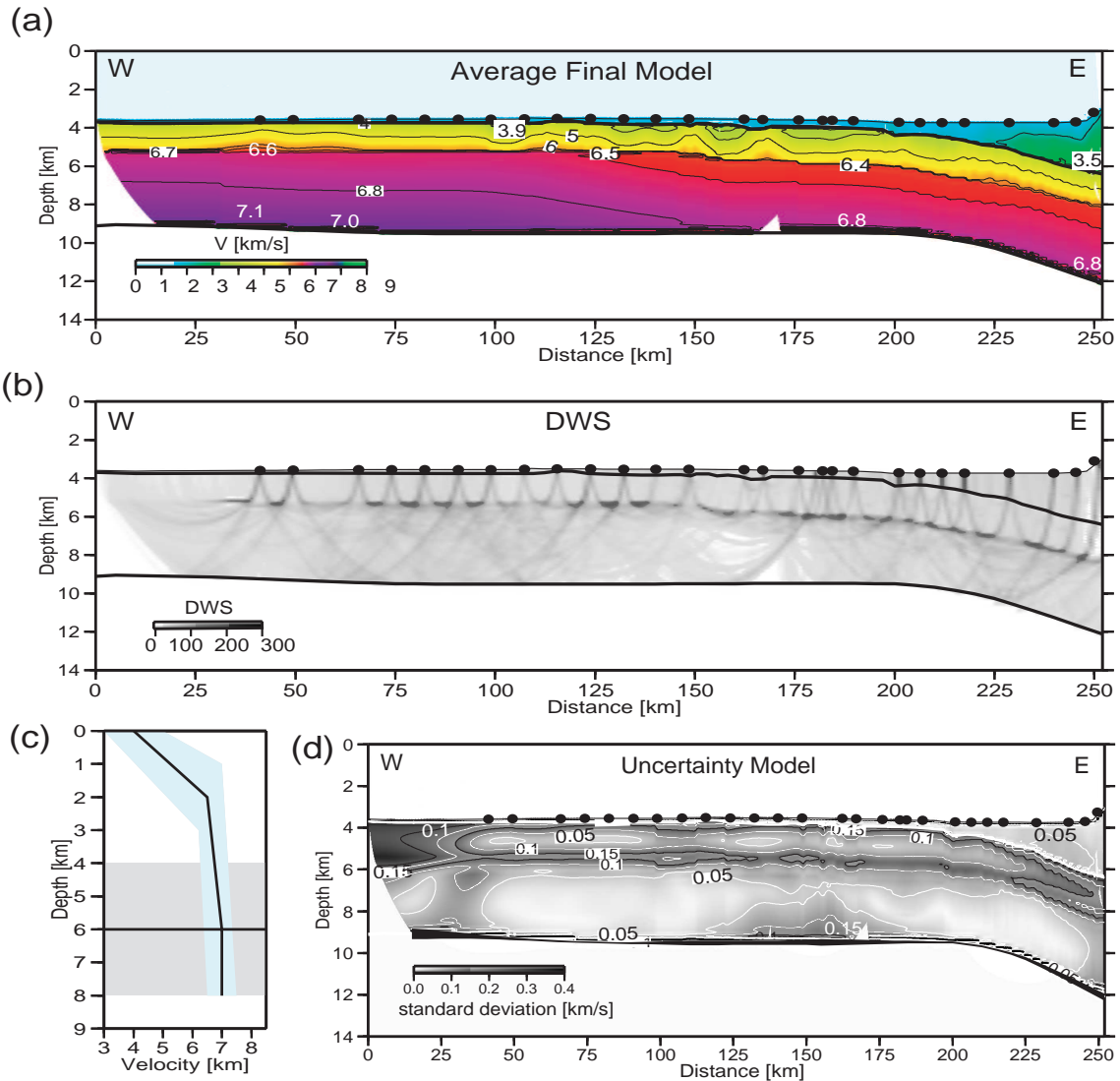


Figure 2.7: Result of crustal tomographic inversion using  $P_g$  and  $P_mP$  phases. (a) Final velocity model derived by averaging all Monte Carlo ensembles. (b) Derivative weight sum. (c) Range of parameters for Monte Carlo ensembles. A starting model consists of a 1-D crustal velocity profile, the Moho depth is the sum of the previously obtained smoothed basement and a given crustal thickness. Gray and light blue regions show possible variations in Moho depth and velocity randomization, respectively. (d) Corresponding standard deviation for velocity and depth nodes, contour interval is at 0.05 km/s.

### Resolution test

To check the resolvability of the obtained velocity model, in particular the anomalous low velocity zones in the trench-outer rise region (Figure 2.7a), we have created a synthetic model consisting of four sinusoidal anomalies located in the oceanic crust (see Figure 2.8a), which are superimposed onto the final average velocity model. The maximum amplitude of each Gaussian anomaly is  $\pm 6\%$  (Figure 2.8). Synthetic travel time data

with the same source-receiver geometry as in the real data set have been generated with the perturbed model, and they were inverted using an initial unperturbed model to see how well given perturbations are recovered. The recovery model is plotted in Figure 2.8b, which was gained after 3 iterations. The result shows that position, shape and amplitude of the velocity anomalies are reasonably well recovered within the uncertainty limits. Despite a certain deterioration in the shape of the anomalies, the result indicates that the geometry and instrument spacing yields a sufficiently high resolution for these structural anomalies, discerning between positive and negative variations along the oceanic crust. The tomographic inversion scheme used here is able to resolve structures with size and amplitude similar to the normal and low-velocity zone at this depth range. This shows that the crustal velocity reduction of the oceanic crust when approaching the trench shown in Figure 2.7a is not an artifact of the seismic tomographic inversion procedure but a real feature.

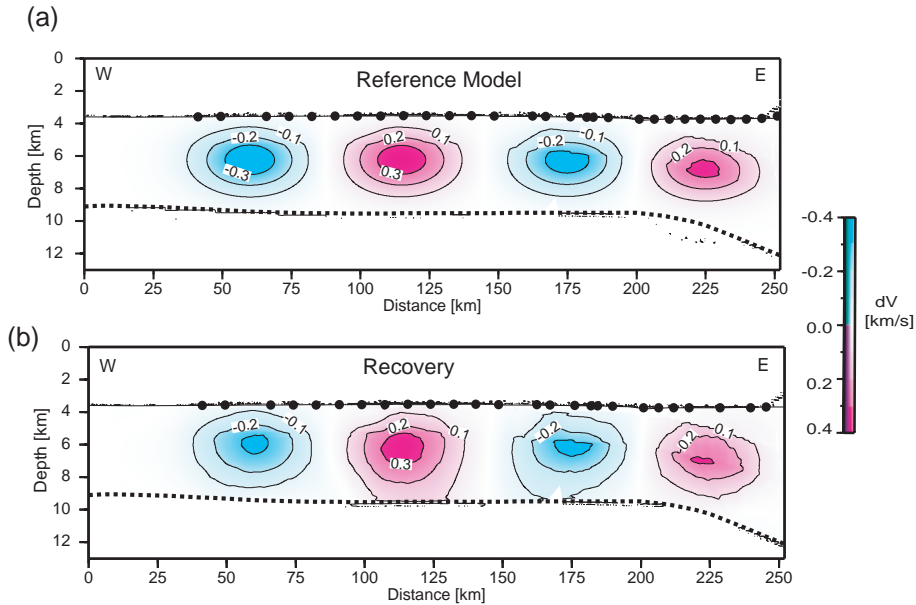


Figure 2.8: *Results of resolution test. (a) Synthetic reference velocity model, consisting of four single sinusoidal anomalies superimposed onto the final velocity model of Figure 2.7a. (b) Recovery obtained after three iterations.*

### 2.4.3 Upper mantle tomography

For the subsequent tomographic inversion of the mantle refraction  $P_n$ , a "layer-stripping" procedure was chosen, preserving the structural and velocity information above the Moho interface gained before. For the Monte Carlo inversion approach, we constructed several initial models by varying the uppermost mantle velocity between 7.5 to 8.5 km/s and the mantle velocity gradient between 0 and  $0.04 \text{ s}^{-1}$  respectively. The final average model and

its uncertainties are plotted in Figure 2.9. The results exhibit a clear trend of velocity-reduction towards the trench, which is well correlated with the location of the outer rise but landward of the crustal velocity reduction. Uncertainties of the upper mantle velocity in the outer rise region range between 0.1-0.2 km/s and are well constrained in the seaward part ( $\sim 0.1$  km/s) where the plate geometry is relatively flat and the sediments are thin.

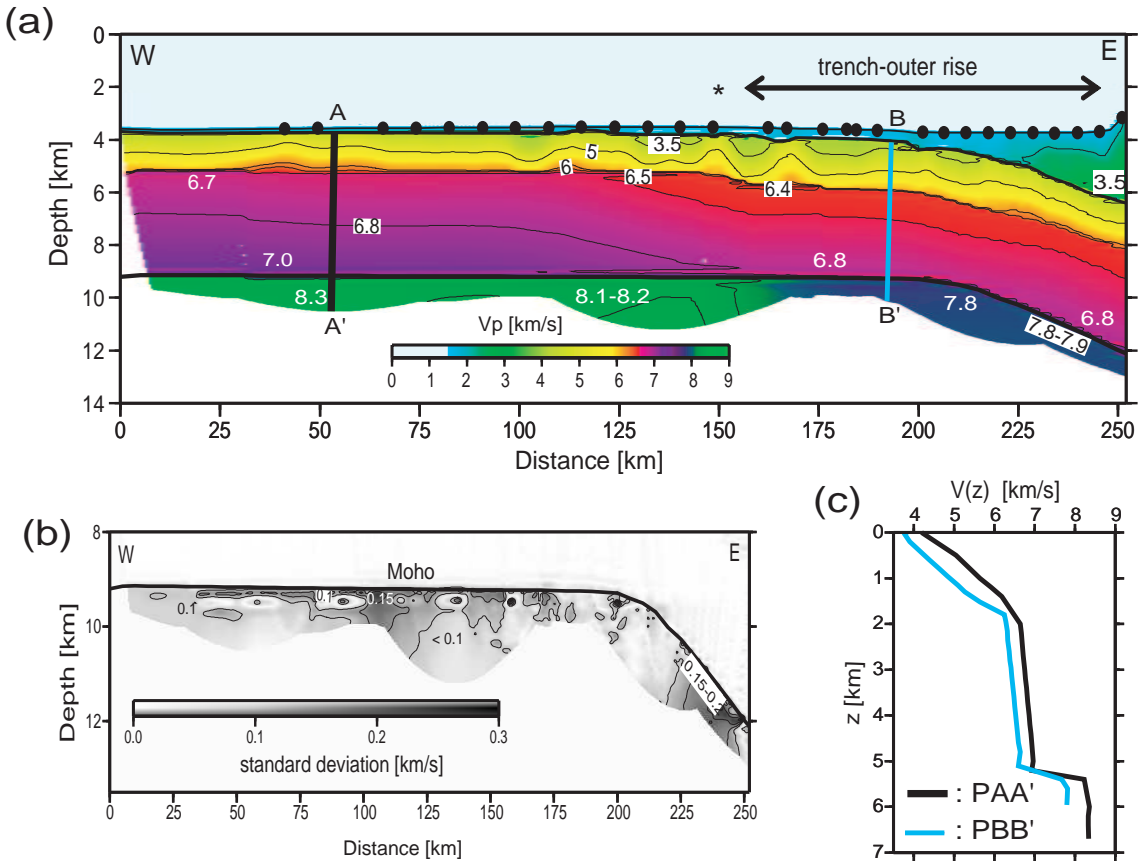


Figure 2.9: Result of mantle tomographic inversion using refracted  $P_n$  phases. (a) Final velocity model derived by averaging all Monte Carlo ensembles (see text for details). (b) Corresponding standard deviation for upper mantle velocity model, contours are drawn at 0.05 km/s interval. Velocity uncertainty is higher between  $x=220-250$  km below the thick sediments at the trench. (c) Comparison of velocity depth structure for extracted profile from our velocity model shown in Figure 2.9a. Black line shows velocity structure  $V(z)$  away from the trench and blue line  $V(z)$  beneath the trench-outer rise.

To survey the robustness of our tomographic results, we conducted independent forward modeling seeking a minimum-structure model that satisfies the data. Model features common to the tomographic and forward-modeling output may be assessed without using subjective a priori information [e.g., Zelt and Smith, 1992]. We studied uppermost mantle velocity and different velocity gradients by keeping the structural and velocity informa-

tion above the Moho interface gained for the crustal tomography (Figure 2.7a). Figure 2.10a shows the record section of OBH 68, which displays an example of the onset of the  $P_g$ ,  $P_mP$  and  $P_n$  phases. "Normal" crustal velocities fit the crustal phases well, and the best-fitting uppermost mantle velocity is about 8.3 km/s. A comparison with a reduced upper mantle velocity of 8.0 km/s produces a large  $P_n$  travel time misfit (Figure 2.10a), and so we conclude that the seismic data can only be explained with uppermost velocities as fast as 8.3 km/s. Towards the trench the situation changes; a "delay" of  $P_n$  arrivals is observed (Figure 2.10b). These delayed  $P_n$  arrivals are already apparent in most of the trench-ward branches of seismic stations. A large amount of the total delay in  $P_n$  arrivals can be attributed to the thick sedimentary sequence, which covers the deflected downgoing plate (see Figure 2.6b). However, as our previous sedimentary tomography constrains the sediment structure, a remaining delay of 150 ms is still required to fit  $P_n$  arrivals within the uncertainty of the picked arrivals. A better  $P_n$  travel time fit occurs with uppermost mantle velocities ranging between 7.7-8.0 km/s. We also plotted the predicted travel times for  $P_n$  with an uppermost mantle velocity of 8.2 km/s; the arrivals are predicted up to 150 ms earlier than observed (Figure 2.10b). In conclusion, the high quality  $P_n$  phases clearly define a reduction of upper mantle velocities towards the trench.

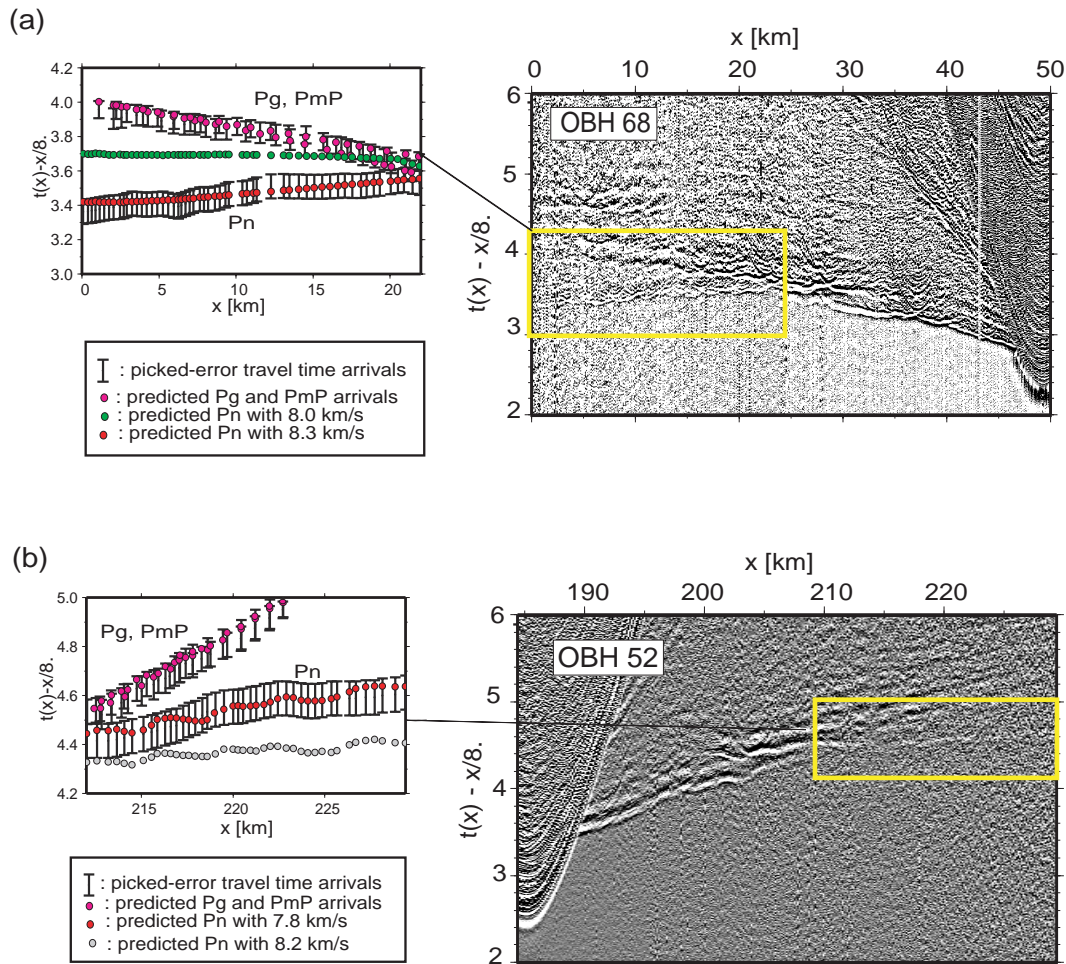


Figure 2.10: Detailed forward analysis of  $P_n$  travel times for oceanward branch of OBH 68 (a) and trenchward branch of seismic record section of OBH 52 (b). Predicted  $P_g$  and  $P_mP$  arrivals are based on the final crustal model shown in Figure 2.7a. (a)  $P_n$  oceanic phases can only be predicted with values as fast as 8.3 km/s (red dots), uppermost velocities values of 8.0 km/s produce a misfit  $> 250$  ms (green dots). (b)  $P_n$  arrivals are predicted up to 150 ms earlier than observed using an uppermost velocity of 8.2 km/s (gray dots); a better  $P_n$  travel time fit occurs with uppermost mantle velocity of 7.8 km/s (red dots).

## 2.5 Discussion

The data presented in this paper show systematic changes of crustal and upper mantle seismic structure in the form of velocity reduction in the oceanic Nazca plate while it approaches the Chile trench. In this section, we discuss the transition from "normal" to deformed and altered oceanic subducting lithosphere and its possible causes within the geodynamic framework.

### 2.5.1 Seismic structure of the oceanic lithosphere

#### Sediments and basement topography

Seaward from the trench ( $> 200$  km) the southern Nazca plate is covered by a thin sequence of pelagic and hemipelagic sediments ( $< 150$  m). Here, high resolution multibeam bathymetric mapping shows the typical topographic pattern of the tectonic fabric formed at the spreading center, which is obscured towards the trench due to turbidite deposits (Figure 2.2b). From profile km  $\sim 50$  to 200, turbidites fill the half-graben structure and overlay pelagic sediments, forming a mix-sedimentary sequence of 200-400 m thickness. Further to the east (in the trench basin), the sedimentary-cover becomes thicker, resulting in a total thickness of  $\sim 2200$  m (Figure 2.6b). Trench sediments were mainly delivered during the Pleistocene glaciation with a rapid sedimentation rate [Bangs and Cande, 1997]. At the bottom of the trench basin, compressional velocities of 3.0-3.5 km/s were detected at 2 km-depth below seafloor. These velocities are because of compaction processes and the increase of sediment size from top to bottom (graded bedding), associated to sedimentary deposit events.

The basement topography is in general rough, and it is characterized by the presence of outcrops of basement highs (Figure 2.2a). In the outer rise ( $x \sim 150$  km), and approximately 5 km to the north of the seismic profile a basement outcrop rises  $\sim 200$  m above the surrounding seafloor (Figure 2.11a), while its associated basaltic edifice rises  $\sim 400$  m above regional basement. Ten kilometers to the north of this basement outcrop, several abyssal hills generated at the spreading center with pervasive faulting and large offsets strike approximately parallel to the trench axis (Figure 2.2a). This area is characterized by pervasive normal faults exposing basement caused by plate bending. Southward and trenchward of the seismic profile, this fault pattern is not visible on the multibeam bathymetry owing to the thicker sedimentary cover. Under the trench fill, however, multi-channel data reveal that as the plate approaches the trench, basement topography becomes rougher and the oceanic crust is probably pervasively fractured due to bending-related faulting (Figure 2.2b).



### Oceanic crust

Two distinct zones of the oceanic crust can be identified in the final model: (i) the oceanward section, away from the trench, and (ii) the trench-outer rise region just prior of the subduction of the oceanic plate. Figure 2.9c compares the velocity structure beneath the sediments for well resolved velocity-depth profiles of zones (i) and (ii).

In the oceanward section of the velocity model, the velocity structure below basement roughly follows the basement topography. Velocities in the  $\sim 1.7$  km thick layer are between 4.0-4.2 km/s at the top and  $\sim 6.6$  km/s at the bottom and correspond to oceanic layer 2; a typical sequence of extrusive basalts on top of a sheeted dike complex and high velocity gradient of about  $1.4 \text{ s}^{-1}$ . Both seismic velocity and gradient are similar to the seismic structure obtained off-axis in the upper crust of the southern East Pacific Rise [Grevemeyer *et al.*, 1998]. These values are in good agreement with mature oceanic crust sufficiently far way from the ridge crests so that strong hydrothermal circulation has largely ceased [Grevemeyer *et al.*, 1999]. Layer 2 overlies a  $\sim 3.6$  km thick layer with velocities increasing from 6.6 km/s to  $\sim 7.0$ - $7.1$  km/s. This seismic structure is typical of oceanic layer 3 normally associated with gabbro and layered gabbro rocks (layer 3A and 3B) [e.g., Vera *et al.*, 1990]. The velocity range of 6.6-7.1 km/s is consistent with lower crust relative anhydrous in composition, which is typical for oceanic crust formed at fast spreading ridges [e.g., Carbotte and Scheirer, 2004; Karson, 1998]. The bulk porosity of the crust should be rather low due to the closure of cracks and fissures by hydrothermal mineralization [e.g., Grevemeyer and Bartzeko, 2004].

Approaching the trench, velocities for the igneous crust start to decrease 100-150 km from the deformation front (Figure 2.7a). The uppermost crustal velocities decrease to values lower than 3.7 km/s (Figure 2.9c), which are much lower than typical uppermost layer 2 velocities of mature oceanic crust ( $> 4.5$  km/s) [Carlson, 1998; Grevemeyer and Bartzeko, 2004]. Lowermost crustal velocities decrease to values lower than 6.9 km/s (Figure 2.7a), implying the likely presence of hydrous minerals, such as chlorite and amphibolites [e.g., Hess, 1962; Christensen and Salisbury, 1975]. The decrease of velocities is accompanied with an increase in roughness of the basement topography, and probably coincides with activation of new cracks and normal extensional faults induced by plate bending [e.g., Ranero and Sallares, 2004]. This process suggests a significant alteration of the porosity structure of the entire subducting oceanic crust.

Moho reflections ( $P_mP$ ) constrain the transition from "crustal" gabbros to "mantle" ultramafic rocks, which occurs at  $\sim 5.3$  km depth below the top of the basement. Crustal thickness is therefore less than the average value of  $6.48 \pm 0.75$  km reported by White *et*

*al.*, [1992] for Pacific crust younger than 30 Ma. *McClain and Atallah*, [1986], however, estimated that Pacific crust averages  $5.67 \pm 0.88$  km for crust of the same age, and *Walter et al.*, [2000] and *Grevenmeyer et al.*, [2007] found in more recent studies that crust of the Cocos plate is 5.0-5.5 km thick.

### Uppermost oceanic mantle

Seaward from the trench, compressional velocity of 8.3 km/s was detected in the uppermost 2-2.5 km of the mantle (Figure 2.9a). Typical mature oceanic mantle velocities are  $> 8.1$  km/s [*White et al.*, 1992], which is usually associated to an anhydrous composition of mantle peridotite [e.g., *Peacock*, 1990]. Thus, oceanic Nazca plate approaches the subduction zone with a mantle comparatively undeformed and dry (Figure 2.9a). Closer to the trench, however, a progressive velocity-reduction in the upper mantle occurs. The velocity reduction is visible  $\sim 80$  km from the deformation front (Figure 2.9a), and they decrease to minimum values of  $\sim 7.8$  km/s, which is significantly lower than the velocity of mantle peridotite ( $>8.1$  km/s).  $P_n$  phases image only the first  $\sim 2$  km of the uppermost mantle in the outer rise area (Figure 2.9a). Thus, the maximum depth of possible hydration in the mantle remains unconstrained.

It has been documented that the uppermost mantle velocity reduction is even larger in poorly sedimented margins. In north Chile, for example, upper-mantle velocities in the trench-outer rise area reach values as low as 7.6 km/s [*Ranero and Sallares.*, 2004]. Offshore of Costa Rica, seismic velocities under the trench at the Moho are even lower (7.3-7.4 km/s), with velocities increasing to  $\sim 7.5$ -7.8 km/s at about 3-4 km below the Moho [*Grevenmeyer et al.*, 2007]. Offshore of south-central Chile, upper mantle velocity reduction is slightly lower and solely restricted to the trench-outer rise area (Figure 2.9a), where bending-related faulting is suggested to lead to hydration of the upper mantle [*Ranero et al.*, 2003]. Since water is required to alter mantle peridotite to serpentinite, pervasive fracturing of the entire crust is suggested for the lithosphere entering the Chilean subduction zone offshore Chiloe Island.

### 2.5.2 Water pathways

The efficiency of fluid percolation depends on the sedimentary thickness and faulting history. Faults constitute the possible water pathways but they can be blocked by insulating sediments. Therefore, slab hydration prior to subduction is believed to be largest where outcropping basement relief facilitates the flow of seawater into the crust [*Grevenmeyer et al.*, 2005]. The abyssal hill fabric inherently related to the formation process of the oceanic lithosphere at the mid-ocean ridge is well imaged just 5 km to the north of the seismic line (Figure 2.2a). Therefore; reactivation of fractures by bending-related normal faulting in

this region might be an important mechanism for plate hydration. High resolution seismic data provides evidence for some extensional faults reflected by offsets in the trench-outer rise region (Figure 2.2b), suggesting the trenchward increase of fracturing intensity. This indicates that the bending-related faulting is active in the outer rise, and it fractures the oceanic crust beneath the sedimentary bed. High resolution multibeam bathymetry shows, though, that surface-cutting faults are not visible on the seafloor along this profile (Figure 2.2a). As the insulating sediments are several hundreds of meters thick (Figure 2.2b) an efficient inflow of seawater is unlikely to explain the reduced velocities in the outer rise. However, the onset of velocity reduction in the oceanic crust is well correlated with the location of an outcropping basement high or seamount (Figures 2.2a and 2.9a), suggesting a relationship between plate hydration and basement outcrop. Seamounts or basement highs provide the necessary pathways to move huge volumes of fluid through oceanic crust over large distances, even when the crust is insulated by thick sediments [Fisher *et al.*, 2003a, 2003b]. In order to study the hydrothermal activity in the outer rise, we have directly measured heat flow values on the outer bulge offshore of Chiloe Island [Flueh and Grevemeyer, 2005]. Figure 2.11a shows the location of 10 heat flow stations immediately at the seaward flank of the basement outcrop (see also the bathymetry in Figure 2.2a). The heat flow values decrease from 100-150 to  $\sim 7 \text{ mW/m}^2$  over a distance of less than 10 km towards the trench (Figure 2.11b). We computed two predicted heat flow models using two different temperature distributions at the top of the igneous basement. In the first model basement temperature is isothermal. In the second model basement temperatures varies as a function of distance from the basement high and hence mimics cooling by inflow of cold seawater. Crucial parameters are the temperature at the basement  $T_{bas}$  and at the seafloor  $T_{sea}$ , and the thermal conductivity structure  $k$  between the basement and the seabed. We use a linear temperature gradient and the simple conductive heat transport relation:

$$q = k \frac{dT}{dz}$$

where  $q$  is the heat flow,  $dz = z_{bas} - z_{sea}$  is the thickness of the sediments, and  $dT = T_{bas} - T_{sea}$ . The sedimentary thickness comes directly from the high resolution reflection data and is plotted in Figure 2.11c. The seafloor temperature is assumed  $T_{sea} = 0^\circ\text{C}$ , and thermal conductivity  $k$  was measured in situ. Testing with different  $T_{bas(x)}$  distributions, the extreme low values toward the trench can only be predicted by the cooling model (Figures 2.11b and 2.11d). This finding suggests a very efficient inflow of cold seawater into the oceanic crust through the basement outcrop feature located just 5 km north of the profile.

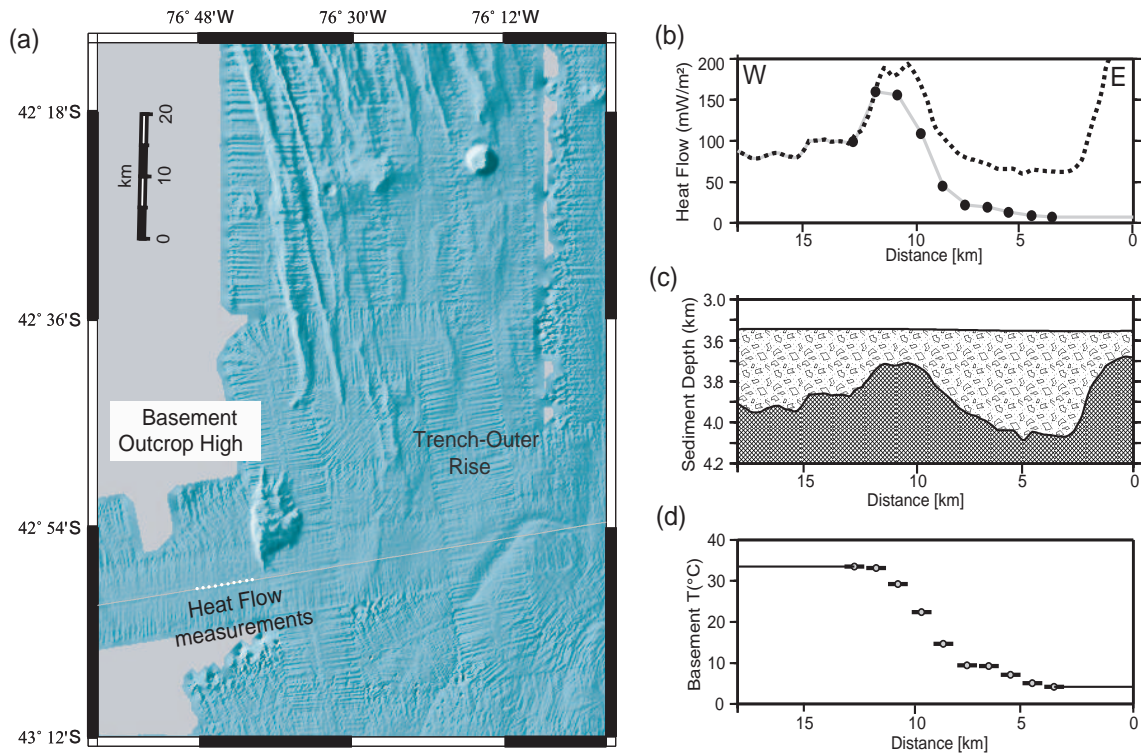


Figure 2.11: (a) Location of heat flow stations along seismic profile. (b) Heat flow measurements (black dots). Predicted heat flow values using a basement temperature of  $T_b = 40^\circ\text{C}$  (dotted line). Predicted heat flow values incorporating hydrothermal cooling (gray line). (c) Basement topography obtained from seismic reflection data. (d) Temperature distribution at the basement used in our heat flow model with cooling. For (b), (c) and (d) distance is measured from the location of the basement outcrop high.

The flanks of the high outcrop basement probably act as an important and primary entry of cold seawater into the igneous oceanic crust. This process accompanied by the opening of new cracks and activation of extensional faults due to bending-related faulting increases the permeability and hence facilitates a deeper fluid inflow, probably, reaching mantle depths, as supported by our tomographic results (Figure 2.9a). We see a number of other mounds and basement ridges imaged in the multibeam bathymetry to the north of the profile, which may act as recharge and discharge sites and therefore fuel a hydrothermal circulation in the outer rise. Cold seawater might be transported laterally between separated basement outcrops for distances of more than 50 km [Fisher *et al.*, 2003a], which implies that fluids may circulate through most of the studied trench-outer rise area. Here, bending-related faulting might increase the permeability of the oceanic crust, and consequently facilitates and reactivates hydrothermal circulation.

Moreover, the incoming plate may laterally carry water already percolated in the oceanward part of the outer rise (70-40 km from the trench axis), where plate bending is strongest, igneous basement is more exposed, and due to a higher water/rock ratio hydration might be more vigorous. In this part of the outer rise, the sedimentary thickness is comparable with the outer rise in middle America (200-400 m thick), which is highly hydrated [Ranero *et al.*, 2003]. Once cold seawater is stored in cracks and/or faults and faulting continues towards the deformation front, water trapped within the crust may migrate deeper where larger faults cut into the mantle.

### 2.5.3 Volatiles stored in the oceanic subducting lithosphere

The amount of volatiles stored in the subducting oceanic lithosphere consists mainly of three components: volatiles stored in (i) subducting sediments, (ii) in the oceanic crust and (iii) in the oceanic mantle. Recent studies, however, suggest that most of the bound water enters subduction zones within the oceanic crust and mantle [Peacock, 1990; Ranero *et al.*, 2003].

The observed crustal velocity reduction beneath the trench-outer rise is caused in part by cracks and fissures induced by plate bending. The similar trend for upper and lower crustal velocities has been observed in the northern Chile trench, which was explained as consequence of fracturing rather than hydration [e.g., Ranero and Sallares, 2004]. The amount of chemically bound water in the crust is therefore not straightforward to estimate by the magnitude of velocity reduction. Peacock [1990] concludes from chemical analysis of drill cores of oceanic crust that a 2.5-km-thick basaltic layer contains in average 2 wt. %  $H_2O$  and  $\sim 0.1$  wt. %  $CO_2$ , and a 3- to 5-km- thick oceanic gabbro layer contains roughly 1%  $H_2O$  and  $\sim 0.1$  wt. %  $CO_2$ . Hacker *et al.*, [2003] calculated a maximum water content of 1.3 wt %  $H_2O$  for partially hydrated lower oceanic crust based on a global compilation of physical properties of minerals. Carlson [2003] shows that, based on the modal mineralogy and seismic properties of oceanic diabase and gabbro samples, gabbros with velocities typical for the lower oceanic crust (6.7-7.0 km/s) already contain a mean water content near 0.5 wt%. This value could be much larger if lower oceanic crust has been altered by tectonic processes, as is probably the case in our study area.

Quantifying the amount of serpentine in subducting oceanic mantle is also difficult because relatively modest amounts of serpentine can represent a major  $H_2O$  input into the subduction factory [Peacock, 2001]. Following Carlson and Miller [2003], an approximate formula to estimate water content in the partially-serpentinized peridotites is  $w(\%) \sim 0.33\Delta V$ , where  $w$  is the water content (in weight percentage) and  $\Delta V$  is the percent difference between the observed velocity and the velocity in unaltered peridotite. The

upper mantle P-wave velocity in our study region ranges between 7.8 to 8.3 km/s, corresponding to serpentinite contents of roughly 0 to 9%; and the corresponding range of water contents of 0 to 3.0% (0 to 4 moles/m<sup>3</sup>). These values are lower compared to estimates in central America (>20 % of serpentinitization) [Ranero *et al.*, 2003], the erosional margin in northern Chile ( $\sim 17$  % of serpentinitization) [Ranero and Sallares, 2004], and offshore Costa Rica (10-25% of serpentinitization) [Grevemeyer *et al.*, 2007]. Nevertheless, the total amount of hydration and thus the total volume of fluids entering the subduction zone in south central Chile should be larger than the 9% bound in the upper mantle because of the volatile stored in the entire oceanic crust plus subducting sediments. Moreover, this degree of hydration can be even larger if the oceanic plate continues to hydrate during subduction [Ranero *et al.*, 2003].

## 2.6 Conclusions

Joint inversion of seismic refraction and wide-angle data offshore of south-central Chile yields the P-wave velocity structure of the subducting oceanic Nazca plate. This information and the tectonic features obtained from high-resolution seismic data, multibeam bathymetry and heat flow measurements suggest that the structure of the incoming plate changes systematically within  $\sim 120$  km off the trench axis as the lithosphere approaches the deep sea trench. This work leads to the following conclusions:

- The 2D-velocity model derived from tomographic travel time inversion consist of a  $\sim 5.3$  km thick oceanic crust and shows a classical mature fast-spreading P-wave velocity structure in the seaward part outside of the influence of plate bending at the trench-outer rise. Seismic analysis of  $P_n$  arrivals reveals fast uppermost mantle velocities of  $\sim 8.3$  km/s,  $>120$  km seawards of the trench. The velocity structure found in this zone indicates that the oceanic lithosphere is relatively dry and undeformed.

- Approaching the Chile trench, seismic velocities decrease, indicating an evolutionary process changing the structure of the lithosphere, likely to be related to an increase in fracture porosity and hydration of both the oceanic crust and the uppermost mantle. Reduced velocities are only located in the trench and outer-rise area. The decrease of velocities is accompanied by an increase of basement-relief roughness and also by the amount of stress induced by the plate bending.

- In spite of the thick sedimentary blanket on the incoming plate and in the trench basin, an efficient inflow of cold seawater into the oceanic crust through outcropping basement highs or seamounts is supported by anomalously low heat flow values, which are

spatially well correlated with the onset of velocity reduction in crust and upper mantle. Cold seawater might be laterally transported between high basement outcrops over large distances ( $> 50$  km) in the vicinity of the trench-outer rise area. This primary water pathway could extend to mantle depth through bending induced trench parallel normal faults, and thus cause a hydration of the upper mantle.

- Assuming that the mantle velocity reduction is produced only by hydration, serpentinization of the uppermost mantle from the outer rise to the trench axis is  $\sim 9\%$  in the uppermost 2 km of the mantle, where seismic data provide enough resolution. This degree of hydration in the uppermost mantle is about 10% less than observed in poorly sedimented margins.

In summary, seismic data of high resolution reveal a clear alteration of the oceanic lithosphere at the outer rise just prior to its subduction, showing that the alteration occurs where strong plate bending is likely to modify the large scale porosity and permeability structure of oceanic lithosphere, and simultaneously nurtures the migration of cold seawater through crustal faults down to mantle depth, resulting in hydration of both oceanic crust and upper mantle. Infiltration of cold seawater, and consequently hydration of the subducting oceanic lithosphere may also occur at heavily sedimented trenches through high basements outcrops where igneous crust is exposed.





## Chapter 3

# Effect of bending-related faulting on seismic Poisson's ratio and mantle anisotropy: a case study offshore of southern central Chile

Several trench-outer rise settings in subduction zones worldwide are characterized by a high degree of alteration, fracturing and hydration. These processes are induced by bending-related faulting in the upper part of the oceanic plate prior to its subduction. Mapping of P- and S-wave velocity structures in this complex tectonic setting provides crucial information for understanding the evolution of the incoming oceanic lithosphere, and serves as a baseline for comparison with seismic measurements elsewhere. Active source seismic investigations at the outer rise off southern central Chile ( $\sim 43^\circ\text{S}$ ) were carried out in order to study the seismic structure of the oceanic Nazca plate. Seismic wide-angle data were used to derive 2-D velocity models of two seismic profiles located seaward of the trench axis on 14.5 Ma old crust; P01a approximately parallel to the direction of spreading and P03 approximately parallel to the spreading ridge and trench axes. We determined P- and S-velocity models using 2-D traveltime tomography. We found that the Poisson's ratio in the upper crust (layer 2) ranges between  $\sim 0.33$  at the top of the crust to  $\sim 0.28$  at the layer 2/3 interface, while in the lowermost crust and uppermost mantle it reaches values of  $\sim 0.26$  and  $\sim 0.29$ , respectively. These features can be explained by an oceanic crust significantly weathered, altered and fractured. Relative high Poisson's ratios in the uppermost mantle may be likely related to partially hydrated mantle and hence serpentinization. Thus, the seismic structure of the oceanic lithosphere at the southern central Chile outer rise exhibits notable differences from the classic ophiolite seismic model ("normal" oceanic crust). These differences are primarily attributed to fracturing and

hydration of the entire ocean crust, which are direct consequences of bending-related faulting at the outer rise. On the other hand, the comparison of the uppermost mantle P-wave velocities at the crossing point between the perpendicular profiles ( $\sim 90$  km oceanward from the trench axis) reveals a low degree of  $P_n$  anisotropy ( $< 2\%$ ).

### 3.1 Introduction

Alteration and serpentinization of oceanic lithosphere entering the subduction zone has been postulated to arise from infiltration of seawater into normal faults in the trench-outer rise where oceanic plates bend upon entering subduction zones [e.g. *Peacock* 2001; *Ranero et al.*, 2003]. Here, the oceanic plate is largely altered by extensional stresses at the top of the lithosphere leading to normal faulting [*Peacock*, 2001; *Ranero et al.*, 2003], horst and graben structures [*Ranero et al.*, 2003], and associated seismicity with tensional focal mechanisms [*Chapple and Forrsyth*, 1979; *Ranero et al.*, 2006]. Additionally, bending-related faulting might open near vertical cracks and fissures, and reactivate pre-existing cracks previously created at the spreading centre. Hence, bending-related faulting modifies the porosity and permeability structure, and further provides the pathways for fluids to enter the crust and mantle [e.g., *Ranero et al.*, 2003]. This process has been evidenced by a noticeable reduction of compressional mantle velocities in the outer rise in several convergent margins. For example, reduced velocities of partially serpentinized mantle have been reported in subduction zones with little sediments such as north Chile [*Ranero and Sallares*, 2004], central Chile [*Kopp et al.*, 2004] and central America [*Grevemeyer et al.*, 2007]. In south central Chile, the trench basin is heavily filled by terrigenous sediments sourced from the southern Andes [*Thornburg and Kulm*, 1987], and hydration of the oceanic lithosphere in the outer rise area is comparatively less vigorous [*Contreras-Reyes et al.*, 2007]. Nevertheless, some regions of the outer rise are characterized by an oceanic basement exposed to the infiltration of seawater at high basement outcrops and extensional normal faults. Low compressional velocities and anomalous low heat flow values at the outer rise have been reported in this region, suggesting infiltration of seawater and perhaps hydro-alteration of the oceanic crust and upper mantle [*Contreras-Reyes et al.*, 2007].

The Poisson's ratio ( $\nu$ ) is an indicator of lithology, porosity, structure and the existence of fluids within the rock. Theory predicts that for increasing fluid-content,  $V_s$  decreases faster than  $V_p$  resulting in the increase of  $\nu$  (i.e.,  $\nu$  is more sensitive to the presence of fluids than P-wave only). Therefore, mapping of  $\nu$  would provide crucial evidence for existence of fluids within the oceanic lithosphere. Also, the presence of porosity, in the form of cracks and fissures, has a profound influence on seismic velocities and Poisson's ratios. High crack-porosity affects in disproportional amounts  $V_p$  and  $V_s$ , and it depends

on the aspect ratios of the cracks [e.g., *Shearer*, 1988; *Takei*, 2002]. Moreover,  $\nu$  is quite sensitive to the grade of metamorphism [*Christensen*, 1996], and it behaves differently depending on the mineral nature of the original rock. Differences between seismic Poisson's ratio measurements and laboratory analyses of ophiolites samples ("normal" oceanic crust) serve as an indicator to detect hydro-alteration and perturbation of the density structure of oceanic rocks. Theoretical prediction based on crack geometry and content of water have advanced in recent years [e.g., *Takei*, 2002], but their application to geological settings rich in hydrothermal and faulting activity such as the outer rise areas has been limited by the difficulty of recording high-quality shear wave arrivals. During the TIPTEQ (from The Incoming Plate to mega-Thrust Earthquake Processes) experiment [*Flueh and Grevemeyer*, 2005], P- and S- waves of high quality were recorded just 90 km oceanward from the southern central Chile trench ( $\sim 43^\circ\text{S}$ ). This data set allows us to image the uppermost  $\sim 2$  km of the mantle, and it provides an excellent opportunity to study the  $\nu$  structure at the outer rise setting. Since fracturing and hydration process dramatically affects the Poisson's ratio structure of the oceanic crust and mantle, seismic P- and S-wave tomography should be able to detect this.

Another important issue related to the evolution of seismic properties at the outer rise is the study of upper mantle seismic anisotropy. Seismic anisotropy is initially controlled by the lattice preferred orientation (LPO) of relatively dry olivine at the creation of the oceanic lithosphere at mid-ocean ridges [*Nicolas and Christensen*, 1987]. Compressional waves travel fastest along the  $a$ -axis of relatively dry olivine, which generally matches the plate motion direction. However, several experimental and theoretical studies of  $P_n$  anisotropy have postulated that the presence of water affects considerably the preferential orientation of olivine. Olivine can be recrystallized and aligned along the  $c$ -axis nearly parallel to the shear direction when a large amount of water is present [*Jung and Karato*, 2001]. In our seismic experiment, we have recorded  $P_n$  phases of good quality along two mutually perpendicularly seismic profiles, yielding additionally the opportunity to investigate  $P_n$  anisotropy at the trench-outer rise off southern central Chile.

We modelled the velocity structure of the oceanic Nazca plate near the southern central Chile trench at  $\sim 43^\circ\text{S}$  along two perpendicular seismic wide-angle reflection and refraction transects. Seismic data recorded along one of these profiles allow us to identify refracted and reflected energy of shear waves, and they were used to construct a two-dimensional S-wave velocity model, and hence estimate Poisson's ratios. We used a joint refraction and reflection travel time inversion approach to obtain accurate 2D tomography velocity models [*Korenaga et al.*, 2000], and P- and S-wave velocity model uncertainties are estimated by applying a nonlinear Monte Carlo method [*Korenaga et al.*, 2000]. Finally, uppermost

mantle velocities of the crossing profiles are compared to quantify  $P_n$  anisotropy at the outer rise, and it is interpreted within the tectonic framework.

## 3.2 Tectonic setting

The geological structure of the southern central Chile margin is controlled by the subduction of the oceanic Nazca plate beneath South America. The incoming Nazca plate (approaching South America at a rate of  $\sim 6.6$  cm/yr) subducts at a relatively high convergence azimuth of  $\sim 78^\circ\text{E}$  [Angermann *et al.*, 1999] (Figure 3.1). The part of the plate investigated here has been formed at the Chile Rise (a fast spreading mid-ocean ridge). Fracture zones (FZs) cut the Chile Rise into several segments, resulting in abrupt changes of thermal states along the plate boundary. The southern central Chile trench is filled by terrigenous sediments sourced from the Andes [Thornburg and Kulm, 1987], which are redistributed from south to north due to the slight northward dip of the trench floor [e.g., Thornburg *et al.*, 1990].

Our study area corresponds to the outer rise located between Chiloe and Guafo FZs (Figure 3.1). Here, the plate age decrease from 18.5 to 10 Ma along the Chile trench, and the half-spreading rate ranges between 45 and 35 mm/a [Tebbens *et al.*, 1997]. The plate age where the seismic profiles were positioned is approximately 12.5 Ma (Figure 3.1). The spreading centre segments bounded by Chiloe and Guafo FZs are roughly parallel to the trench strike (Figure 3.1). In the oceanward section of the outer rise, the plate is covered by a few hundred metres of pelagic sediments and turbidites (0-500 m) [Contreras-Reyes *et al.*, 2007], whereas the sedimentary cover becomes thicker towards the trench owing to the turbiditic deposits filling the trench basin with a total thickness of  $\sim 2$  km at the trench axis [Scherwath *et al.*, 2006]. Active faulting underneath the sedimentary cover at the outer rise has been evidenced by several basement-faults imaged by high resolution seismic reflection data [Contreras-Reyes *et al.*, 2007].

## 3.3 Wide angle seismic data

Seismic measurements offshore south central Chile were carried out using the German R/V SONNE during the TIPTEQ project [Flueh and Grevenmeyer, 2005]. In this paper, we present the seismic wide-angle data that were collected along two seismic profiles (P01a and P03) located seaward of the trench axis, supplemented by high-resolution swath bathymetric images of the surrounding seafloor (Figure 3.1). Seismic line P01a runs perpendicular to the Chile Rise spreading centre and approaches the deep sea trench roughly normal to the trench axis. Seismic line P03 runs parallel to the Chile trench and

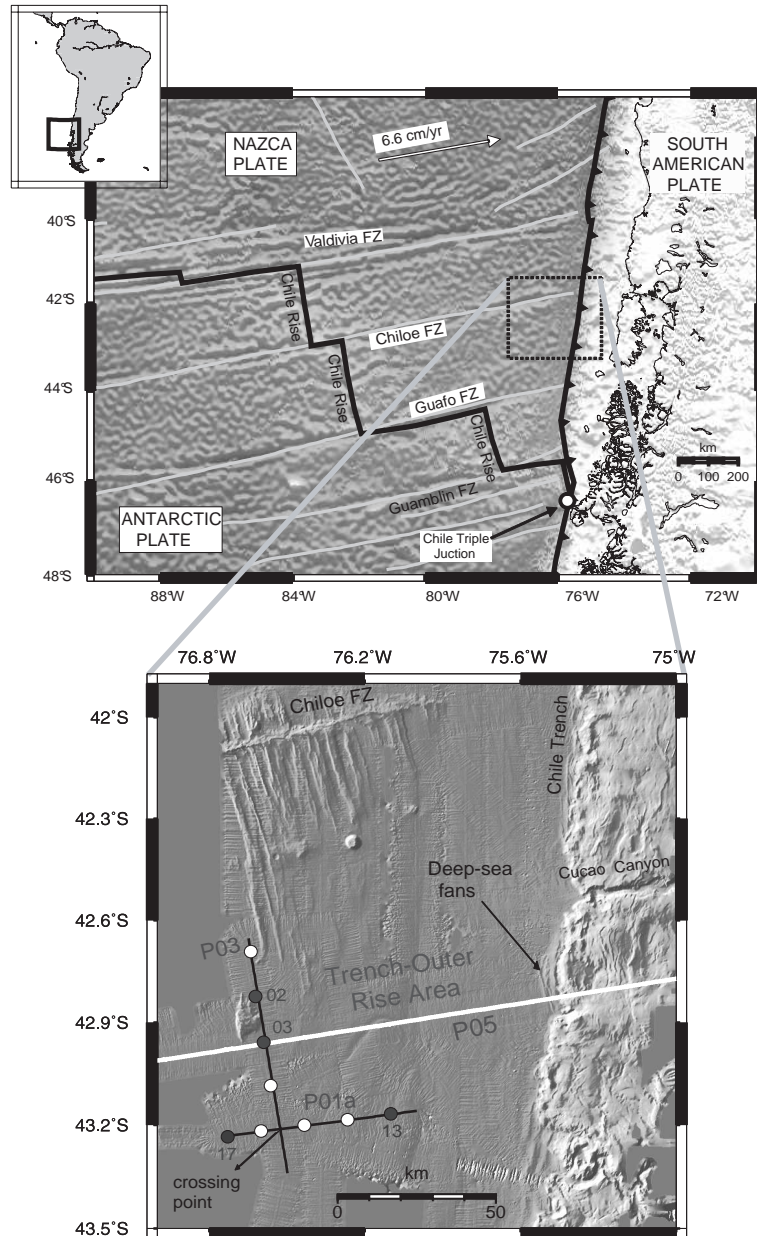


Figure 3.1: (top) Our study area is located between Chileo and Guafu Fracture Zones, where the plate age ranges from 18.5 to 10 Ma along the Chile trench. (bottom) High-resolution bathymetric image of the incoming southern Nazca plate, with locations of three wide-angle seismic profiles: P01a, P03, and P05. Black dots and station numbers indicate the four ocean bottom stations (17, 13, 02, and 03) shown in Figures 3.2 and 3.3

Chile Rise axes, and it crosses perpendicularly P01a (Figure 3.1). Shots were recorded with a total number of 9 OBS (Ocean Bottom Seismometers) [Bialas and Flueh, 1999] and OBH (Ocean Bottom Hydrophones) [Flueh and Bialas, 1996]. The seismic source for the refraction work was a cluster of 8x8-litres G-guns, providing a total volume of 64 litres for each shot. This source was fired at a time interval of 60 s, which corresponds to

an average shot spacing of  $\sim 150$  m. The record sections were interpreted after bandpass filtering and predictive deconvolution. The signal-to-noise ratio obtained for most of the stations is high (Figures 3.2 and 3.3). Crustal refractions ( $P_g$ ), Moho wide-angle reflections ( $P_mP$ ) and upper mantle refractions ( $P_n$ ) were recorded on almost all stations with excellent quality. Four examples of seismic record sections are shown in Figures 3.2 and 3.3, with their respective seismic phases identified.

The profile P01a, is a 65 km long East-West profile across the outer rise (Figure 3.1), 85 km to the north of the Guafo FZ. This profile was recorded with 5 OBH/S evenly spaced every  $\sim 8$  km. All of them returned data with a high signal-to-noise ratio. The maximum shot receiver aperture was 62 km (Figure 3.2a). Figures 3.2a and 3.2b show record sections representative of this profile with the identified  $P_g$ ,  $P_mP$  and  $P_n$  phases. The 76 km long profile P03 is located  $\sim 90$  km west of the Chile trench (Figure 3.1), which is covered by four OBSs spaced every  $\sim 8$  km. Figures 3.3c and 3.3d show record sections representative of this profile with the identified phases.  $P_mP$  and  $P_g$  phases are observed in most record sections with excellent quality.  $P_n$  arrivals are abundant in many stations (Figures 3.3c and 3.3d) with noticeable amplitude. The most striking feature of the dataset is the abundance of very strong S-wave arrivals, including Moho wide-angle reflections and P/S (S/P) conversions that can often be followed to offsets longer than 30 km. Shear-waves refractions  $S_g$  and  $S_n$  are observed in most record sections along P03, as well as S-wave Moho wide-angle reflections  $S_mS$  (Figures 3.3c and 3.3d).

Picking of the seismic phases was done manually, and picking errors were assigned on the basis of the dominant period of the phase. Detailed information regarding average picking uncertainties and number of picks for both profiles are summarized in Table 1. Typically, errors were assumed to be half a period of one arrival, to account for a possible systematic shift in the arrival identification, and were weighted according to the phase quality. Secondary  $S_g$  arrivals (arriving later than  $S_n$ ) are not evident on the data. Moho reflections  $S_mS$  are identifiable on most of the stations (Figures 3.3c and 3.3d), although with relative high uncertainty ( $>80$  ms).

### 3.4 P-wave travel time modelling scheme

We obtained the P-wave velocity-depth structure using the joint refraction and reflection travel time inversion method of *Korenaga et al.*, [2000]. This method allows jointly inverting refraction ( $P_g$  and  $P_n$ ) and reflection ( $P_mP$ ) travel times for a 2-D velocity field. Travel times and ray paths are calculated employing a hybrid raytracing scheme based on the graph method and the local ray-bending refinement [*van Avendonk et al.*, 1998].

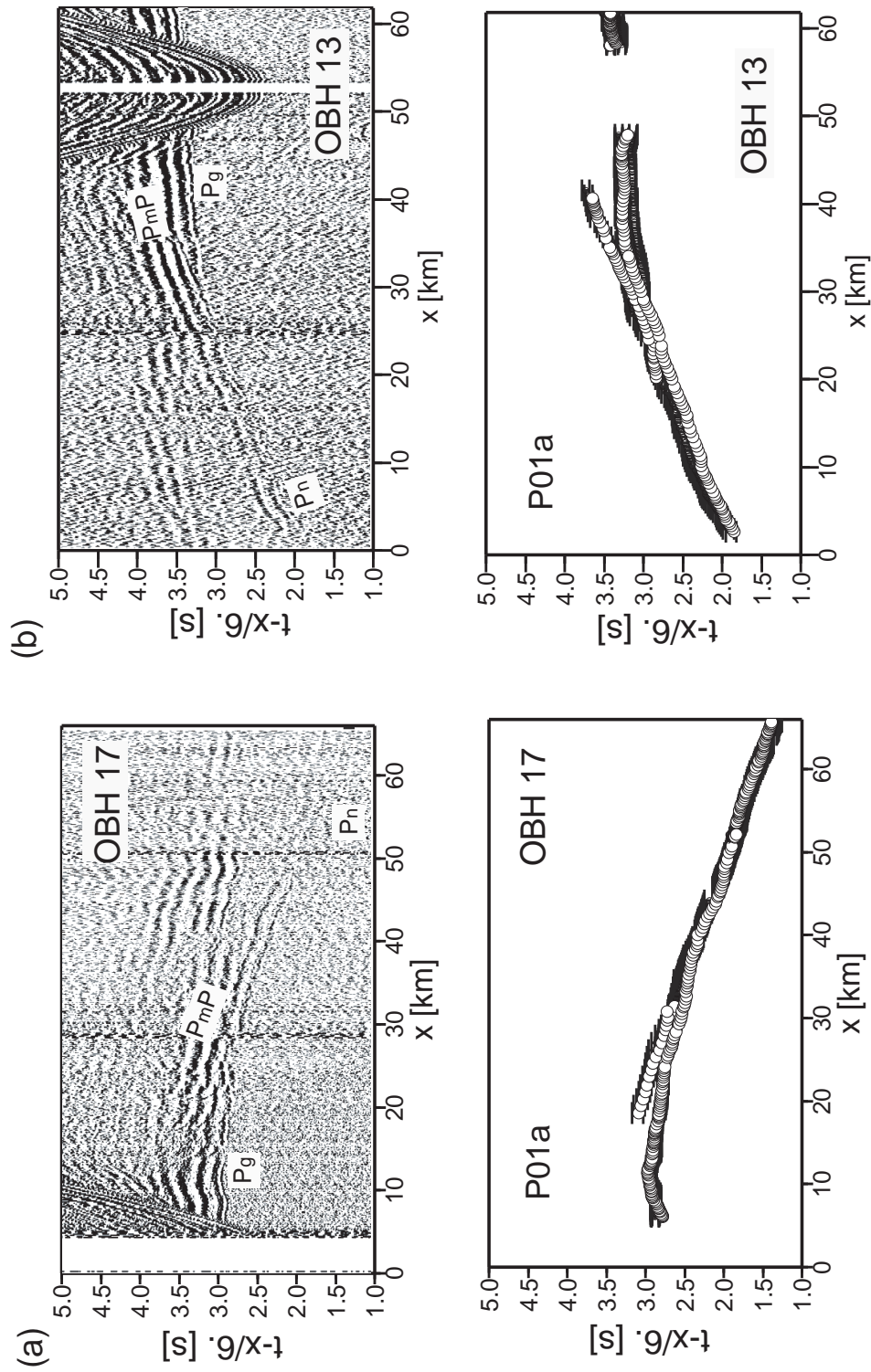


Figure 3.2: Examples of wide-angle seismic data with predicted travel times (white circles), which are computed based on the velocity model presented in Figures 3.4a, 3.4b and 3.5a. (a) OBH 17 and (b) OBH 13.

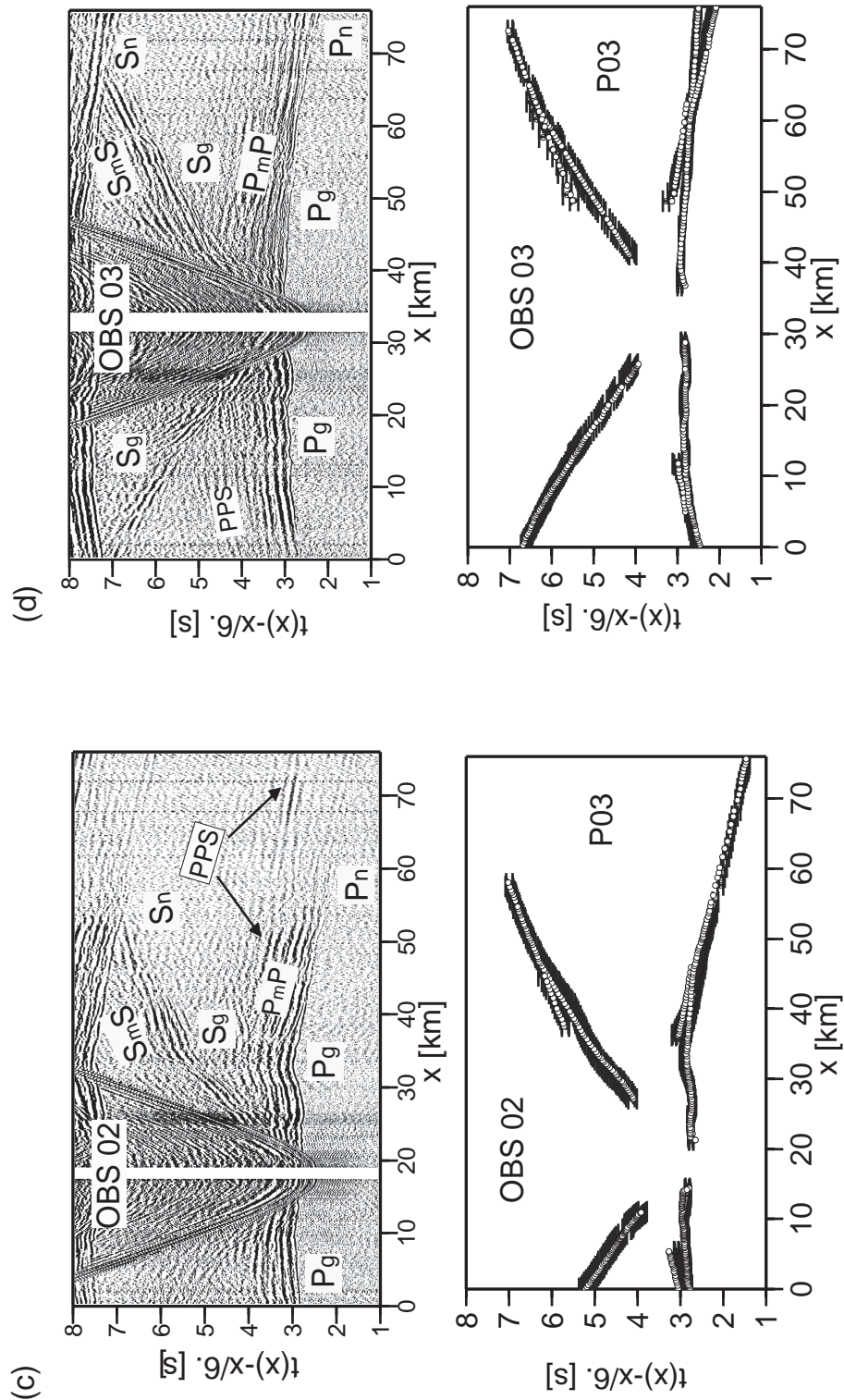


Figure 3.3: (continued) (c) OBS 02 (hydrophone component), and (d) OBS 03 (hydrophone component).

Smoothing constraints from predefined correlation lengths and optimized damping for the model parameters are employed to regularize an iterative linearized inversion [Korenaga et



*al.*, 2000]. The velocity models were constructed using four layers, (1) water, (2) sedimentary section, (3) oceanic crust and (4) upper mantle. To derive the velocity depth model, the water depths were taken from the known bathymetry, which remain fixed during the inversion. The basement was derived by a combined analysis of the reflection and refraction seismic data. Along P01a, we picked and converted the vertical incidence reflections from Two-way-Time (TWT) data [Flueh and Grevemeyer, 2005] to depth using a constant velocity of 1.7 km/s. Along P03, no streamer data are available to establish the thickness of the sedimentary sequence. The basement depth was estimated from the seismic sections at each section, taking the multiples into account where the basement reflection is relative strong. Again, a constant velocity of 1.7 km/s was used for the sediments.

The sedimentary section was also held fixed in the inversion procedure. The P-wave velocity structure for the oceanic crust was inverted using  $P_g$  and  $P_mP$  phases in order to model the velocity field and Moho depth. Once the crustal structure was determined, this section remains fixed for the subsequent upper mantle inversion, which is inverted using the  $P_n$  phases. Applying this hybrid technique not only the first arrivals are taken in account but also later refracted  $P_g$  could be used to constrain the lower crustal structure. To fix the structures obtained in the respective previous inversion, we defined 2D velocity damping functions with either large or low weighting factors depending on the zone to retain or invert in the corresponding inversion [see Korenaga *et al.*, 2000].

Horizontal grid spacing of the model used for velocity inversion is 0.5 km, whereas vertical grid spacing is varied from 0.05 km at the top of the model to 0.5 km at the bottom. Depth nodes defining the reflectors are spaced at 2 km. We used horizontal correlation lengths ranging from 2 km at the top to 10 km at the bottom of the model, and vertical correlation lengths varying from 0.4 km at the top to 2.5 km at the bottom. Several tests have shown that varying the correlations lengths by 50% does not affect significantly the overall smoothness. In addition, there is a trade-off between correlation lengths and smoothing weights, and it is possible to obtain similar results with shorter correlation lengths and larger smoothing weights. Thus, we choose short correlation lengths and large smoothing weights in order to reduce memory requirements [Korenaga *et al.*, 2000].

### 3.4.1 Oceanic crust tomography

We prepared a starting model for the crustal part by searching a 1-D velocity model that best fits the  $P_g$  and  $P_mP$  arrivals for each profile. The initial 1-D model, shown in the Appendix A, is composed of seismic layer 2 with a high vertical velocity gradient ( $>1.2 \text{ s}^{-1}$ ), and layer 3 with a low gradient ( $<0.2 \text{ s}^{-1}$ ). The starting Moho reflector was chosen as the sum of the obtained smoothed basement geometry and crustal thickness of

Table 3.1: Summary of arrivals time picks.

<sup>a</sup>Total number of picks for P-waves arrivals, <sup>b</sup>Total number of picks for S-waves arrivals, and picking uncertainties ( $\Delta T_{avg}$ ) are given.

Phase	Profile	Total picks	$\Delta T_{avg}$ , (ms)
$P_g$	P01a	1335	55
$P_mP$	P01a	623	80
$P_n$	P01a	1052	70
<sup>a</sup> Total	P01a	3010	
$P_g$	P03	1541	55
$P_mP$	P03	438	75
$P_n$	P03	873	65
<sup>a</sup> Total	P03	2852	
$S_g + S_n$	P03	2294	80
$S_mS$	P03	336	100
<sup>b</sup> Total	P03	2630	

5.3 km, which was obtained previously from processing a longer wide-angle transect P05 [Contreras-Reyes *et al.*, 2007] in the surrounding study area (see Figure 3.1 for location). Initial and final root-mean-square travel time misfits  $T_{RMS}$  for the initial models are shown in Table 2. The starting models already yield a relative good fit, with a total ( $P_g$  and  $P_mP$ )  $T_{RMS} \sim 97$  ms and  $T_{RMS} \sim 92$  ms for profiles P01a and P03, respectively. This shows that the 1-D velocity model already fit the data well since the plate geometry is quite flat along these short profiles (particularly for profile P03 which runs parallel to the trench).

In order to study the accuracy of the final model, we apply the Monte Carlo method to estimate the uncertainties of the model (see Appendix for a description of this method). Figures 3.4a and 3.4b show the average model for both profiles obtained after application of the Monte Carlo method, with the inclusion of the upper mantle part of the model as explained below.  $T_{RMS}$ ,  $\chi^2$  parameters for the final average models are summarized in Table 2. The standard deviation of the calculated velocities  $\sigma_v$  for profile P01a and P03 are displayed in Figures 3.4c and 3.4d, respectively. For the crustal part of the model along P01a,  $\sigma_v$  ranges between 0.05 to 0.2 km/s. Uncertainties of the Moho depth  $\sigma_z$  range between 0.1 and 0.3 km, average  $\sigma_z$  is less than 0.2 km. Maximum values of  $\sigma_v$  are reached at the eastern edge of the model (Figure 3.4c) where the velocity uncertainty increases to values larger than 0.15 km/s and the maximum value of  $\sigma_z$  is  $\sim 0.3$  km. In this region the

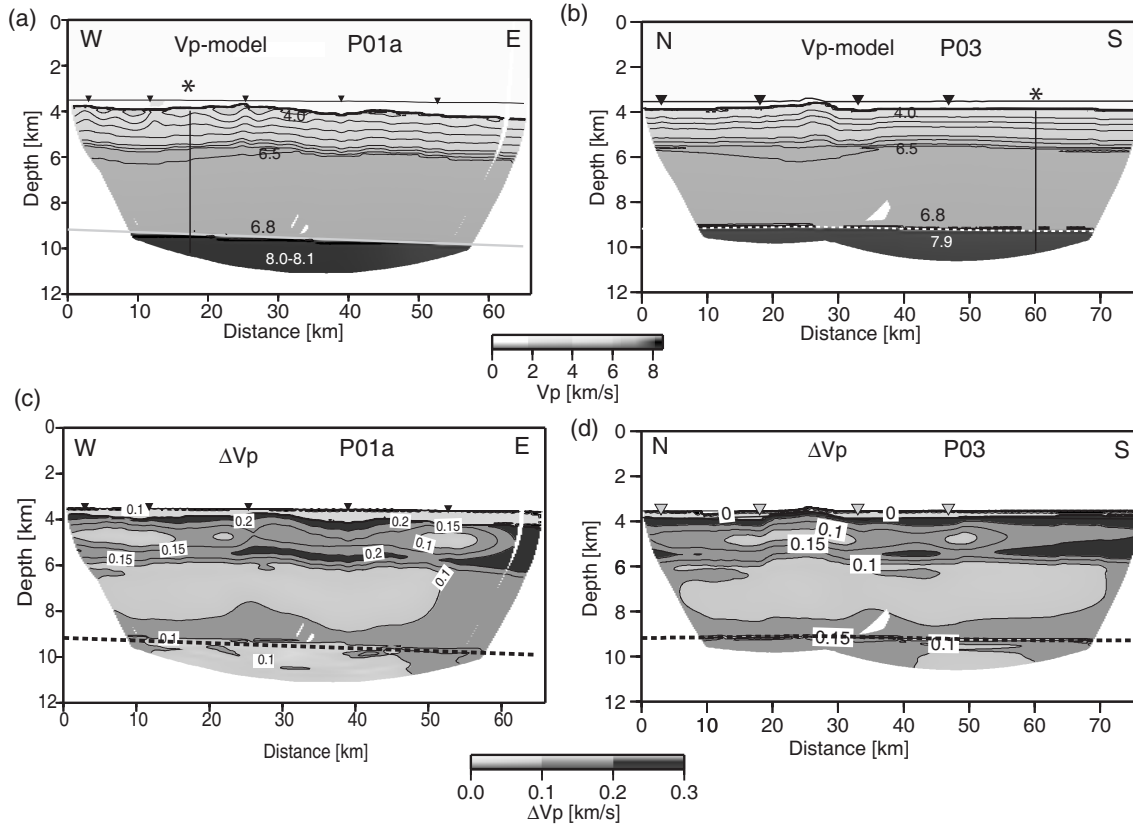


Figure 3.4: Result of P-wave velocity tomographic inversion. Final velocity model derived by averaging all Monte Carlo ensembles along (a) Profile P01a and (b) Profile P03. Asterisk in (a) and (b) denotes the location of the crossing point between P01a and P03. Corresponding standard deviation for compressional velocities along (c) P01a and (d) P03.

data coverage is reduced (Figure 3.4c). Along profile P03,  $\sigma_v$  ranges between 0.05 and 0.2 km/s and  $\sigma_z < 0.25$  km. Velocities uncertainties at the southern end of the upper crust reach values of 0.2 km/s, showing a reduced model resolution (Figure 3.4d).

### 3.4.2 $P_n$ travel-time tomography

For the subsequent tomographic inversion of the mantle refraction  $P_n$ , a "layer-stripping" procedure was chosen, preserving the average velocity model and the average Moho interface gained before. Analogously, velocity uncertainties were estimated using the Monte Carlo approach (for details see Appendix).

Along P01a, uncertainties of the upper mantle velocity in the eastern part range between 0.05 and 0.15 km/s and are lower in the seaward part ( $< 0.1$  km/s) where the crustal velocity structure and Moho reflector are well constrained (Figure 3.4c). In general, upper mantle velocity uncertainties along P03 are less than 0.2 km/s, and become lower in the southern part ( $\sigma_v \sim 0.1$  km/s) where there is good ray coverage of mantle phases.

Table 3.2: Details of seismic P-wave crustal velocity-depth inversion based on the average final models shown in Figures 3.4a and 3.4b.

$T_{RMS}$ =root-mean-square travel time misfit, and  $\chi^2$  = chi-square parameter are given

Phase	Profile	Initial Model	Initial Model	Average Final	Average Final
		$T_{RMS}$ (ms)	$\chi^2$	Model $T_{RMS}$ (ms)	Model $\chi^2$
$P_g$	P01a	96.60	2.44	58.17	0.84
$P_mP$	P01a	97.26	1.93	79.37	1.28
Total ( $P_g + P_mP$ )	P01a	96.81	2.28	65.67	0.98
$P_g$	P03	90.22	2.20	56.87	0.86
$P_mP$	P03	96.55	2.49	81.86	1.72
Total ( $P_g + P_mP$ )	P03	91.64	2.26	62.4	1.05

A detailed comparison of  $P_n$  velocities of both profiles at the crossing point (Figure 3.4) reveals that the difference between the velocities for these profiles is only 0.2 km/s, slightly more than the magnitude of the uncertainty in the velocity estimation. The faster  $P_n$  velocity is oriented in the direction of the spreading (along P01a). A similar estimation is obtained by comparing the uppermost mantle velocity obtained along profile P05 [Contreras-Reyes *et al.*, 2007] with P03 at their intersection, which is located just 30 km to the north of the crossing point between P01a and P03 (see Figure 3.1).

Table 3.3: Details of seismic P-wave mantle velocity inversion based on the average final models shown in Figures 3.4a and 3.4b.

$T_{RMS}$ =root-mean-square travel time misfit, and  $\chi^2$  = chi-square parameter are given

Phase	Profile	Average Final	Average Final
		Model $T_{RMS}$ (ms)	Model $\chi^2$
$P_n$	P01a	62.52	1.08
$P_n$	P03	60.58	1.04

### 3.5 S-wave travel time modelling scheme

Shear waves arrivals of good quality were recorded only along P03 (which is oriented parallel to the trench). Along P01a, in turn S- waves are too weak to be included in our tomographic model. In general, conversion from P-to S waves is more likely to occur where a sediment blanket is present [Lewis and McClain, 1977], since cementation and

infilling of cracks result in an increase of S-wave velocity and decrease shear attenuation enough for an efficient P- to S-wave conversion. The mature oceanic crust in our study area is covered by a sequence of 0-500 m of sediments, but the P- to S-wave conversion is preferentially efficient in the direction parallel to trench and inefficient perpendicular to it. Probably, the main reason is the topographic disturbances which parallel to the trench are small compared to the characteristic wavelength of the affected S-waves modes. Towards the trench, several extensional faults striking parallel to the trench axis (Figure 3.7) result in a basement surface quite heterogeneous. Thus, the P- to S-wave conversion in the sediment-crust boundary near the trench is practically absent.

To obtain the shear velocity structure we assumed that the P- to S-wave conversion took place at the sediment/crust interface, and we fixed the layer interfaces of the P-wave velocity structure (sediment-crust, layer 2/3 and Moho boundaries) obtained previously [e.g, *Mithal and Mutter, 1989*]. Thus, only S-velocities values were altered in the tomographic inversion. Sedimentary velocities are not inverted in the seismic tomography, but they were estimated using the PPS wave modes. The PPS wave modes travel through the sedimentary layer and basement as a P-wave and they are converted to an S-wave at the sediment/crust interface, and hence is recorded as an S-wave. Its time delay to the normal P-wave mode is directly related to the time difference in P- and S-wave velocity of the sediment section beneath the OBS station [e.g., *Trummer, 2002*]. We observed PPS phases on most of the stations, which exhibit the same apparent velocity as the first arrival P-phase but with a relative constant time delay of roughly 1s (Figures 3.3c and 3.3d). Using the geometry and velocity field of the sedimentary section gained in the P-wave modelling, the estimated S-wave velocity is therefore  $\sim 0.5$  km/s in the sediments. The average picking uncertainty of PPS phases is 80 ms. Studying the travel time error by perturbing S-wave velocities, we estimated an overall accuracy for shear wave velocities for the sedimentary layer of 0.05 km/s.

Table 3.4: Details of seismic shear wave arrivals inversion based on the average final model shown in Figure 3.5a.

$T_{RMS}$ =root-mean-square travel time misfit, and  $\chi^2$  = chi-square parameter are given

<b>Phase</b>	<b>Average Final Model <math>T_{RMS}</math> (ms)</b>	<b>Average Final Model <math>\chi^2</math></b>
$S_g + S_n$	72.70	0.95
$S_m S$	62.52	0.48
Total ( $S_g + S_n + S_m S$ )	71.88	0.89

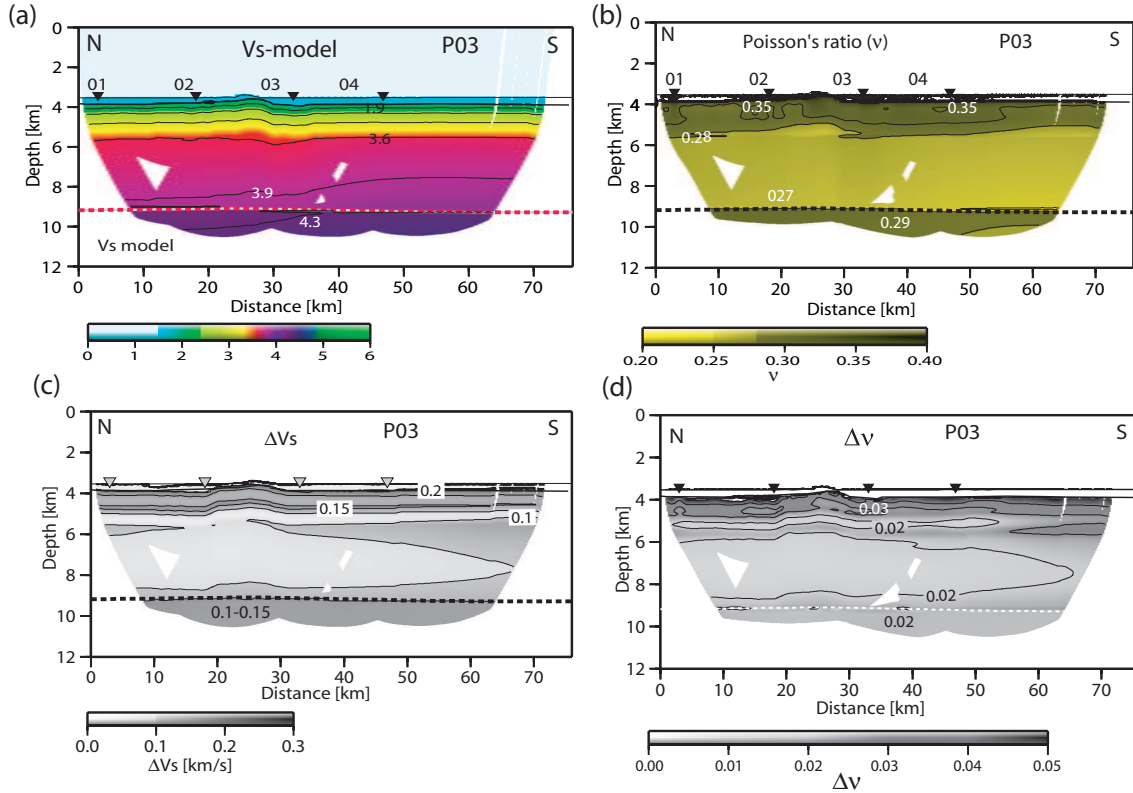


Figure 3.5: (a) Final shear wave velocity model derived by averaging all Monte Carlo ensembles. (b) Poisson's ratio two-dimensional model derived from  $V_p$  (Figure 3.4b) and  $V_s$  (Figure 3.5a) models at the same ray-coverage intersection. (c) Standard deviation for S-wave velocity model. (d) Standard deviation for Poisson's ratio model.

To model the oceanic crust and upper mantle simultaneously, we inverted only the first refracted shear wave arrivals ( $S_g$  and  $S_n$ ) and Moho reflections  $S_mS$ . We used the PSP modes, where the signal travels as a P-wave through the sedimentary layer but as an S-wave through the oceanic crust ( $S_g$  and  $S_mS$ ) and upper mantle ( $S_n$ ). Picking uncertainties and number of picked arrivals of these phases are shown in Table 1. Starting model preparation and analysis of the uncertainties for the S-wave velocity model are described in the Appendix A. Figures 3.5a and 3.5c display the final average S-wave velocity model and its standard deviations, respectively.  $T_{RMS}$  and  $\chi^2$  parameters are summarized in Table 4. Upper crustal velocity uncertainties range between 0.05 and 0.25 km/s, with a mean value of  $\sim 0.1$  km/s. In general,  $\sigma_v$  through the lower crust is  $< 0.15$  km/s, its maximum where the poorest ray-coverage is located at the southern edge. Velocity uncertainties in the upper mantle reach values of 0.1-0.2 km/s.

In Appendix B and C, we present two independent synthetic tests in order to study the robustness of our tomographic results. First, we study the travel time sensitivity of the uppermost shear wave velocity by using classical 2D forward modelling (Appendix B).

Second, we modeled the most prominent amplitude pattern of the seismic data by using the method of Reflectivity (Appendix C).

### 3.6 Poisson's ratio

The Poisson's ratio  $\nu$  is the ratio of transverse contraction strain to longitudinal extension strain in the direction of stretching force.  $\nu$  is related to the compressional wave velocity  $V_p$  and shear wave velocity  $V_s$  via

$$\nu = \frac{\left(\frac{V_p}{V_s}\right)^2 - 2}{2\left[\left(\frac{V_p}{V_s}\right)^2 - 1\right]} \quad (3.1)$$

and its standard error  $\Delta\nu$  is given by:

$$\Delta\nu = \pm \frac{\left(\frac{V_p}{V_s}\right)^2}{2\left[\left(\frac{V_p}{V_s}\right)^2 - 1\right]} \sqrt{\left(\frac{\Delta V_p}{V_p}\right)^2 + \left(\frac{\Delta V_s}{V_s}\right)^2} \quad (3.2)$$

where  $\Delta V_p$  and  $\Delta V_s$  are the uncertainties of P- and S- wave velocities, respectively.

We used (3.1) to compute  $\nu$  directly from the obtained P and S wave velocity structure at a common ray-coverage, which is given by the overlap of the ray-coverage of P- and S-wave velocity models (see Figures 3.4b, 3.5a and 3.5b). Uncertainties of the Poisson's ratio are computed using (3.2) and they are plotted in Figure 3.5d. Usually  $\Delta V_p < \Delta V_s$ , and thus  $\Delta\nu$  is very sensible to the uncertainties of the S-wave velocity model. Characteristic values of  $\Delta\nu$  range between 0.01 and 0.03, its maximum at the top of the oceanic crust (Figure 3.5d).

## 3.7 Results and Discussion

### 3.7.1 Seismic structure of the oceanic lithosphere

#### Sediments

The top of the incoming plate is covered by a mixture of pelagic and terrigenous sediments with compressional velocity of 1.7 km/s and shear wave velocity of 0.5 km/s, resulting in a Poisson's ratio of  $\sim 0.48$ . The thickness of the sedimentary layer varies from 0 m (where igneous basement is exposed) to  $\sim 500$  m at the eastern most section of profile

P01a.

In-situ measurements of shear wave velocity in marine sediments at less than 100 meters below seafloor give  $\nu$  values ranging from 0.46 to 0.49 [Hamilton, 1976]. Wilkens *et al.*, [1992], based on inversion of S-wave velocities from full waveform acoustic logs recorded in partially lithified calcareous oozes, have determined Poisson's ratios of 0.35-0.39. We interpreted the Poisson's ratio of 0.48 for the sedimentary layer offshore of southern central Chile as a mixture-sequence of pelagic sediments and turbidites with rich water content.

### Upper crust

Below the sediments, the velocity structure roughly follows the basement topography and a  $\sim 1.7$  km thick layer with compressional velocities between  $4.0 \pm 0.2$  km/s and  $6.5 \pm 0.15$  km/s were obtained. Thus, seismic P-wave velocity is reduced by  $\sim 0.5$  km/s with respect to normal oceanic crust of that age [Grevemeyer and Weigel, 1996; Grevemeyer *et al.*, 1999]. The shear-wave velocity at the top of the upper crust is  $1.9 \pm 0.2$  km/s, hence the Poisson's ratio is  $0.33 \pm 0.03$ . S-wave velocity increases to  $3.6 \pm 0.15$  km/s and  $\nu=0.27 \pm 0.02$  at the 2/3 layer boundary (Figure 3.5b). The seismic structure is consistent with oceanic layer 2 with the typical sequence of extrusive basalts on top of a sheeted dikes complex [e.g. Vera *et al.*, 1990]. High  $V_p$ -gradient ( $\sim 1.5 \text{ s}^{-1}$ ) and  $V_s$ -gradient ( $\sim 0.9 \text{ s}^{-1}$ ) across seismic layer 2 is consistent with the rapid decrease of porosity, and consequently the decrease of  $\nu$  with depth (Figure 3.5b).

Lithology, degree of hydro-alteration, geometry and density of cracks influence the behavior of  $\nu$ . Discrepancies exist between seismic Poisson's ratio measurements and laboratory analysis of ophiolites samples. For example, several in-situ experiments have shown that the uppermost 200-300 m of the oceanic crust are consistent with Poisson's ratio of 0.32-0.38, which exceed values obtained for normal ocean basement samples ( $\nu=0.30$ ) [Hyndman, 1979; Salisbury and Christensen, 1978; Collier and Singh, 1998]. Spudich and Orcutt, [1980] determined high values of  $\nu$  (0.32-0.38) in the uppermost crust, which were interpreted as a high degree of porosity. High Poisson's ratios above 0.30 in the upper crust are typical for young oceanic crust due to its high porosity in the form of cracks, fissures, breccias and talus [e.g., Hyndman, 1979]. Sediment thickening and filling of cracks by secondary minerals during crustal aging result in an increase of both P- and S-wave velocities [e.g., Wilkens *et al.*, 1991], and a decrease of  $\nu$ , as shown in laboratory studies [e.g., Shaw, 1994]. However, the mature oceanic crust ( $\sim 12.5$  Ma) offshore south central Chile is characterized by active faulting beneath the "thick" sedimentary cover [Contreras-Reyes *et al.*, 2007], reactivating fluid circulation and creating



new cracks and re-opening old ones. Thus, additional pore space is created and hence porosity is increased at the outer rise owing to strong bending-related faulting. In this in-situ experiment, we detected Poisson's ratios of  $\sim 0.33$  at the top of seismic layer 2, which are in close agreement with altered and fractured upper oceanic crust (Figure 3.5b).

With increasing depth  $\nu$  decreases to values of  $\sim 0.28$  at the base of the upper crust (Figure 3.5b). *Au and Clowes*, [1984] detected seismic Poisson's ratios of 0.22-0.26 at 1-1.5 km crustal depth, which are noticeably lower than for metamorphosed basalts (0.26-0.32) occurring at these depths in ophiolites. This difference between rock-laboratory and seismic measurements can be explained by crack theory. *Shearer* [1988] predicts that the Poisson's ratio is increased by the presence of thin cracks (aspect ratio  $< 0.005$ ) and is decreased by thick cracks (aspect ratio  $> 0.5$ ). At low depths both types of cracks are present, but thin cracks have a much greater effect on elastic properties than thick cracks [Shaw, 1994]. In contrast, Poisson's ratio is less sensible to porosity increment of thick cracks at shallow depths. At greater depth most of the thin cracks are closed and thick cracks dominate the behavior of Poisson's ratio, resulting in its reduction. *Shaw* [1994] interpreted the depth pattern of cracks closures to be related to the aging of the oceanic crust. In young crust thick cracks remain unsealed at depths of 1-1.5 km [Shearer, 1988], and they gradually become sealed by hydro-mineral deposition as oceanic crust ages and sedimentary cover becomes thicker [e.g., Shaw, 1994].

Our estimated Poisson's ratios of  $\sim 0.28$  at the base of layer 2 ( $\sim 1.7$  km beneath sediments), fall between values of metamorphosed basalts (Figure 3.6b). It is noteworthy that given the complexity and heterogeneity of crack-geometry perturbation caused by bending-related faulting, several scenarios might produce identical Poisson's ratio distribution, e.g. fracturing and hydration acting simultaneously in the upper crust. On one hand, if active normal-faulting is able to increase the number of thick cracks, then according to the model of *Shaw* [1994]  $\nu$  should decrease. On the other hand, if bending-related faulting allows the infilling of thick cracks by fluids, then  $\nu$  should increase, contrasting the effect of thick cracks. Thus, hydro-fracturing effects may overprint Poisson's ratio values of metamorphosed basalts. Since bending-related faulting modifies heterogeneously the bulk porosity, different distributions of distinct types of cracks should result in disproportional variations of the  $\nu$  structure.

### Lower crust

The upper crust overlies a  $\sim 3.6$  km thick layer with compressional velocities increasing from  $6.5 \pm 0.1$  km/s at the top of the layer to  $6.8 \pm 0.1$  km/s at the bottom. Uppermost lower crust S- wave velocities are  $3.6 \pm 0.15$  km/s and reach  $3.8 \pm 0.15$  km/s at the Moho,

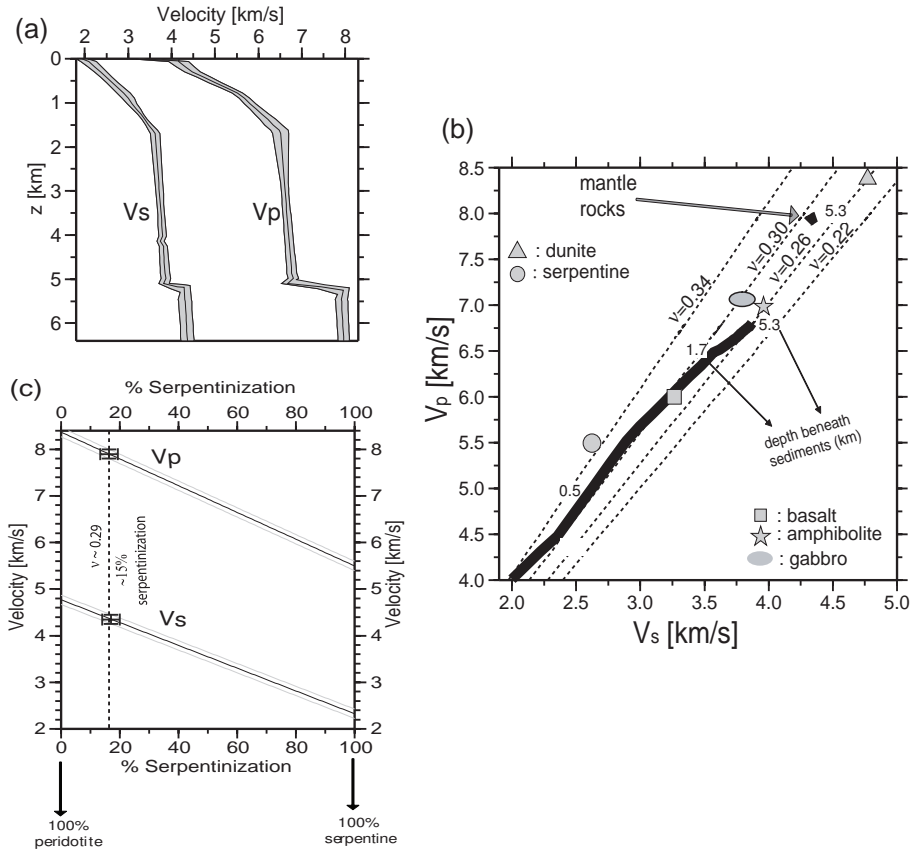


Figure 3.6: (a) Extracted compressional and shear velocity-depth profile at  $x \sim 40$  km along profile P03. Grey area represents the velocity-uncertainty of the models. (b) P velocity versus S velocity paths for P03 (black solid line). Paths for constant Poisson's ratio (dot lines), which form straight lines in the  $V_p - V_s$  plane, are plotted at intervals of 0.04.  $V_p$  and  $V_s$  values for dunite, serpentinite, basalt, amphibolite, and gabbro were taken at 200 MPa [Christensen, 1996]. (c) Trend of  $V_p$  and  $V_s$  as a function of degree of serpentinization based on compilation of laboratory mantle peridotite [Christensen, 1996].

resulting in a Poisson's ratio decreasing from  $0.28 \pm 0.02$  to  $0.26 \pm 0.02$  within the lower crust (Figure 3.5b). The base of the lower crust is constrained by Moho reflections ( $P_mP$ ) at about 5.3 km depth below the basement.

This seismic structure corresponds to oceanic layer 3, generally associated with gabbro and layered gabbro rocks (layer 3A and 3B). However, noticeable reduced lowermost crustal P-wave velocities ( $< 7.0$  km/s) suggest the likely presence of hydrous minerals such as chlorite and amphibolites [e.g., Hess, 1962; Christensen and Salisbury, 1975]. Furthermore, Carlson and Miller [2004] pointed out that even in gabbros with top and bottom compressional velocities typical of seismic layer 3 (6.7 and 7.0 km/s, respectively) contain already 5-15% alteration products, including 5-15 % amphibole and 0-5 % phyllosilicates. Our estimates (6.5 and 6.8 km/s) are consistent with gabbros of high degree of metamor-

phism. *Salisbury and Christensen* [1978] determined  $\nu$  values ranging from 0.26 to 0.31 based on experimental measurement of an ophiolite complex. *Christensen* [1996] reported  $\nu$  values of 0.29 for gabbro decreasing with metamorphism to values as low as 0.26 for amphibolite facies rocks, based on measurements of  $V_p$  and  $V_s$  to hydrostatic pressures of 200 MPa.

Fracturing and population of cracks might also be partially responsible for the observed velocity reduction [e.g., *Ranero and Sallares, 2003*]. Old crustal cracks originally created at the spreading crest might be re-opened and new ones created by bending-related faulting near the trench, producing a large population of cracks at lower crustal depths. These cracks can be filled by infiltrated seawater via outer rise hydraulic faults, resulting in the hydro-alteration of the oceanic gabbro. Figure 3.6b shows the reduction of  $\nu$  within layer 3 between depths of 1.7 and 5.3 km beneath sediments, reaching a value of  $\sim 0.26$  at the base of the crust. This value is clearly lower than laboratory measurements of gabbro rocks ( $\sim 0.29$ ) (Figure 3.6b). According to the model of *Shaw* [1994], cracks of both small and large aspect ratios are closed at lower crustal depths, restoring Poisson's ratio values to be consistent with laboratory measurements (0.28-0.29). Our results near the Chile trench, however, show a decrease of  $\nu$  rather than an increase within the lower crust (Figure 3.6b). This implies that fracturing and/or hydro-alteration at lower crustal depths occurs, regardless that our seismic profile is emplaced on mature oceanic crust of  $\sim 12.5$  Ma, where usually hydrothermal alteration is largely confined to upper crustal depths [e.g., *Carbotte and Scheirer, 2004*].

### Uppermost mantle

Uppermost mantle  $V_p$  of  $7.9 \pm 0.1$  km/s and  $V_s$  of  $4.3 \pm 0.15$  km/s were detected along P03, which are lower than dry peridotite ( $V_p > 8.1$  km/s and  $V_s > 4.6$  km/s). Thus, along the Moho discontinuity a rapid increase of  $\nu$  from  $0.26 \pm 0.02$  at the lowermost crust to  $0.29 \pm 0.02$  at the uppermost mantle is observed (Figure 3.6b). *Hyndman* (1979) reported ratios of 0.24 ( $V_p/V_s = 1.71$ ) with a compressional velocity of 8.4 km/s for mantle peridotite. Based on laboratory samples of ophiolites, *Christensen* [1996] describes the transition from mafic to ultramafic igneous intrusions as a decrease of the Poisson's ratio reaching a value of  $\sim 0.26$  ( $V_p/V_s = 1.76$ ) immediately below the Moho. This  $\nu$  reduction is due primarily to increasing dry olivine content. In the case of partially serpentinized mantle, however, the behavior of  $\nu$  is totally different, as Poisson's ratio increases abruptly where peridotite or dunite is hydrated. For example, serpentinization of dunite forces  $\nu$  to change from an average 0.24-0.26 in peridotite to an average of 0.35 in serpentinite [*Christensen, 1996*]. Partially serpentinized dunites and peridotites have Poisson's ratios that fall between these limiting values.

Figure 3.6c shows a compilation of  $V_p$  and  $V_s$  for mantle peridotite as a function of degree of serpentinization based on laboratory results of *Christensen* [1996]. The data were taken at 200 MPa, and the average zero-serpentine for this suite of laboratory data is about 8.4 km/s and 4.7 km/s for  $V_p$  and  $V_s$ , respectively. Our new tomographic results exhibit slightly reduced  $V_p$  and  $V_s$ , and high Poisson's ratios ( $\sim 0.29$ ) for mantle rocks reflecting a partial degree of hydration (Figures 3.6b and 3.6c). These values correspond to moderately hydrated mantle composition with a degree of serpentinization of 10-20% (Figure 3.6c). Since water is required to alter mantle peridotite to serpentinite, pervasive fracturing of the entire crust is suggested for the lithosphere entering the Chilean subduction zone off Chiloe Island.

### 3.7.2 Hydrothermal activity at the southern central Chile outer rise

The relative young oceanic Nazca plate created at the Chile Rise is characterized by the absence of a strong outer bulge oceanward from the trench axis and by a thick sedimentary cover. In some parts of the outer rise area shown in our bathymetric map, pelagic sediments and turbidites obscure normal outer rise faults (Figure 3.7a). Since sediments are thought to limit seawater from communicating with the underlying oceanic crust, hydrothermal activity should be absent. However, seismic reflection data show some faults which expose basement, and also rough basement topography (Figure 3.7b), suggesting that bending-related faulting pervasively fractures the oceanic crust beneath the sedimentary blanket and likely creates pathways for seawater into the uppermost brittle lithosphere. In addition, basement outcrops also expose igneous basement resulting in an easy percolation of cold seawater through their flanks. Infiltration of cold sea water into the crust has been reported in the working area [*Contreras-Reyes et al.*, 2007], where extremely low heat flow values in the outer-rise ( $\sim 7 \text{ mW/m}^2$ ) are readily explained with the inflow of cold seawater through a basement outcrop marked in Figure 3.7a. The seismic profile P03 passes next to the high basement outcrop and anomalous high Poisson's ratios in the oceanic crust in mantle are observed. Thus, hydration mechanisms in the oceanic plate provide a natural explanation for the velocity and Poisson's ratio anomaly.

### 3.7.3 $P_n$ anisotropy at the outer rise

The genesis of the oceanic lithosphere involves active mantle flow, resulting in ductile deformation and intense crystal anisotropy of olivine within the uppermost mantle [*Nicolas and Christensen*, 1987]. Seismic anisotropy therefore is controlled by the lattice preferred orientation (LPO) of relatively water-poor olivine [*Nicolas and Christensen*, 1987]. P-waves travel fastest along the  $a$  axis of relatively dry olivine. Hence, the direction of the fastest P-wave velocity is usually assumed to indicate the flow direction in the

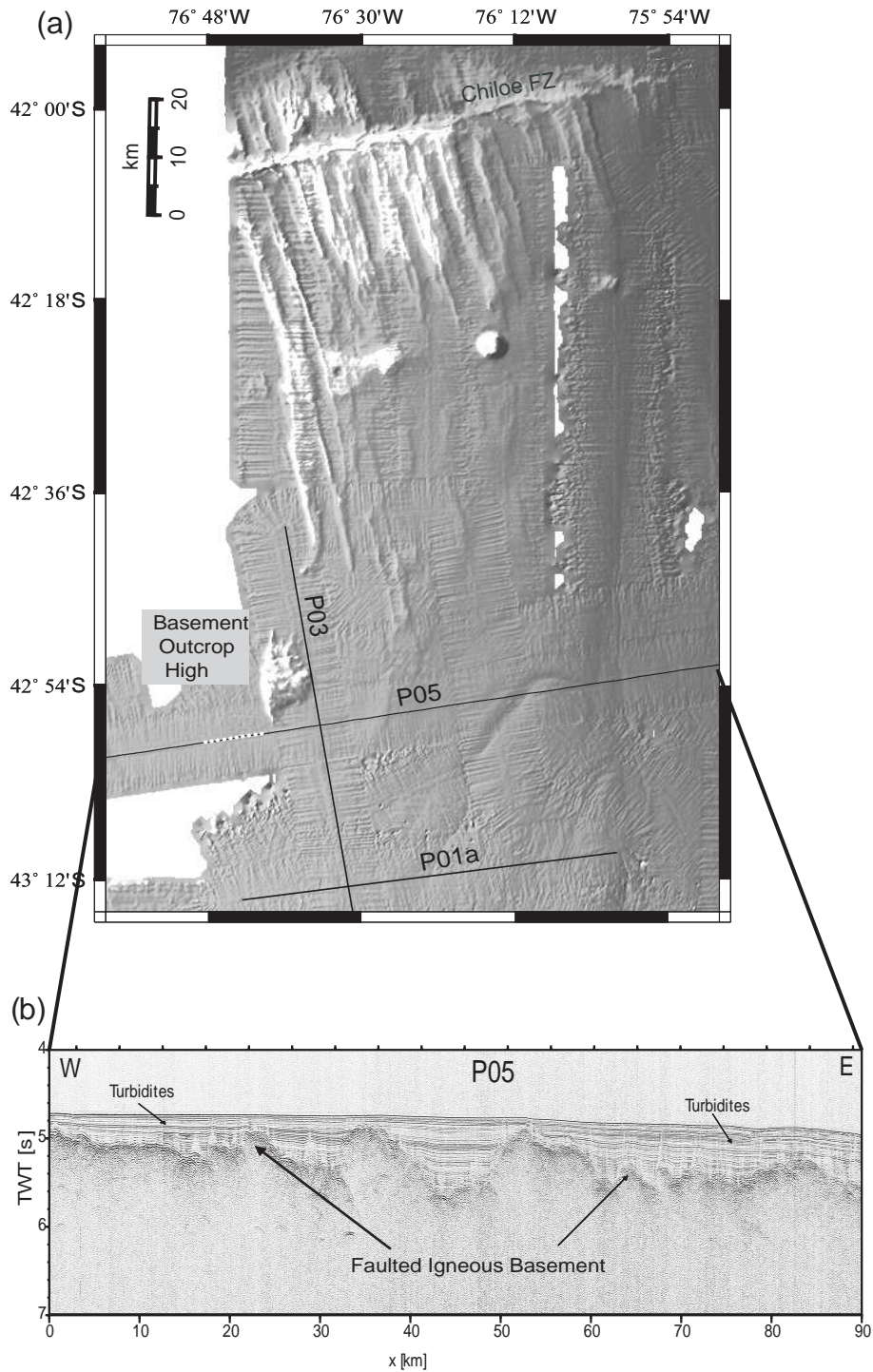


Figure 3.7: (a) High-resolution bathymetric image of the southern central Chile outer rise. (b) Multichannel reflection data reveals active faulting underneath the sedimentary cover, as is shown by extensional bending faults, which cut the oceanic crust and expose igneous basement to direct contact with seawater.

mantle [e.g., Zhang and Karato, 1995]. This assumption is not always valid, however, in environments with a large stress field and high water-content, such as subduction zones

[*Jung and Karato, 2001*]. Experiments of *Zhang and Karato* [1995] show that at large strain, the main  $a$  axis orientation no longer follows the finite strain ellipsoid but rotates toward the shear direction. This process is also accompanied by intensive dynamic recrystallization. In addition, the presence of water can alter the relative strengths of olivine slip planes and change how it deforms [*Jung and Karato, 2001*], and consequently results in variation of both degree and orientation of seismic anisotropy. Mineral physics studies showed that crystal anisotropy of wet peridotite is unusually low, despite of considerable texture strength [*Precliz, 2005*]. Furthermore, the hydration process enhances anisotropic deformation of olivine, increases with the amount of water and re-orientes the fast wave speed orientation with the  $c$ -axis nearly parallel to the shear direction [*Jung and Karato, 2001*].

*Clowes and Au* (1982), in an in-situ seismic experiment, reported strong  $P_n$  anisotropy of 10 % offshore western Canada (seaward from the trench), with a fastest speed of 8.3 km/s aligned parallel to the direction of the spreading and slowest of 7.5 km/s oriented approximately parallel to the spreading ridge. The difference was attributed to azimuthal velocity anisotropy of the type normally found in the Pacific basin. *Christensen and Salisbury* [1979] performed laboratory analyses of 15 ultramafic tectonite samples from an ophiolite complex, and they estimated a compressional seismic anisotropy of 6 % with a fastest upper mantle velocity of 8.7 km/s parallel to the inferred spreading direction, and the slowest of 8.2 km/s perpendicular to this direction. *Christensen and Smewing* [1981] provide empirical results of harzburgites samples from the lower ultramafics of the Oman ophiolite. They found  $P_n$  anisotropy as high as 8 %. Our in-situ  $P_n$  anisotropy estimation of  $\sim 2\%$  at the trench-outer rise area is considerably lower than the measurements mentioned above.

Fast  $P_n$  velocities of  $> 8.3$  km/s were detected  $> 200$  km seaward from the southern central Chile outer rise [*Contreras-Reyes et al., 2007*], reflecting a dry-peridotite composition of the oceanic mantle. However, towards the trench uppermost mantle velocities become systematically slower ( $\sim 7.8$  km/s) indicating an evolutionary process and alteration of the seismic properties of the oceanic lithosphere in the vicinity of the trench [*Contreras-Reyes et al., 2007*]. We speculate, therefore, that tectonic and hydration processes near the trench decrease the difference between compressional velocities along the fast and slow axis of olivine or the partially serpentinized zones, and we anticipated that the fastest P-wave velocity orientation might be rotated while the plate approaches the trench, where hydrothermal circulation and stress magnitude increase. This interpretation is supported by laboratory experiments on mantle rocks [*Zhang and Karato, 1995; Jung and Karato, 2001*].

### 3.7.4 Conclusions

Joint inversion of seismic refraction and wide-angle reflection data at the southern central Chile outer rise yields the P- and S-wave velocity structure of the incoming oceanic Nazca plate. We presented new results showing the impact of bending-related faulting on seismic properties of the oceanic subducting lithosphere prior to its subduction. This work leads to the following conclusions:

- The oceanic Nazca plate at the southern central Chile outer rise is covered by a sequence of oceanic pelagic sediments and turbidites of 0-400 m, with a Poisson's ratio of  $\sim 0.48$ . Frequently, the igneous basement with its extensional normal faults is exposed to direct contact with cold seawater through high basement outcrops.

- The upper oceanic crust is characterized by relatively low  $V_p$ , low  $V_s$ , and high Poisson's ratios ranging between  $\sim 0.33$  at the top of the crust and  $\sim 0.28$  at the layer 2/3-interface. These high values of  $\nu$  are interpreted to be the cause of high hydro-activity and high degree of porosity in the form of cracks and fissures.

- The trend of Poisson's ratio within the lower crust is characterized by a slight decrease of  $\nu$  from the top of the lower crust down to the Moho (where  $\nu$  reaches values of  $\sim 0.26$  at the bottom of the crust). The observed decrease of  $\nu$  is interpreted as the likely presence of a high degree of fracturing and/or hydro-alteration at lower crustal depths.

- Anomalously high Poisson's ratios in the upper mantle of  $\sim 0.29$  are likely caused by partial hydration, since bending-related faulting may breach the entire oceanic crust providing the necessary water-pathways up to upper mantle depths. Based on laboratory seismic velocity measurements of mantle peridotite and serpentinite, the degree of serpentinization is 10-20%.

- Comparison of the uppermost mantle velocities at the crossing points of perpendicular profiles reflects low degree of  $P_n$  anisotropy ( $< 2\%$ ). Our in-situ refraction seismic experiment detected much lower degree of anisotropy than laboratory measurements of ophiolite complex and refractions experiments performed seaward from the outer rise area.





## Chapter 4

# Seismic structure of the incoming/subducting oceanic Nazca plate offshore the southern Arauco Peninsula, Chile at $\sim 38^{\circ}$ S

A joint interpretation of swath bathymetric, seismic refraction, wide-angle reflection and multi-channel seismic data was used to derive a detailed tomographic image of the Nazca-South America subduction zone system offshore southern Arauco peninsula, Chile ( $\sim 38^{\circ}$ S). Here, the trench basin is filled with up to 2.2 km of sediments and the Mocha Fracture Zone (FZ) is obliquely subducting underneath the South American plate. The velocity model derived from the tomographic inversion consists of a  $\sim 7$ -km-thick oceanic crust and shows P wave velocities typical for mature fast spreading crust in the seaward section of the profile, with uppermost mantle velocities  $> 8.4$  km/s. In the trench-outer rise area, the top of incoming oceanic plate is pervasively fractured and likely hydrated as shown by extensional faults, horst-and-graben structures, and a reduction of both crustal and mantle velocities. These slow velocities are interpreted in terms of extensional bending-related faulting leading to fracturing and hydration in the upper part of the oceanic lithosphere. The incoming Mocha FZ coincides with an area of even slower velocities and thinning of the oceanic crust (10-15 % thinning), suggesting that the incoming fracture zone may enhance the flux of chemically-bound water into the subduction zone. Slow mantle velocities occur down to a maximum depth of 6-8 km into the upper mantle, where mantle temperatures are estimated to be 400-430°C.

## 4.1 Introduction

Subduction at convergent margins has a major impact on both the incoming plate, which is forced to subduct, and the overriding block. As the incoming plate approaches the continent (or island arc), the lithosphere bends into the trench, producing a prominent bathymetric bulge, the outer rise. Depending on the age, rheology and stress state of the lithosphere, uplift may start several hundreds of kilometers from the trench axis. Plate bending, however, is strongest within 50 km of the trench, where bending stresses exceed the yield strength of the lithosphere, producing normal faulting [e.g., *Masson, 1991; Ranero et al., 2003; Grevenmeyer et al., 2005*] and earthquake activity [e.g., *Chappel and Forsyth, 1979; Tilmann et al., 2008*] seawards of the trench. Recent work suggested that bending-related faulting might be an evolutionary process, affecting structure and composition of the downgoing plate [*Ranero et al., 2003; Grevenmeyer et al., 2005; 2007*].

The southern central Chile margin hosted the rupture area of the great 1960 Chilean earthquake ( $M_w \sim 9.5$ ) [*Cifuentes, 1989; Barrientos and Ward, 1990*] and is characterized by a filled trench confined between two main oceanic features: the Juan Fernandez Ridge (JFR) and the Chile Rise (Figure 4.1). The southern central Chile margin was characterized by *Bangs and Cande [1997]* using structural constraints from multichannel seismic reflection data. Main features were a 15-20 km wide accretionary prism and a  $\sim 2$  km thick trench fill. The backstop underlying the continental slope and its velocity structure, however, were poorly resolved. *Krawczyk et al., [2006]* used seismic refraction and wide-angle reflection data from an amphibious experiment to yield structural constraints of the entire subduction zone system offshore of the southern Arauco peninsula at  $\sim 38^\circ$ S. Their final velocity-depth model concentrated on the nucleation area of the great 1960 earthquake more than 80 km landwards of the trench and hence put less emphasis on the marine forearc. To refine the crustal model of the accretionary complex, marine forearc and downgoing plate, we re-analysed a subset of the SPOC (Subduction Process Off Chile) data [*Krawczyk et al., 2006*] and extended the profile across the trench-outer rise seaward of the trench to study the impact of bending-related faulting on the structure of the incoming plate. We integrated multi-channel seismic reflection (MCS) data and seismic refraction and wide-angle reflection data into our inversion and performed a joint refraction and reflection travel-time tomography to obtain a detailed velocity model of the marine forearc and the incoming/subducting oceanic lithosphere off Arauco peninsula, south central Chile ( $\sim 38^\circ$ S).

One of the aim of this study is to investigate the evolution of the seismic structure of the incoming/subducting oceanic plate. Prior to subduction the oceanic lithosphere suffers from plate bending, causing normal faulting [e.g., *Masson, 1991; Ranero et al.,*

2003] and earthquake activity ranging from micro-earthquakes of  $M_w < 1$  [Tillmann *et al.*, 2008] to large intraplate earthquakes of  $M_w > 6.5$  [e.g., Chappel and Forsyth, 1979; Lefeldt and Grevenmeyer, 2008]. Bending-related faulting modifies the porosity structure and hydro-geology of the oceanic lithosphere and thus affects the subduction water cycle [Ranero *et al.*, 2003; Grevenmeyer *et al.*, 2007]. A number of seismic experiments provided evidence that plate bending affects the subducting Nazca plate off northern [Ranero and Sallares., 2004], central [Kopp *et al.*, 2004; Grevenmeyer *et al.*, 2005], and southern central Chile [Contreras-Reyes *et al.*, 2007; 2008a]. At the trench-outer rise area, the oceanic crust is pervasively fractured and hydrated by extensional bending-related faults, allowing the percolation of fluids to mantle depths and thus resulting in the weakening of the oceanic lithosphere prior to subduction [Ranero *et al.*, 2003]. During subduction, large intraplate earthquakes associated with normal-faulting under the inner trench slope region suggest that plate bending and faulting continues until the plate un-bends at greater depth [Mikumo *et al.*, 2002; Vallee *et al.*, 2003]. Thus, oceanic lithosphere already hydrated and weakened at the outer-rise is further fractured and faulted by extensional stresses underneath the overriding plate. Ranero *et al.*, [2003], and Ranero and Sallares, [2004] have suggested that the isotherm of  $600^\circ\text{C}$  (the depth limit of the brittle lithosphere) corresponds to a good proxy for the maximum depth of mantle hydration. However, this depth as a limit for lithospheric hydro-alteration has not yet been constrained by active seismic studies. In this paper, we present new geophysical evidence for the evolution of the seismic structure of the oceanic Nazca plate prior to and during subduction, and we assess the maximum depth of mantle alteration using wide-angle data.

## 4.2 Geodynamic setting

The geological structure of the southern central Chile margin is controlled by the subduction of the oceanic Nazca plate beneath South America (Figure 4.1). The incoming Nazca plate subducts at  $\sim 6.6$  cm/yr with an azimuth of about  $\text{N}78^\circ\text{W}$  [Angermann *et al.*, 1999]. The Chilean subduction zone is composed of two major segments defined by the incoming oceanic plate formed at two different spreading centers: north of the Valdivia Fracture Zone (FZ) the oceanic lithosphere was formed at the Pacific-Farallon spreading center more than 20 Ma ago [Mueller *et al.*, 1997], whereas south of the Valdivia FZ it was created at the Chile Rise within the past 20 Ma [Herron, 1981] (Figure 4.1). North of the Valdivia FZ, the seafloor spreading fabric of the Nazca plate strikes approximately  $45^\circ$  to the trench axis, whereas south of the Valdivia FZ it strikes  $\sim 15^\circ$  to the trench axis. The Chile trench, Mocha and Valdivia Fracture Zones (FZs) define a triangle called the Mocha block, which is an area of high stress concentration on the plate interface that acts as a boundary between two major segments of the Chilean subduction zone [Barrientos

and Ward, 1990]. The main shock of the 1960 Chile earthquake ( $M_w \sim 9.5$ ), the largest ever instrumentally recorded, nucleated near the Mocha FZ and propagated southward for more than 900 km [Cifuentes, 1989; Barrientos and Ward, 1990].

Our study area is located offshore southern Arauco peninsula, where the Mocha FZ trending N55°E, is currently entering the trench at  $\sim 38^\circ$ S (Figure 4.2) and may be partly responsible for the uplift of the peninsula [Kaizuka, 1973]. Because Mocha FZ strikes obliquely to the trench axis, the fracture zone intersection with the trench migrated southward at  $\sim 3.1$  cm/yr over the past million years relative to South America. North of the Mocha FZ, the plate age at the trench axis is  $\sim 30$  Ma, whereas south of it the seafloor is about 24 Ma [Tebbens *et al.*, 1997]. The southern central Chile trench is filled by terrigenous sediments sourced from the Andes [Thornburg and Kulm, 1987]. The deposited material is transported through submarine canyons and redistributed within the trench from south to north [Thornburg *et al.*, 1990; Voelker *et al.*, 2006].

The primary geologic units exposed on land along the southern Chile coast are the continental basement rocks that are part of a Paleozoic accretionary complex and magmatic arc [Mordojovich, 1974; Herve *et al.*, 1988]. Exploratory drilling into the Arauco basin (see Figure 4.2 for location) reached metamorphic basement beneath  $\sim 500$  m of Pliocene shelf sediments [Mordojovich, 1974]. Interpretation of seismic reflection data across the Arauco basin indicates that the oldest sediments in the depocenter of the forearc basin are Senonian [Gonzalez, 1989].

### 4.3 Seismic reflection and bathymetric data

Seismic reflection and swath bathymetric data were acquired offshore Arauco peninsula during the SPOC and TIPTEQ projects using R/V SONNE in 2000/2001 and 2004/2005, respectively [Reichert *et al.*, 2002; Krawczyk and SPOC Team, 2003; Flueh and Greve-meyer, 2005; Scherwath *et al.*, 2006]. The seismic signals for the seismic reflection experiment were generated by a tuned set of 20 airguns with a total volume of 51.2 litres. The multi-channel seismic reflection data were analysed using standard processing, including re-binning, normal-move out correction, stacking, deconvolution, and post-stack time migration. A predictive deconvolution with two gates, for the shallow sedimentary events and the deeper crustal events, was applied before the stack. A space and time variant frequency filter prior to a post-stack migration completed the processing flow [Reichert *et al.*, 2002]. Seismic reflection data are displayed in Figure 4.3.

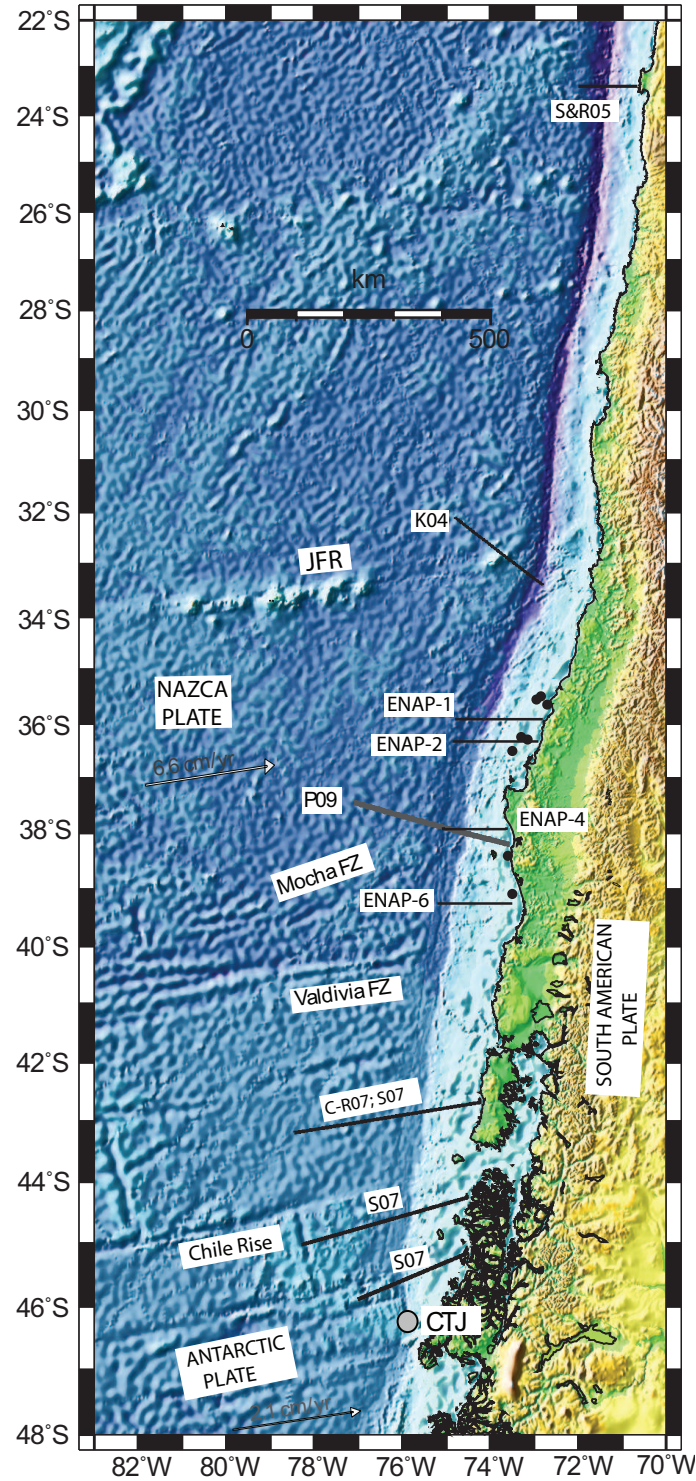


Figure 4.1: Geodynamic setting of Nazca, Antarctic, and South America plates; plates join at the Chile Triple Junction (CTJ), where the Chile Rise is currently subducting at  $\sim 46.4^\circ$  S. The southern central Chilean margin is heavily sedimented and lies between the Juan Fernandez Ridge (JFR) and Chile Rise spreading center. P09 is the study profile (Figure 4.2). Small black dots indicate locations of the drilled wells [Mordohovic, 1974]. Seismic profiles ENAP 1, 2, 4 and 6 were studied by Bangs and Cande, [1997] and Diaz-Naveas, [1999], while black lines denote the published seismic profiles: S&R05 Sallares and Ranero., 2005]; K04 [Kopp et al., 2004]; C-R07 [Contreras-Reyes et al., 2007] and S07 [Scherwath et al., 2007].

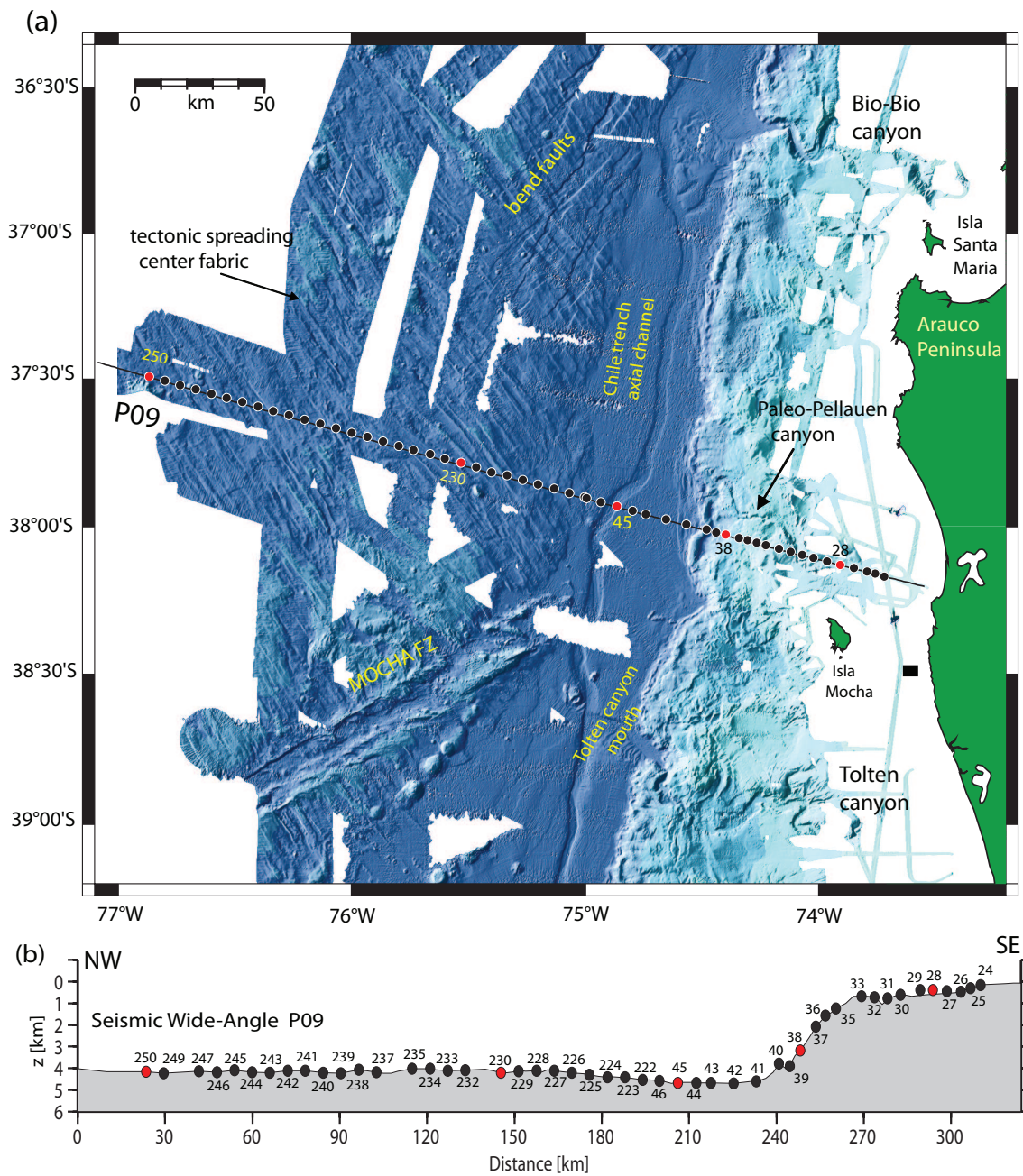


Figure 4.2: (a) High-resolution bathymetric image of the seafloor off Arauco peninsula. Solid black lines are the integrated TIPTEQ and SPOC reflection and refraction profiles, while red dots and station numbers indicate the five stations (250, 230, 38, 45 and 28) shown in Figures 4.4-4.6. Solid black square denotes the location of the well drilled by ENAP [Mordohovic, 1974]. (b) Seismic profile P09 and numbers of the 48 OBH/S stations used in the travel-time tomographic inversion.

### 4.3.1 The trench-outer rise area

Seaward from the trench axis ( $>70$  km) the oceanic plate is covered by a thin 0-400 m layer of pelagic sediments, which is draped by a much thinner and transparent blanket of hemipelagic mud. Here, high resolution multibeam bathymetric mapping shows the SE-NW-trending topographic pattern of the tectonic fabric formed at the spreading center, which is overprinted by horst-and-graben structures caused by bending-related faulting (Figure 4.2). Roughly 50 km off the trench axis, turbidites begin to fill the graben-like structure and overlay pelagic sediments, forming a sedimentary sequence with increasing thickness towards the trench (Figure 4.3). The trench-fill wedge is  $\sim 40$  km wide, with a maximum thickness of  $\sim 1900$  m of turbidites overlying a  $\sim 300$  m thick sequence of hemipelagic/pelagic sediments (Figure 4.3). Moho reflections occur at  $\sim 2.3$  s below the top of the oceanic basement and can clearly be identified in the seismic section (Figure 4.3a).

The Nazca plate carries seamount "chains" rising up to 2 km above the surrounding seafloor and elongated ridges aligned sub-parallel to the trend of the Mocha FZ (Figure 4.2). Approaching the trench, these edifices become progressively buried by sediments (Figure 4.2). The traverse ridge of the Mocha FZ is usually not higher than 700 m. At  $\sim 25$  km seaward of the deformation front, a 5 km wide trench axial channel cuts into the seabed. The axial channel is buried by turbiditic deposits, and coincides with a horst-and-graben fault (Figure 4.3b). Towards the trench, bending-related faults tend to continue and cut often through the entire trench fill (Figure 4.3). In addition, the top of the oceanic crust becomes rougher in the trench-outer rise area, which might be caused by the combined effect of bending-related faulting and the rough relief of the Mocha FZ, which intersects the seismic line in the vicinity of the trench axis (Figure 4.2).

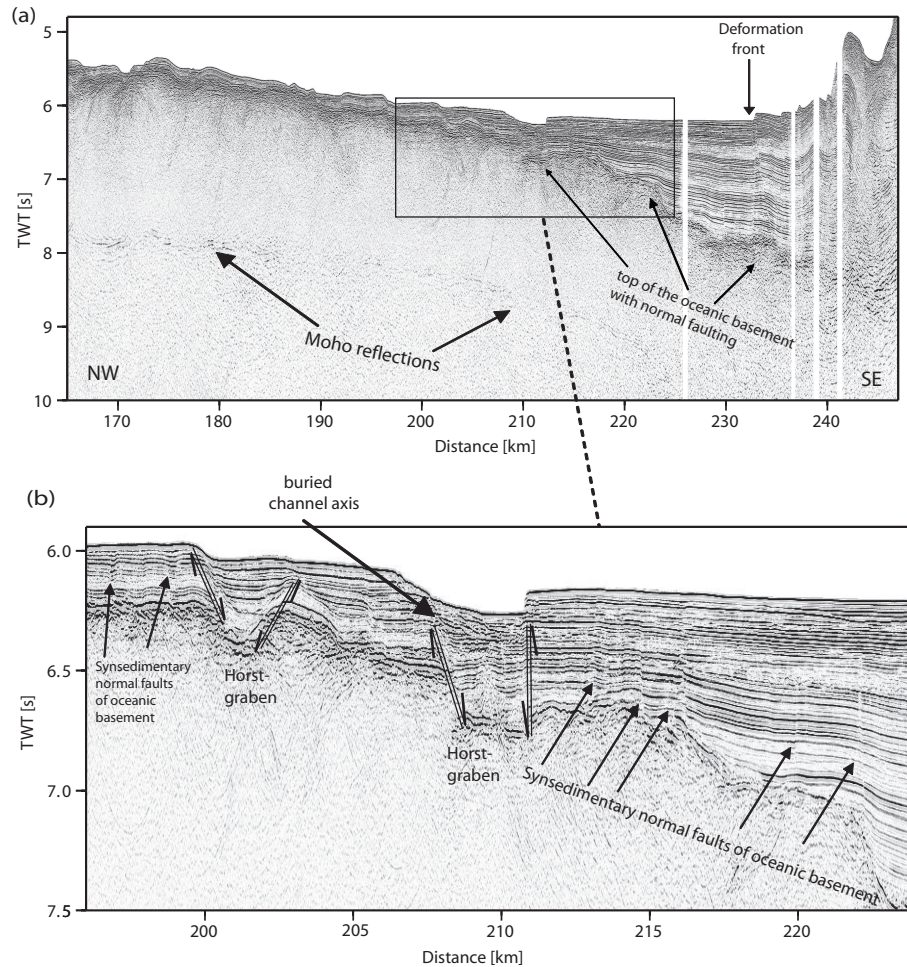


Figure 4.3: (a) Post-stack time migration of the trench-outer rise and deformation front areas of seismic profile P09. (b) The seaward limit of the smooth trench is marked by the notably rough topography of the igneous basement. Its surface displays a characteristic, linear, topographic pattern caused by crustal horst-and-graben structures, masked by a thin sediment cover. The outer trench slope is disrupted by a set of subparallel normal faults that cut the oceanic crust.

#### 4.4 Wide-angle seismic data

Figure 4.2 shows the location of the seismic refraction/wide-angle reflection profile analysed to study the incoming plate and marine forearc at  $\sim 38^\circ S$ . The westernmost part of the line was obtained during the TIPTEQ cruise SO181 aboard R/V Sonne in 2005. 25 seismic stations were placed along the  $\sim 215$  km long profile P09 [Flueh and Grevemeyer, 2005; Scherwath et al., 2006]. This line extended SPOC profile P01 shot during SO161 in 2001 [Krawczyk and SPOC Team, 2003] further seaward across the trench-outer rise. Shots were recorded with a total number of 48 OBS (Ocean Bottom Seismometers) [Bialas and Flueh, 1999] and OBH (Ocean Bottom Hydrophones) [Flueh and Bialas, 1996], covering a distance of  $\sim 250$  km along the easternmost portion of the incoming oceanic Nazca



plate, and  $\sim 75$  km along the westernmost portion of the continental margin (Figure 4.2). The seismic source for the refraction work carried out during TIPTEQ was a cluster of 8x8-liter G-guns, providing a total volume of 64 litres for each shot. During SPOC a tuned array of 20 airguns provided a total volume of 51.2 litres. Both sources were fired at a time interval of 60 s, which corresponds to an average shot spacing of  $\sim 150$  m. The record sections were interpreted after bandpass filtering (1 to 20 Hz) and predictive deconvolution. The signal-to-noise ratio obtained for most of the stations was high (Figures 4.4-4.6).

We have recorded crustal refractions ( $P_g$ ), Moho wide-angle reflections ( $P_mP$ ), upper mantle refractions ( $P_n$ ), refractions through trench-sediment ( $P_s$ ), and reflections from the top of the oceanic crust ( $P_{toc}P$ ) with excellent quality. Five examples of seismic record sections are shown in Figures 4.4-4.6, with their respective seismic phases identified. Apparent velocities influenced by the trench-sediment and forearc structures decrease and increase landward, respectively.  $P_s$  and  $P_{toc}P$  phases occur at approximately km-200 and hence 40 km from the trench axis. Figure 4.5d shows an example of record section OBH 38 positioned on the continental slope (see Figure 4.2 for location). The OBH data provide coverage of trench fill and accreted sediments down to basement at the NW and SE branch, respectively. Mantle, oceanic and continental crustal phases were recorded on most of the stations with excellent quality (Figures 4.5c, 4.5d, and 4.6e). Two striking features of the dataset are: the rapid increase of apparent  $P_g$  velocities from profile-km  $\sim 310$ , and the long offsets of  $P_n$  phases ( $>100$  km) of some stations located on the continental shelf (Figure 4.6e).

Picking of the seismic phases was done manually, and picking errors were assumed to be half a period of one arrival, to account for a possible systematic shift in the arrival identification, and were weighted according to the phase quality. Detailed information regarding average picking uncertainties and number of picks for the study profile are summarized in Table 4.1.

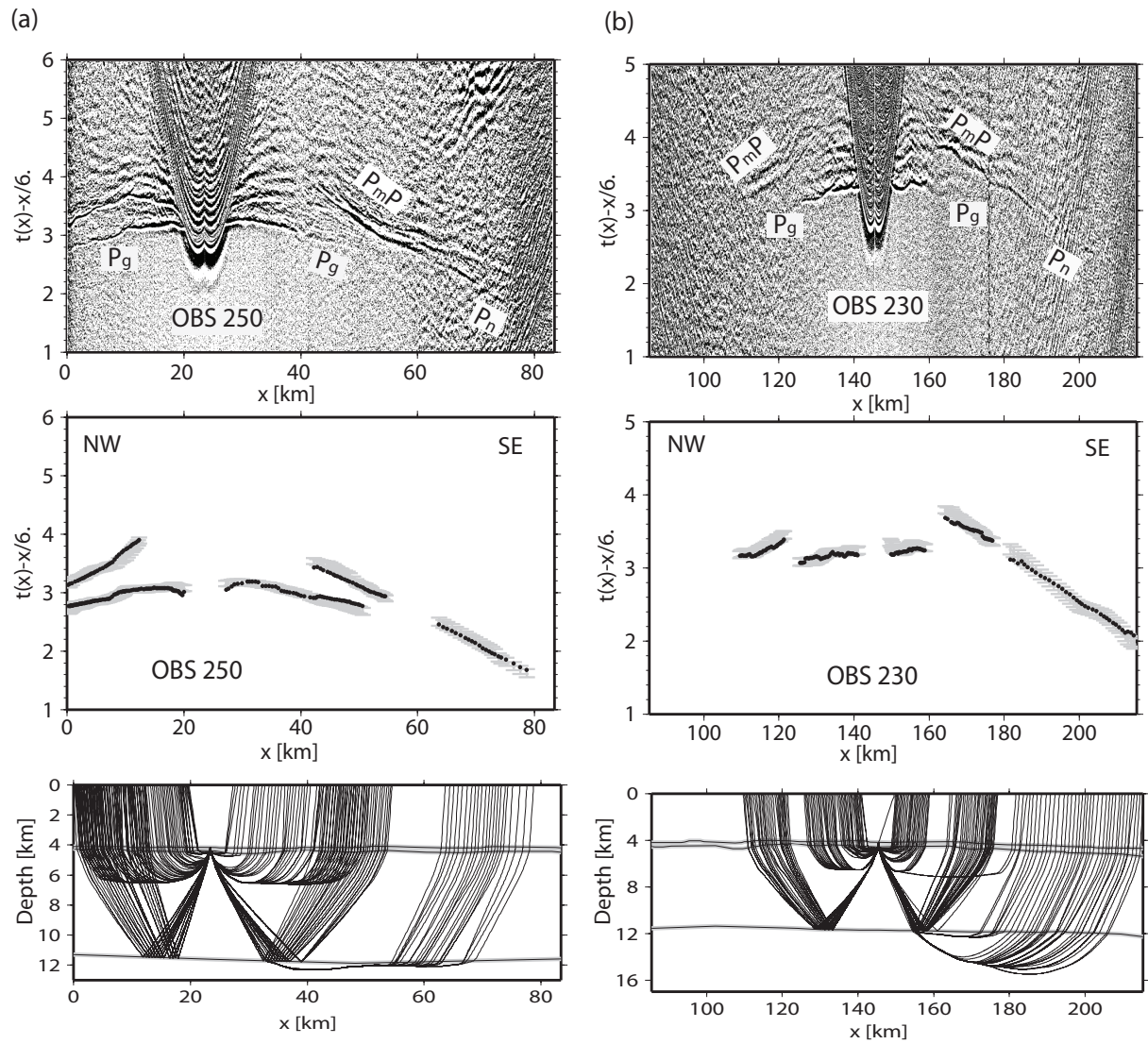


Figure 4.4: Examples of wide-angle seismic data with predicted travel times (white circles), which are computed based on the velocity model presented in Figure 4.7b. (a) OBS 250 and (b) OBS 230.

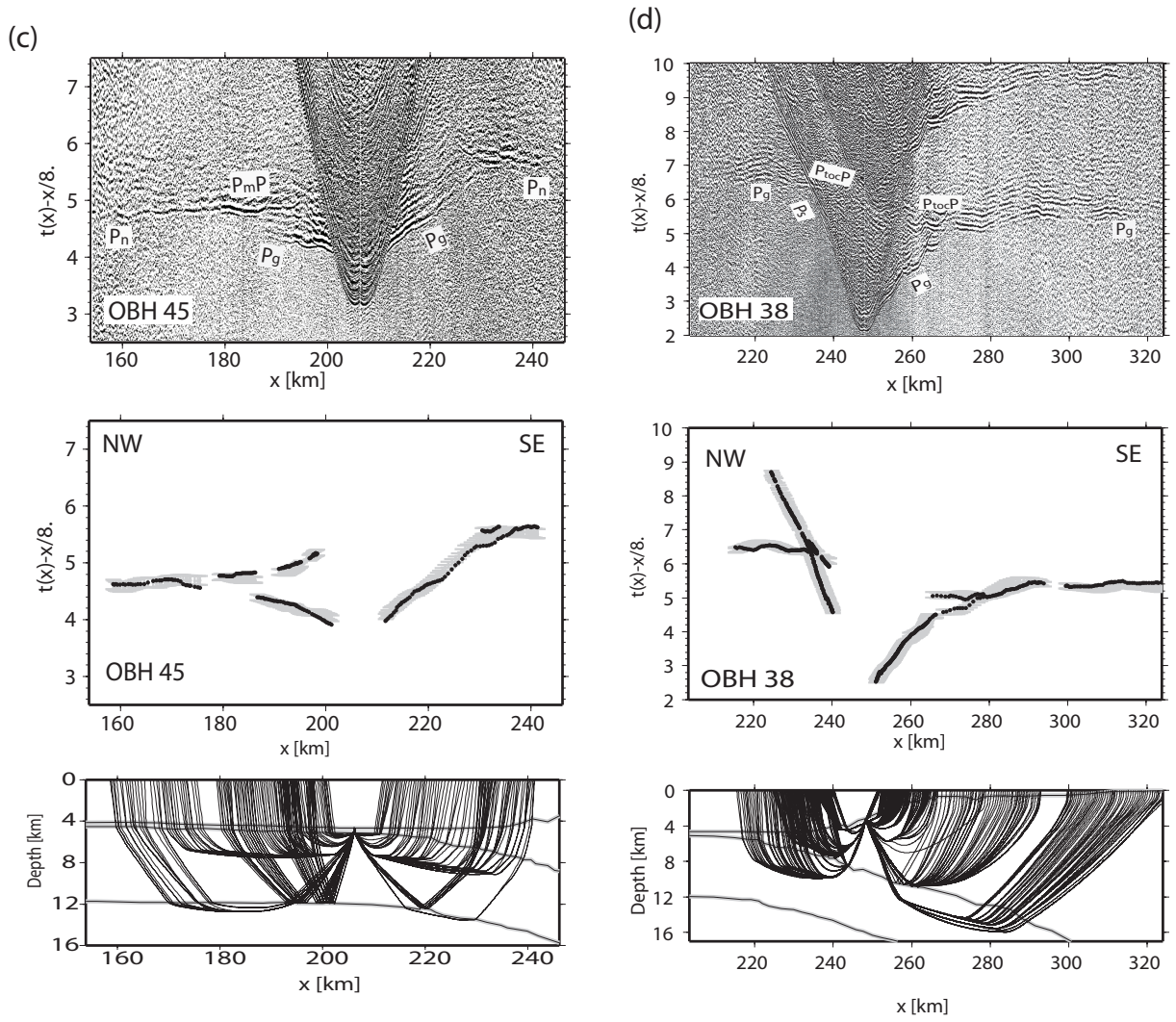


Figure 4.5: (continued) (c) OBH 45 and (d) OBH 38.

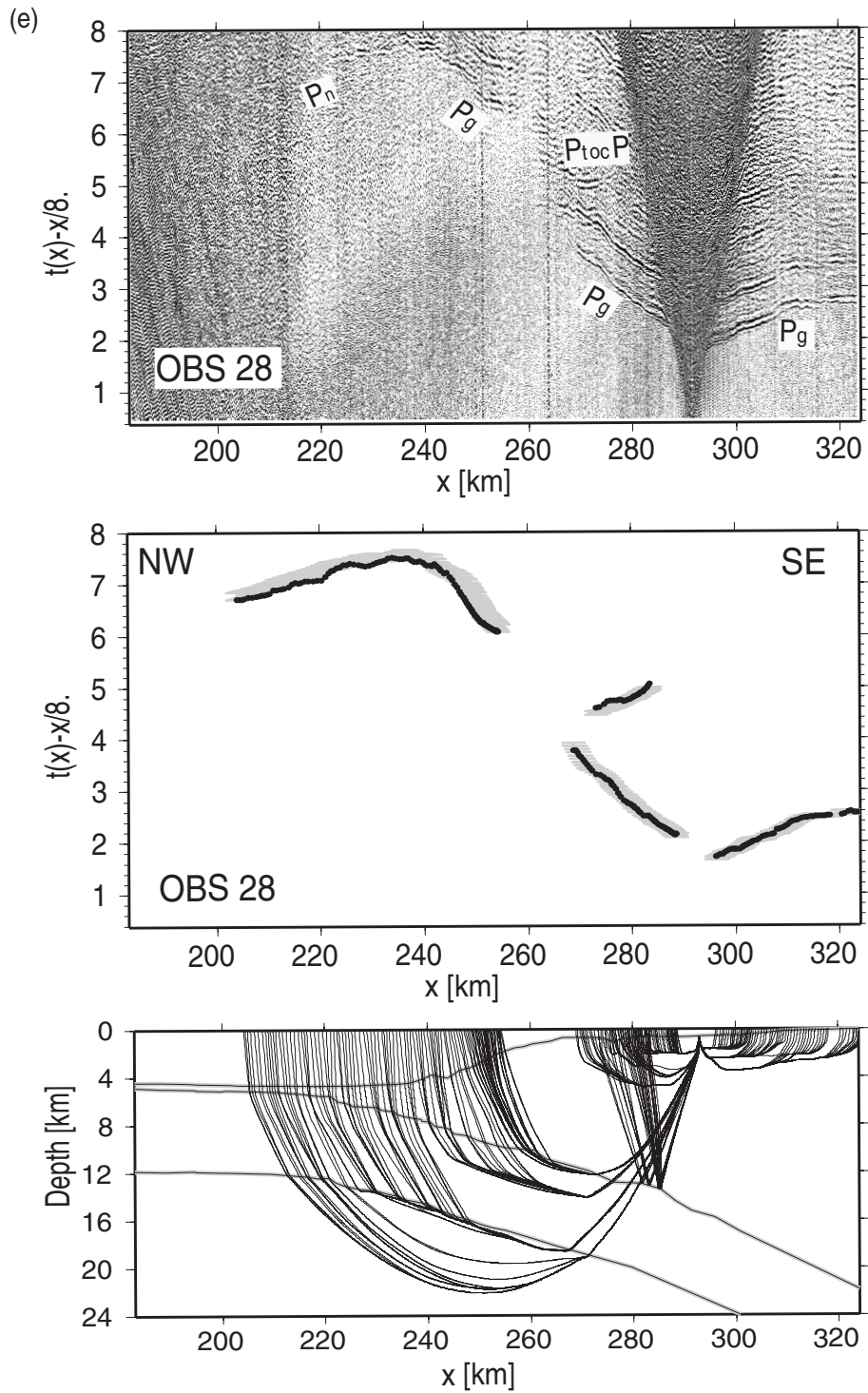


Figure 4.6: (continued) (e) OBS 28.

## 4.5 Travel-time tomography scheme

We obtained the P-wave velocity-depth structure using the joint refraction and reflection travel time inversion method of *Korenaga et al.*, [2000]. This method allows joint inversion of seismic refraction and reflection travel time data for a 2-D velocity field. Travel times and ray paths are calculated using a hybrid ray-tracing scheme based on the graph method and the local ray-bending refinement [*van Avendonk et al.*, 1998]. Smoothing constraints using predefined correlation lengths and optimized damping constraints for the model parameters are employed to regularize an iterative linearized inversion [*Korenaga et al.*, 2000].

The velocity model consists of the following geological units, (1) water, (2) sediments, (3) marine forearc basement, (4) oceanic crust and (5) upper oceanic mantle. To derive the velocity depth model, the water depth was taken from the known bathymetry, which remained fixed during the inversion. Thickness of the sediment unit overlying the oceanic plate seaward of the trench wedge was obtained by picking and converting the vertical incidence reflections from the time migrated MCS data, using a constant velocity of 1.7 km/s. In order to obtain the velocity of the sediments and the thickness of the sedimentary forearc basin, a combined approach using sedimentary refractions through the basin and reflections from the top of the oceanic basement plus TWT reflection data was applied. Landward of roughly km-200, refracted  $P_s$  and  $P_g$  and reflected  $P_{toc}P$  phases were used to directly invert for the velocity structure of the marine forearc and geometry of the top of the oceanic plate. Inverted velocities and the depth of the plate boundary (igneous oceanic basement) were then held fixed in the following iterative inversions. The inner oceanic crust structure was inverted using  $P_g$  phases (first and later arrivals) to their maximum offset and  $P_mP$  phases in order to derive the velocity field and Moho depth. Similarly, the crustal velocities and Moho depth remained fixed for the next step of the inversion, where the upper mantle velocities were derived using oceanic  $P_n$  phases.

The applied hybrid scheme uses both first and second arrivals to constrain the velocity model, without the need to disregard for example secondary arrivals such as lower crustal  $P_g$  phases, which become secondary arrivals where  $P_n$  arrivals overtake  $P_g$ . However, one problem of this approach is the identification and separation of crustal refractions  $P_g$  traveling through the continental and oceanic crust. This fact is critical in the landward portion of the model, where the small velocity-contrast at the plate boundary makes it difficult to separate oceanic and continental  $P_g$  arrivals (Figure 4.5d). To solve this problem, we used for the upper plate inversion only  $P_g$  phases with offset up to 40 km ( $P_{g1}$ ). For the lower plate and subsequent inversions, we decreased damping weight values

in this area of the velocity-depth model and inverted  $P_g$  arrivals up to their maximum offsets ( $P_{g2}$ ). Thus, arrivals at greater offset might constrain the upper structures. Several tests have shown that this approach fails at velocity discontinuities of high velocity contrast (for example Moho) but works adequately in continuous velocity-boundary (landward part of the plate boundary). This is due to the fact that the tomographic inversion tends to smooth the lowermost and uppermost part of the upper and lower layer, respectively. As we described above, we use 2D velocity damping functions with either large or low weighting factors depending on the zone to retain or invert [Korenaga *et al.*, 2000].

#### 4.5.1 Reference model and inversion parameters

The 2-D velocity model is  $\sim 324$  km long and 30 km deep. We used two floating reflectors to model (1) the interplate boundary beneath the continental margin and (2) the oceanic Moho. The initial geometry of the interplate boundary reflector was obtained by forward modelling of the  $P_g$ ,  $P_s$  and  $P_{toc}P$  phases landward of profile-km 200 profile. Unfortunately,  $P_{toc}P$  reflections landward of km-280 are weak and modelling of the reflector is difficult. We have therefore continued the geometry of the plate boundary towards the land by fitting it to hypocenter data of a temporary network in the Arauco peninsula which imaged the plate contact [Haberland *et al.*, 2006]. We prepared the reference model for the tomographic inversion by 1D-modeling of four OBH/S stations, which we consider as a key to define the general structure of the margin [Vera, *personal communication*, 2007]. Figure 4.7a shows the locations of the four selected stations and their respective 1-D models. The 2-D seismic velocities of the reference model are calculated by linearly interpolating the velocities of the four 1-D velocity models. A similar approach is presented by Sallares and Ranero [2005].

The root mean square travel time residuals ( $T_{RMS}$ ) obtained with the 2-D reference model are presented in Table 4.1. The horizontal grid spacing of the model used for the velocity inversion is 0.5 km, whereas the vertical grid spacing is varied from 0.1 km at the top of the model to 1 km at the bottom. Depth nodes defining the plate boundary and Moho reflectors are spaced at 1 and 2 km, respectively. We used horizontal correlation lengths ranging from 2 km at the top to 10 km at the bottom of the model, and vertical correlation lengths varying from 0.1 km at the top to 2.5 km at the bottom. Different tests showed that varying the values of correlations lengths by 50% does not significantly affect the solution. Because the trade-off between correlation lengths and smoothing weights, we tried to use shorter correlation lengths and larger smoothing weights in order to reduce memory requirements [Korenaga *et al.*, 2000]. Depth and velocity nodes are equally weighted in the refraction and reflection travel time inversions.

### 4.5.2 Final and uncertainty velocity models

Tests with several starting models converge to nearly the same final model. In order to study the accuracy of the final model, we employed the Monte Carlo method [Korenaga *et al.*, 2000]. The uncertainty of a nonlinear inversion can be expressed in terms of the posterior model covariance matrix [e.g., Tarantola, 1987], which can be approximated by the standard deviation of a large number of Monte Carlo realizations assuming that all the realizations have the same probability [e.g., Tarantola, 1987]. The uncertainty estimated by this method should be interpreted as the uncertainty for our model parameters (*i.e.*, starting velocity model and smoothing constraints). The procedure to estimate velocity-depth uncertainties consisted of randomly perturbing velocities and reflector-depths of our reference model (Figure 4.7a). We generated 100 random initial velocity models by adding randomly distributed smooth perturbations. The 2-D starting velocity models were obtained by linearly interpolating 1-D velocity profiles shown in Figure 4.7a, where gray areas represent possible variations in velocity randomization. The initial geometry of the interplate and Moho reflectors were randomly varied within a range of  $\pm 1.5$  and  $\pm 2$  km, respectively. In addition to the perturbed reference models we produced 100 so-called noisy arrival time sets constructed by adding random phase errors ( $\pm 50$  ms) and common receiver errors ( $\pm 50$  ms) to the original data set [Korenaga *et al.*, 2000]. Then we performed a tomographic inversion for each velocity model with one noisy data set, in order to estimate not only the dependence of the solution on the reference model but also the effect of phase arrival time picking errors. The mean deviation of all realizations of such an ensemble is considered to be a statistical measure of the model parameter uncertainties [e.g., Tarantola, 1987]. The stopping criterion for each inversion was  $\chi^2 \sim 1$ . Figure 4.7b shows the average velocity-depth model from the 100 final models, and detailed information regarding root-mean-square travel time misfits  $T_{RMS}$  and  $\chi^2$  parameters for the final average model is summarized in Table 1.

The standard deviation of the calculated velocities ( $\sigma_v$ ) is well constrained in the seaward portion of the velocity-model (Figure 4.8). Landward from profile-km 260,  $\sigma_v$  values in the upper plate increase to larger than 0.15 km/s due to the reduced data coverage (Figure 4.8a). Below the upper plate and within the upper oceanic crust,  $\sigma_v$  values increase up to 0.5 km/s, which indicates that velocities in this part of the model are largely unconstrained. The depth uncertainties of the interplate reflector oceanward from km $\sim$ 255 are lower than 0.1 km and reach 0.4 km at the landward edge of the velocity-depth model (Figure 4.8b), which is a zone characterized by the absence of  $P_{toc}P$  reflections. Moho depth uncertainties oceanward of km $\sim$ 270 range between 0.1 km and 0.3 km, and reach values higher than 0.5 km at the south eastern edge of the velocity model (Figure 4.8d).

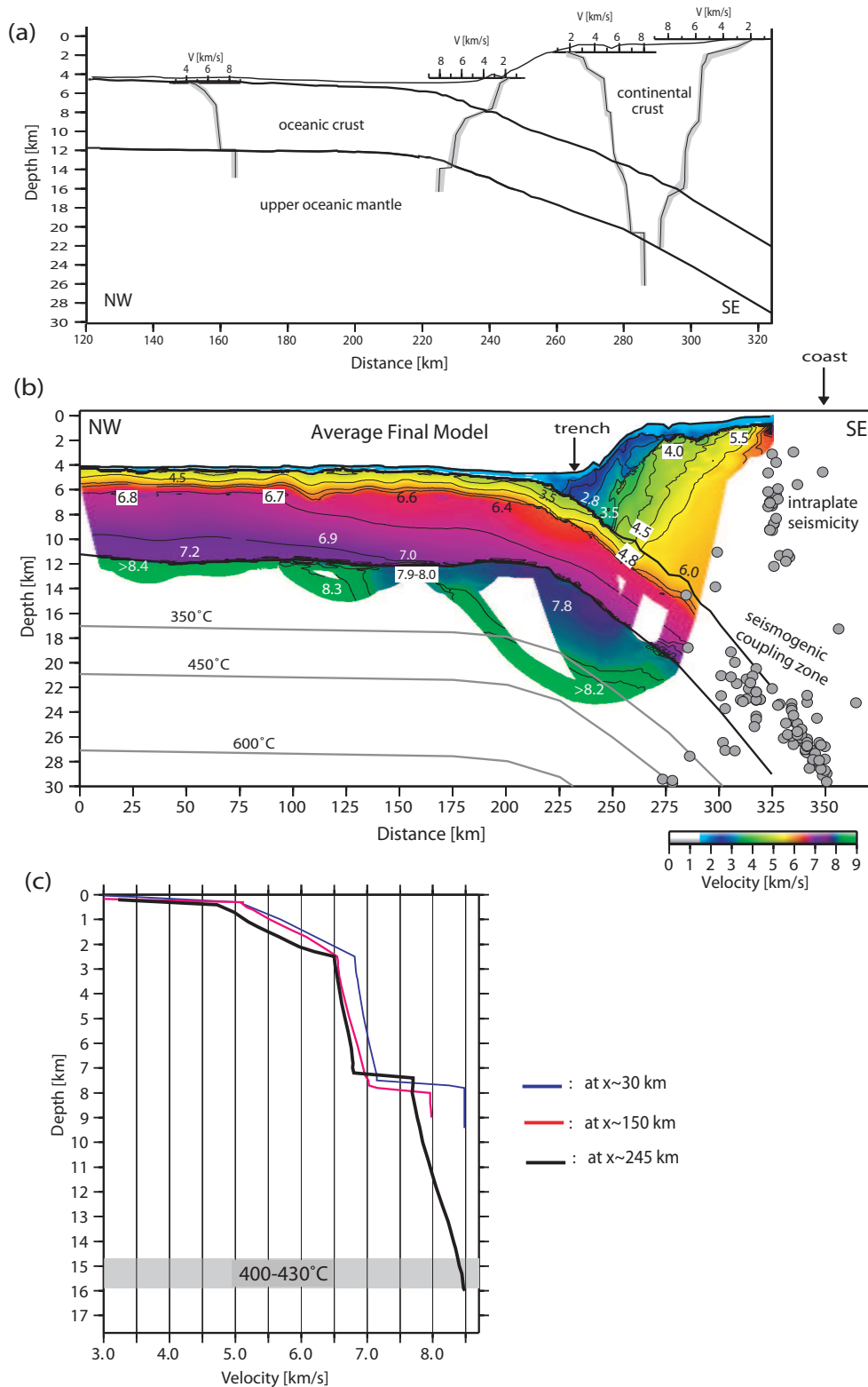


Figure 4.7: (a) One-dimensional reference models. (b) Final velocity-depth model derived by averaging all Monte Carlo ensembles, displayed together with projected earthquakes. The onset of shallow and coastal seismicity coincide roughly with the location of the most landward velocity transition zone inferred by our tomographic model. Hypocenters are taken from the TIPTEQ temporary seismological network [Haberland et al., 2006]. Isotherm computations are based on the cooling of a semi-infinite half-space model [e.g., Turcotte and Schubert., 1982]. (c) 1D-Velocity depth profiles are extracted from (b) below sediments in order to compare the seismic structure of the "normal" (blue), altered incoming (red) and altered subducting oceanic lithosphere (black).



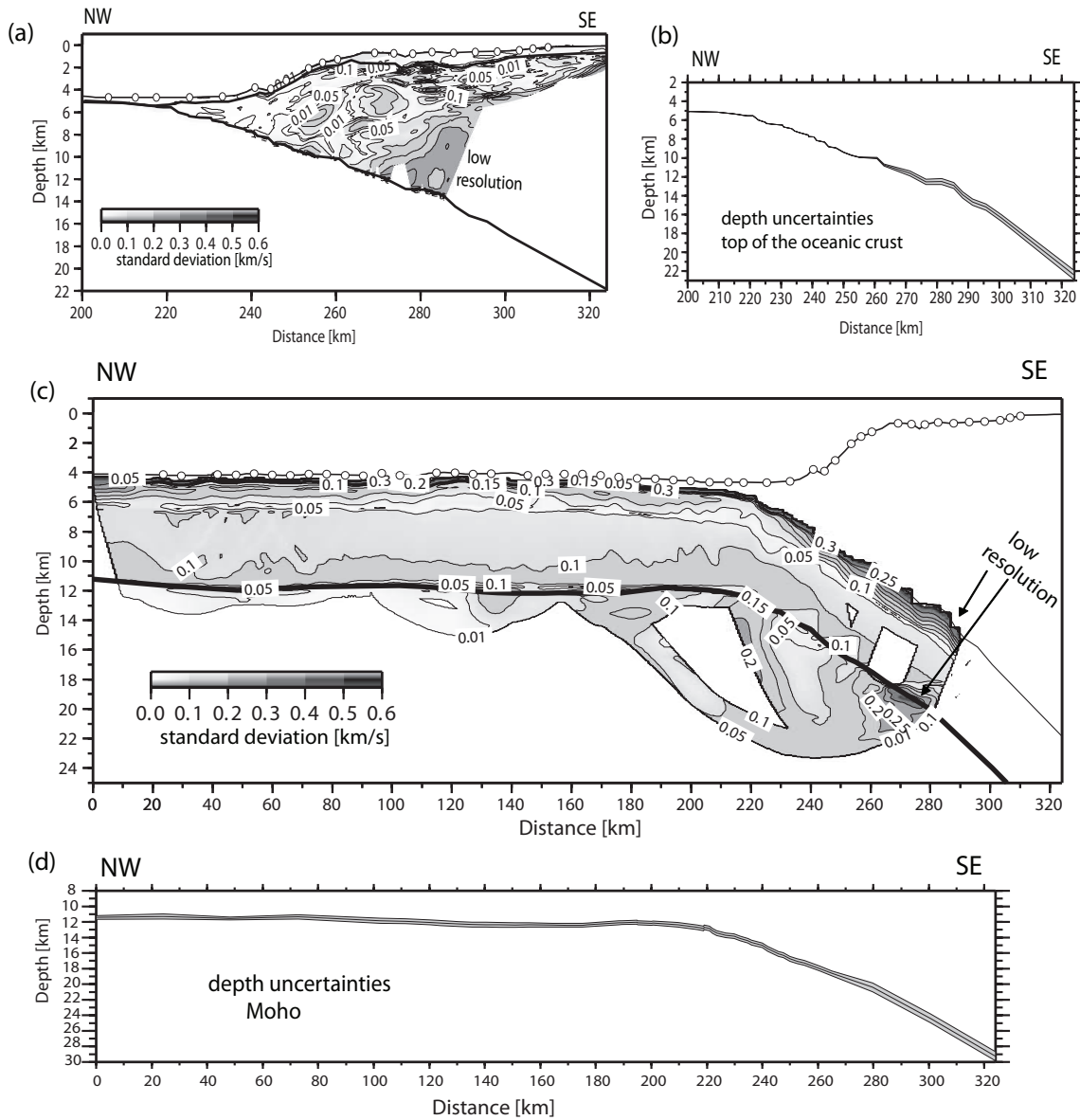


Figure 4.8: Velocity uncertainties for the (a) upper and (c) lower plates, and depth uncertainties for the (b) interplate and (d) Moho reflectors are shown.

Table 4.1: Summary of travel-time picks, and details of seismic P-wave velocity-depth inversion based on the average final models shown in Figure 4.7b.  $P_{g1}$ : continental crustal refraction or crustal refractions with offsets  $<40$  km;  $P_s$ : trench fill refractions;  $P_{toc}P$ : reflection from the top of the oceanic crust;  $P_{g2}$ : oceanic crustal refraction or crustal refractions with offsets  $>40$  km;  $P_mP$ : Moho reflections;  $P_n$ : oceanic mantle refractions.

$T_{RMS}$  (ms): root-mean-square travel time misfit,  $\Delta T_{avg}$ : average travel time uncertainty and  $\chi^2$ : chi-square parameter, are given.

Phase	$\Delta T_{avg}$ (ms)	Initial Model $T_{RMS}$ (ms)	Reference Model $\chi^2$	Average Final Model $T_{RMS}(ms)$	Average Final Model $\chi^2$
$P_{g1}+P_s$	55	222.36	15.5	52.79	0.85
$P_{toc}P$	70	198.70	9.52	75.00	1.24
$P_{g2}$	60	68.32	1.12	54.45	0.68
$P_mP$	75	99.70	2.02	76.91	1.20
$P_n$	75	135.75	3.93	75.54	1.17

### 4.5.3 Resolution test

To check the resolvability of the obtained velocity model we have created a synthetic model consisting of sinusoidal anomalies located both in the upper plate and the oceanic crust (Figures 4.9a and 4.9c). The anomalies are superimposed onto the final average velocity model shown in Figure 4.7b. The maximum amplitude of each anomaly is  $\pm 8\%$  for the upper plate and  $\pm 6\%$  for the oceanic crust (Figure 4.8). Synthetic travel time data with the same source-receiver geometry as in the real data set have been generated with the perturbed model, and they were inverted using an initial unperturbed model to see how well given perturbations are recovered. The recovery models are plotted in Figures 4.9b and 4.9d, which were gained after 5 and 3 iterations, respectively. The results show that most of the anomalies are reasonably well reproduced in position, shape and amplitude, except for two regions: (1) at the bottom of the upper plate at  $\text{km}\sim 285$ , and (2) in the upper oceanic crust at  $\text{km}\sim 250$  (Figures 4.9b and 4.9d). These regions have low ray coverage and are poorly constrained, as is shown by the velocity uncertainty model (Figure 4.8). The recovered velocity anomalies in the upper part of the overriding plate, trench fill and oceanic crust seaward from  $\text{km}\sim 220$  show certain shape deterioration (Figure 4.8). Nevertheless, the results indicate that the geometry and instrument spacing yields a sufficiently high resolution for these structural anomalies, discerning between positive and negative variations along the overriding plate and oceanic crust.

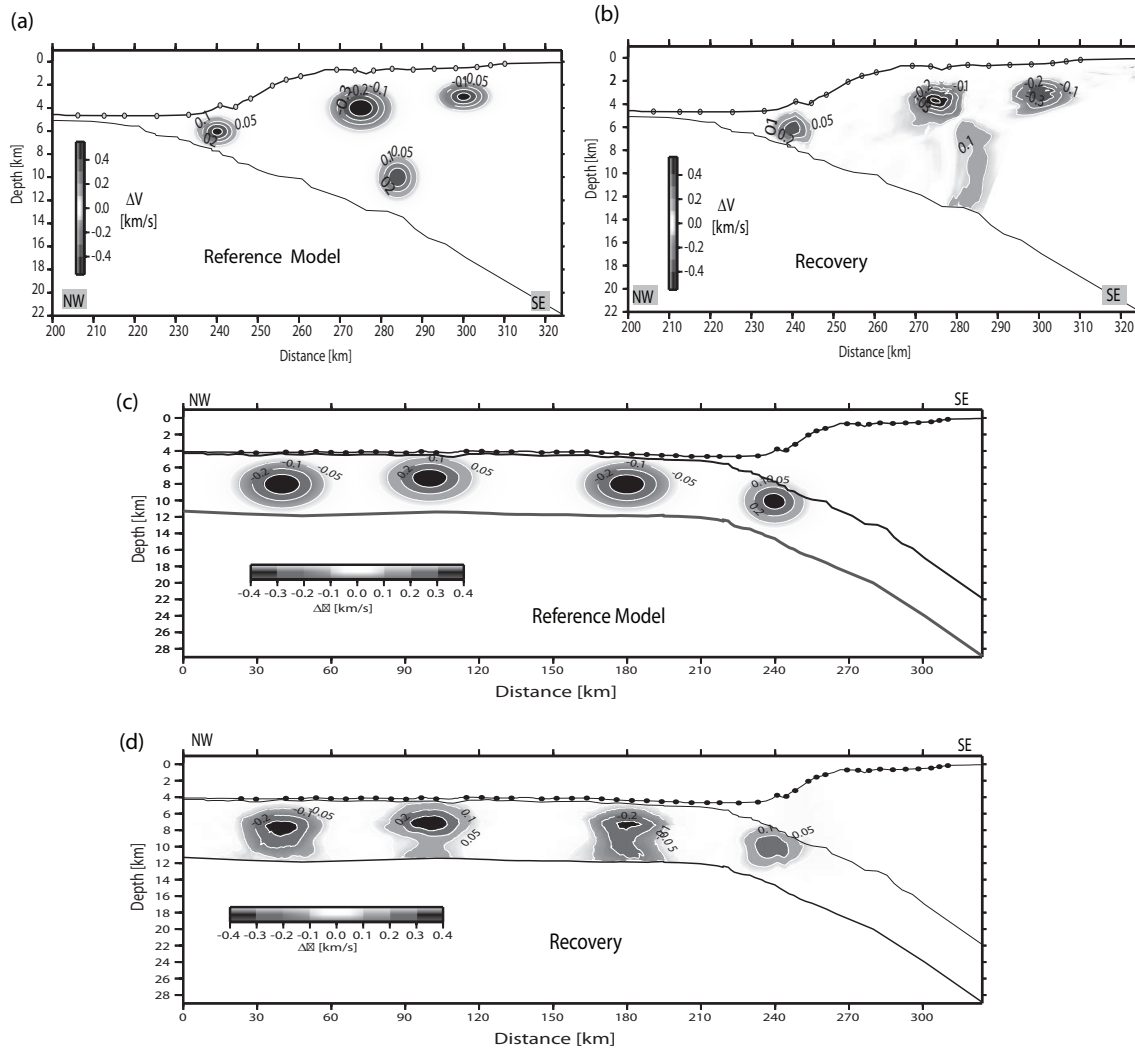


Figure 4.9: Results of resolution test. (a) and (c) Synthetic reference velocity models, consisting of four single sinusoidal anomalies superimposed onto the final velocity model of Figure 4.7b. (b) and (d) Recovery obtained after five and three iterations, respectively.

## 4.6 Results and Discussion

### 4.6.1 Alteration of the oceanic crust

In the seaward section of the tomographic model, the velocity structure of the oceanic crust provides uppermost and lowermost crustal velocities of  $\sim 4.4$  and  $\sim 7.2$  km/s, respectively. These velocities are typical for mature oceanic crust sufficiently far way from the ridge crests so that strong hydrothermal circulation has largely ceased [Grevenmeyer *et al.*, 1999; Grevenmeyer and Weigel, 1996]. The "typical" lower crustal velocities seaward of the trench-outer rise area are consistent with a undeformed and dry oceanic crust [Carlson, 1998; Contreras-Reyes *et al.*, 2007], which reflect an unaltered state of the crust away from

the influence of tectonic extensional stresses in the outer rise region.

Approaching the trench, however, velocities for the igneous crust begin to decrease 100-120 km seaward from the deformation front at crustal and uppermost mantle depths (Figure 4.7c). The uppermost crustal velocities decrease to values lower than 3.5 km/s, which are much less than typical uppermost velocities of layer 2 of mature oceanic crust ( $>4.5$  km/s) [e.g., *Grevenmeyer and Weigel*, 1996]. Low crustal velocities ( $< 7$  km/s) in the trench-outer rise area suggest a significant alteration of the porosity structure of the entire oceanic crust. The decrease of velocities is accompanied by an increase in the degree of fracturing (Figure 4.3), and probably coincides with activation of new cracks and normal extensional faults induced by bending-related faulting [*Ranero and Sallares*, 2004]. A similar trend in velocity reduction in the trench-outer rise area has been observed offshore Antofagasta at  $\sim 23.5^\circ$ S [*Ranero and Sallares*, 2004], and offshore Isla de Chiloe at  $\sim 43^\circ$ S [*Contreras-Reyes et al.*, 2007].

#### 4.6.2 Alteration of the oceanic mantle prior to subduction

Seaward of the trench, mantle velocities faster than 8.4 km/s are interpreted to be features of dry mantle peridotite [*Christensen*, 1996], indicating that the oceanic Nazca plate approaches the subduction zone with an undeformed and dry mantle. Closer to the trench, however, mantle velocities decrease to minimum values of  $\sim 7.8$  km/s (Figure 4.7c), which is significantly lower than the velocity of mantle peridotite ( $>8.1$  km/s). The velocity reduction suggests fracturing and/or hydration of the oceanic mantle in the trench-outer rise area. With an increasing degree of hydration and hence serpentinization the seismic compressional wave velocity is reduced from  $>8.1$ - $8.3$  km/s for pristine peridotite to  $\sim 4.5$  km/s at 100% transformation of peridotite to serpentinite [*Christensen*, 1996]. Perhaps, though, the "normal" uppermost mantle velocity  $>8.1$  km/s between  $\text{km}\sim 260$  and  $\text{km}\sim 280$  is not a real feature but rather an artifact of the seismic tomography due to the low resolution, as indicated by the uncertainty of the velocity model (Figure 4.8c).

Along seismic line ENAP-2 (Figure 4.1), *Diaz-Naveas* [1999] imaged bend-faults cutting through the crust/mantle boundary into uppermost mantle. Similarly, to the south along seismic transect ENAP-6, *Diaz-Naveas* [1999] and *Grevenmeyer et al.*, [2005] imaged outer rise bending-related faults cutting at least  $\sim 6$  km into the uppermost mantle. Offshore Isla de Chiloe (at  $\sim 43^\circ$ S), a similar trend of  $P_n$  velocity reduction and relative high Poisson's ratios were observed [*Contreras-Reyes et al.*, 2007; 2008a]. These observations give a clear sign of pervasive fracturing of the entire oceanic crust offshore south central Chile. Since water is required to alter mantle peridotite to serpentinite, pervasive fracturing of the entire crust is suggested for the lithosphere entering the subduction zone.

Similar features have also been observed in central America [Grevemeyer *et al.*, 2007; Ivandic *et al.*, 2008], suggesting that serpentinization occurring in the trench-outer rise might be a characteristic feature of subduction.

### 4.6.3 Hydro-alteration processes affecting the subducting oceanic lithosphere

Figure 4.7c summarized the evolution of the seismic structure of the oceanic lithosphere as it approaches to the subduction zone. The velocity structure within the uppermost 12 km of the mantle imaged below the continental slope (Figure 4.7c) is characterized by a single velocity gradient of  $0.1 \text{ s}^{-1}$ . "Normal" mantle velocities of  $\sim 8.4 \text{ km/s}$  are reached roughly 6-8 km below the Moho. One mechanism to cause a vertical velocity gradient is impact of overburden pressure conditions at greater depth. Christensen [1996] used laboratory measurements to show that compressional velocities for serpentine at 200 MPa (typical pressure at the Moho) is about 0.1 km/s slower than serpentine at  $\sim 400 \text{ MPa}$  (estimated pressure at  $\sim 16 \text{ km}$  depth from the top of the lithosphere). Thus, the steep gradient in the uppermost mantle could not be caused by lithostatic pressure alone. We favor the interpretation that a decrease in degree of hydration and fracture porosity may control the rapid increase in seismic velocities with depth. Mantle velocities of  $8.4 \text{ km/s}$  occurring at 16 km depth may define the lower limit of hydro-alteration within the oceanic lithosphere, and thus may indicate the depth limit where seawater can penetrate. Ranero *et al.*, [2003; 2005] and Ranero and Sallares [2004] have already suggested a depth limit of  $\sim 20 \text{ km}$ , which is based on the thickness of the brittle layer defined by the isotherm of  $600^\circ\text{C}$ . However, we calculated the geotherm for 30 Ma old lithosphere [e.g., Turcotte and Schubert., 1982] and overlie the temperature model with the seismic tomographic model, which indicates that the  $400\text{-}430^\circ\text{C}$  isotherm matches the lower limit of hydro-alteration of the oceanic mantle (assuming that the base of "alteration front" lies where upper mantle velocities reach values of  $\sim 8.4 \text{ km/s}$ ) (Figure 4.7c). Thus the suggested isotherm of  $600^\circ\text{C}$  overestimates the amount of water carried with the incoming lithosphere into the deep subduction zone (Figure 4.7b).

The transition from a tensional fault to a compressional fault may have important implications for percolation of water along the faults. While a tensional crack may support migration of water into the mantle, a compressional fault may prevent effective transfer of water into the mantle. Therefore, the maximum depth down to which water could penetrate would be at the neutral surface between extensional and compressional stresses, or rather slightly above the neutral surface, where bending stresses are too low to induce fracture and thus brittle faulting and hydro-alteration. Estimating the location of the neutral plane between the compressional and tensional regime is difficult and depends

on the rheology, thermal age and stress state of the plate. Based on statistical data, *Seno and Yamanaka*, [1996] proposed that the  $450^\circ\text{C}$  isotherm is a good proxy for the depth limit between the tensional and compressional setting in the trench-outer rise area. The good match between the  $400\text{-}430^\circ\text{C}$  isotherm with the base of the alteration zone (8.3-8.4 km/s isoline) supports the idea that percolation of seawater might indeed be governed by tensional stresses, suggesting that the vicinity of the neutral plane where the tensional regime changes into a compressional regime defines the lower limit of mantle serpentinization.

#### 4.6.4 The role of the Mocha FZ

Alteration of the seismic structure of the oceanic crust may not only be induced by bending-related faulting, but also by the influence of the Mocha FZ which intersects the seismic line at the trench-outer rise area (Figure 4.2). Seismic tomography studies across the Clipperton transform fault revealed anomalously low velocities of  $\sim 1$  km/s less than usual at all crustal depths, which is interpreted in terms of transpression and brittle deformation acting on the fault zone [*van Avendonk et al.*, 2001]. Seismic studies reported that oceanic crust within large fracture zones consists of a thin, intensely fractured, and hydrothermally altered basaltic section overlying serpentinized mantle [e.g., *Detrick et al.*, 1993].

The crustal thickness of  $\sim 7$  km found between profiles-kms 0 and 170 may be expected for oceanic lithosphere formed at the fast Pacific-Farallon spreading center [*White et al.*, 1992; *Carbotte and Scheirer*, 2004]. Crustal thinning from 7.0 to  $< 6.4$  km in the trench coincides roughly with the intersection of the subducting Mocha FZ and the seismic line (Figure 4.2) and hence may suggest that thinner crust is related to the fracture zone. Some amount of this difference in crustal thickness may be attributed to uncertainties of the Moho depth (Figure 4.8d). However, as we described in section 4.5.2, Moho depth uncertainties are lower than 0.3 km in this part of the velocity-depth model. Therefore, a major part of thinning remains unexplained. Seismic measurements and rare earth element inversions have evidenced crustal thinning beneath fracture zones [*White et al.*, 1992]. According to *Detrick et al.*, [1993], the thinning of the oceanic crust in fracture zones may be caused by a reduced magma supply within a broad region near ridge offsets due to the three-dimensional nature of upwelling beneath a segmented spreading center and by tectonic dismemberment of the crust by large-scale detachment faults that form preferentially in the cold, brittle lithosphere near the ends of segments.

Oceanic fracture zones are characterized by a high degree of hydration in both the crust and mantle, and they commonly host bodies of serpentines deep into the oceanic

lithosphere [White *et al.*, 1992]. The presence of the Mocha FZ may suggest a further potential source of fluids and provides an additional and natural explanation for the reduced low velocities in the crust and upper mantle. Furthermore, the projection of the Mocha FZ inland at the magmatic arc corresponds roughly with the location of the Longavi volcano, where the erupted magma composition has been studied [Selles *et al.*, 2004]. These authors interpreted the magma composition to be high-degree mantle melts, highly hydrous and oxidized, formed as response to high fluid input into the subarc mantle. Thus, efficient water transport to the subarc mantle is a plausible effect of dehydration processes during the subduction of the Mocha FZ [Selles *et al.*, 2004].

## 4.7 Conclusions

- Seaward from the area affected by bending-related faulting and the Mocha fracture zone ( $>120$  km seawards of the trench axis), the oceanic crust is  $\sim 7$  km thick and shows a typical P-wave velocity structure generated during fast spreading. Here, uppermost mantle velocities are faster than  $\sim 8.4$  km/s, suggesting an oceanic lithosphere that is relatively dry and undeformed.

- Approaching the trench, seismic velocities decrease in both oceanic crust and mantle, indicating an evolutionary process altering the structure of the lithosphere. This is likely related to an increase in fracture porosity and hydration of the oceanic lithosphere. In addition, extensional outer rise and horst-and-graben faults were mapped in the upper igneous crust and the seaward part of the trench fill sediment, defining the onset of bending-related faulting. Here, some extensional faults reach the seafloor, perhaps forming pathways for seawater into the underlying oceanic crust.

- Reduced upper mantle velocities are confined to a region between the outer and inner trench wall with a maximum thickness of 6-8 km in the uppermost oceanic mantle and coincide with the isotherm of 400-430°C. This depth is interpreted as the lower limit for hydro-alteration within the upper part of the oceanic lithosphere, where extensional stresses dominate.

- The seismic profile crosses the subducting Mocha fracture zone at the trench. In this area inversion of  $P_mP$  arrivals support that crustal thickness is significantly reduced (10-15% thinning). Anomalous crust and mantle associated with the fracture zone may carry fluids and altered crustal and mantle rocks into the subduction zone.





## Chapter 5

# Conclusions and Outlook

### 5.1 Discussion and Conclusions

The P-wave velocity structure of the oceanic Nazca plate obtained along both corridors suggest that the structure of the incoming plate changes systematically within  $>100$  km seaward of the trench axis as the lithosphere approaches the sea trench. The oceanic crust shows a classical mature fast-spreading P-wave velocity structure in the oceanward part outside of the influence of tectonic stresses at the trench-outer rise with uppermost and lowermost crustal velocities of  $\sim 4.2$  and  $\sim 7.2$  km/s, respectively. Seismic analysis of  $P_n$  arrivals reveals fast uppermost mantle velocities of 8.3-8.4 km/s,  $>120$  km seawards of the trench. The velocity structure found in this zone indicates that the oceanic lithosphere is relatively dry and undeformed.

Approaching the Chile trench, crustal and upper mantle seismic velocities decrease to minimum values of  $\sim 7.8$  km/s, indicating an evolutionary process changing the structure of the lithosphere, likely related to an increase in the fracture porosity and hydration of both the oceanic crust and the uppermost mantle. Reduced velocities commence in trench-the outer rise area, and span along the subducting plate. The zone of reduced seismic velocities is accompanied by an increase of basement-relief roughness and fracturing intensity. Offshore southern Arauco peninsula, high resolution seismic reflection reveal clear extensional outer rise faults in the upper crust and the seaward part of the trench fill sediment, where some extensional faults reach seafloor surface. These processes suggest that fracturing and faulting are key processes controlling the evolution of the oceanic lithosphere in the outer rise area.

Similar observations have been observed in many others subduction zones. Table 5.1 shows the minimum values of  $P_n$  velocities and degree of serpentization reported in middle America and Chile. The trend shows that the reduction of  $P_n$  velocities in the

Table 5.1: Degree of serpentinization for different subduction zones.

<sup>a</sup>Mantle velocities in the outer rise area, <sup>b</sup>Degree of serpentinization assuming that the reduced mantle velocities is only due to hydration.

Subduction Zone	<sup>a</sup> $P_n$ velocity (km/s)	Plate age (Ma)	<sup>b</sup> Degree of serpentinization (%)	Reference
Central America ( $\sim 15^\circ\text{N}$ )	7.5-7.8	22	$\sim 17$	<i>Grevenmeyer et al.</i> , [2007]; <i>Ivandić et al.</i> , [2008]
North Chile ( $\sim 23.5^\circ\text{S}$ )	7.5-7.7	42	$\sim 17$	<i>Ranero and Sallares</i> , [2004]
Central Chile ( $\sim 33^\circ\text{S}$ )	7.4-7.7	37	15-25	<i>Kopp et al.</i> , [2004]
South-Central Chile ( $\sim 38^\circ\text{S}$ )	7.7-7.9	30	$\sim 10$	<i>Contreras-Reyes et al.</i> , [2008b]
South-Central Chile ( $\sim 43^\circ\text{S}$ )	7.8-8.0	14.5	$\sim 10$	<i>Contreras-Reyes et al.</i> , [2007]

outer rise is a general feature in subduction zones. Table 5.1 shows that the lowest degree of hydration ( $\sim 10\%$ ) corresponds to the currently heavily sedimented southern central Chile trench. A thick sedimentary cover is believed to limit significantly the amount of fluids entering into the igneous oceanic crust. However, hydration processes affecting the southern Nazca plate offshore Isla de Chiloe were inferred through: (i) efficient inflow of cold seawater into the crust supported by anomalously low heat flow values [*Contreras-Reyes et al.*, 2007], (ii) relative high Poisson's ratios of  $\sim 0.29$  in the uppermost mantle [*Contreras-Reyes et al.*, 2008a] and (iii) swarm seismicity attributed to fluid pressure variations [*Tilman et al.*, 2008]. Therefore, thick sedimentary cover may limit, but not considerably the infiltration of cold seawater into the igneous crust. Percolation of water may occur via high basement outcrops [*Fisher et al.*, 2003b] and trough faults in the seaward part of the outer rise, where the sediment thickness is much thinner and comparable to middle America (300-400 m thick). Once cold seawater is stored in cracks and faults and faulting-intensity increases landward, water trapped within the crust may migrate deeper where larger faults cut into the mantle. In addition, the trench sediments deposition corresponds to a recent process attributed to the Pleistocene glaciation with a rapid sedimentation rate [*Bangs and Cande*, 1997]. Geological evidence shows that the southern central Chile margin was dominated by erosion during the Miocene [*Melnick and Echter*, 2006; *Encinas et al.*, 2008], when the thickness of the trench fill was much thinner than today. Thus, "paleo" hydration processes may also explain the low mantle velocities under

the thick trench fill (in the landward side of the outer rise).

Bending-related faulting is a natural explanation as cause for hydro-alteration of the oceanic lithosphere in subduction zones, where deep extensional faults have been mapped with multichannel seismic reflection data such as middle America [Ranero *et al.*, 2003] and southern central Chile (35-39°S) [Diaz-Naveas, 1999; Grevemeyer *et al.*, 2003]. Similarly in subduction zones where an intense set of bending faults are visible from the multi-beam bathymetry such as in north [Ranero and Sallares, 2004] and central Chile [Kopp *et al.*, 2004]. Offshore Isla de Chiloe, there is no available MCS data to study possible faulting processes affecting the oceanic crust, and surface-cutting faults are not visible in the seafloor bathymetric image due to the thick sedimentary cover [Contreras-Reyes *et al.*, 2007]. A direct effect of the bending plate on the faulting history of the oceanic lithosphere in this area is not evident. Tilmann *et al.*, [2008] suggest that the oceanic crust offshore Isla de Chiloe must be perversely fractured. Although, not necessarily due to bending related faulting. These authors argued that no pronounced outer rise buldge exists on the very young Nazca plate formed at the Chile Rise (south of the Valdivia FZ), and proposed that the regional stresses such as a ridge push or the progression of the seismic cycle on the megathrust [Christensen and Ruff, 1988] are more dominant than bending-related trench-perpendicular normal faulting. In contrast, the oceanic Nazca plate formed at the Pacific-Farallon spreading center (north of 40°S) is much older and rigid. A pronounced outer rise buldge exists (Figure 4.3), and several normal faults have been imaged in this area [Diaz-Naveas, 1999]. Establishing a relationship between degree of serpentinization and plate age based on the published results shown in Table 5.1 is not straightforward. The degree of serpentinization in central Chile is higher than in north Chile, despite that the oceanic plate in the north is much older. The stress field in the outer rise area off central Chile is strongly affected by the incoming/subducting Juan Fernandez Ridge and their fault system [Ranero *et al.*, 2006; Clouard *et al.*, 2007]. In addition, subduction zones in general are affected by dynamic stresses, induced by forces such as a slab pull, ridge push, and drag forces, which also affect the stress state of the lithosphere prior to subduction [Kanamori, 1971; Clouard *et al.*, 2007]. Thus, actual mechanisms often deviate from the simple idea of a bending plate. This may be controlled also by regional tectonic stresses [Mueller *et al.*, 1996a; Mueller *et al.*, 1996b; Tilmann *et al.*, 2008]. Future researches should also take into account others parameters such as rheology, thermal plate age, loading history and their interrelationship in order to understand the state of stress across the plate, and hence the impact of faulting on hydration.

Ranero *et al.*, [2003; 2005], and Ranero and Sallares [2004] have suggested that the isotherm of 600°C (maximum temperature for brittle faulting) corresponds to a good

proxy for the maximum penetration depth of outer rise extensional faulting and mantle hydration. However, the seismic results of this dissertation suggest that the 400-430°C isotherm match the depth limit of hydro-alteration of the oceanic mantle. As I described in chapter 4 extensional stresses may allow seawater to percolate deep into the mantle, while compressional stresses prevent effective transfer of water into the mantle. The transition depth from a tensional to compressional regimes corresponds to the neutral plane and may represent the maximum depth down to which water may actually penetrate. Estimating the location of the neutral plane between the compressional and tensional regime is difficult, and depends on the rheology, thermal age and stress state of the plate. Based on statistical data, *Seno and Yamanaka*, [1996] proposed that the 450°C isotherm is a good proxy for the depth limit between the tensional and compressional setting in the trench-outer rise area. The good match between the 400-430°C isotherm and the base of the alteration zone supports the idea that percolation of seawater might indeed be governed by tensional stresses, suggesting that the vicinity of the neutral surface where the tensional regime grades into a compressional regime defines that maximum depth of mantle serpentinization. The location of the neutral plane may correspond to the maximum depth of serpentinization rather than the location of the isotherm  $\sim 600^\circ\text{C}$ . Estimation of the depth of the neutral plane deserves future researches and provides an upper bound for the maximum depth of mantle hydration, and hence also an upper bound for the amount of water carried to the deeper subduction zone.

Hydration of the incoming/subducting plate plays an important role on intermediate-depth earthquakes. As the oceanic crust and mantle dehydrates at depths of 50-300 km [*Ruepke et al.*, 2004], the increase of pressure decreases the effective normal stress and hence promotes brittle failure at those depths [*Meade and Jeanloz*, 1991; *Tobi et al.*, 2002]. Thus, the considerable amount of water stored in the southern central Chile trench-outer rise and later released in the deep subduction may be an important processes for the nucleation of megathrust earthquakes in the region. In addition, a considerable amount of earthquakes may occur by reactivation in preexisting structures formed at the initiation of the slab subduction at the trench. As *Savage* [1969] and *Kirby et al.*, [1996] pointed out, faults produced at shallow depth in the trench outer rise setting being reactivated at greater depths may be useful for the assessment of seismic hazard of the region.

## 5.2 Outlook

This seismic study suggested that hydration-alteration of the incoming oceanic is indeed happens in the trench outer-rise area offshore southern central Chile. Despite the

thick sedimentary cover on top of the oceanic crust, percolation of seawater through bend faults and high basement outcrops are evidenced by low heat flow values, normal and horst-grabens faults and reduction of seismic velocities. Additionally, relative high seismic Poisson's ratios in the uppermost mantle suggest the presence of fluids in the oceanic crust at the outer-rise. To further quantify the areal extent of the hydro-altered oceanic crust and mantle offshore south central Chile, future seismic investigations are needed. Additional mapping of Poisson's ratios and 1D and 2D amplitude modelings would enable the comprehensive estimation of the amount of the fluid input in subduction zones.

A pioneer estimation of the maximum depth of mantle's alteration using an active seismic experiment was presented in chapter 4, which was possible to the recording of long and deep penetration of mantle refractions. Thus, a preliminary explanation for the interrelation between plate age and the maximum brittle depth of the oceanic lithosphere was established. However, to better understand these processes and their relationship with tectonic stresses affecting the oceanic lithosphere at subduction zones more seismic experiments with higher resolution and deeper ray coverage into the mantle are required. In addition, seismic study of the mantle velocity gradient is crucial for understanding the mechanical behavior of mantle rocks partly serpentized at large depths, and can be used to compute the depth limit of mantle hydration, and hence to estimate the amount of water carried by the subducting slab to the deeper subduction zone.



# Appendix A

## Monte Carlo Test

In order to study the accuracy of the final model, we employed the Monte Carlo method [Korenaga *et al.*, 2000]. The uncertainty of a nonlinear inversion can be expressed in terms of the posterior model covariance matrix [e.g., Tarantola, 1987], which can be approximated by the standard deviation of a large number of Monte Carlo realizations assuming that all the realizations have the same probability [e.g., Tarantola, 1987]. The uncertainty estimated by this method should be interpreted as the uncertainty for our model parameters (*i.e.*, starting velocity model and smoothing constraints). The procedure to estimate velocity uncertainties consisted of randomly perturbing velocities of our reference model (Figure A.1). We generated 100 random initial velocity models by adding smooth perturbations randomly distributed (maximum velocity perturbations of  $\pm 0.8$  km/s at the top and  $\pm 0.4$  km/s at the bottom of the crustal reference models shown in Figure A.1). Maximum perturbations for the Moho reflector depth were  $\pm 1.5$  km. In addition to the perturbed reference models we produced 100 so-called noisy arrival time sets constructed by adding random phase errors ( $\pm 50$  ms) and common receiver errors ( $\pm 50$  ms) to the original data set [e.g., Korenaga *et al.*, 2000]. Then we performed a tomographic inversion for each velocity model with one noisy data set, in order to estimate not only the dependence of the solution on the reference model but also the effect of phase arrival time picking errors. The mean deviation of all realizations of such an ensemble is considered to be a statistical measure of the model parameter uncertainties [e.g., Tarantola, 1987]. All of the Monte Carlo inversions converged in less than 7 iterations to  $\chi^2 \sim 1$ , where the model error is equal to the data uncertainty. In the upper mantle, we constructed several initial models by varying the uppermost mantle velocity between 7.5 to 8.5 km/s and the mantle velocity gradient between 0 and  $0.04$  s<sup>-1</sup>, respectively. The final average models and their uncertainties for profile P01a and P03 are plotted in Figures 3.4c and 3.4d, respectively.

We prepare the  $V_s$  starting model by searching the best 1-D velocity model using

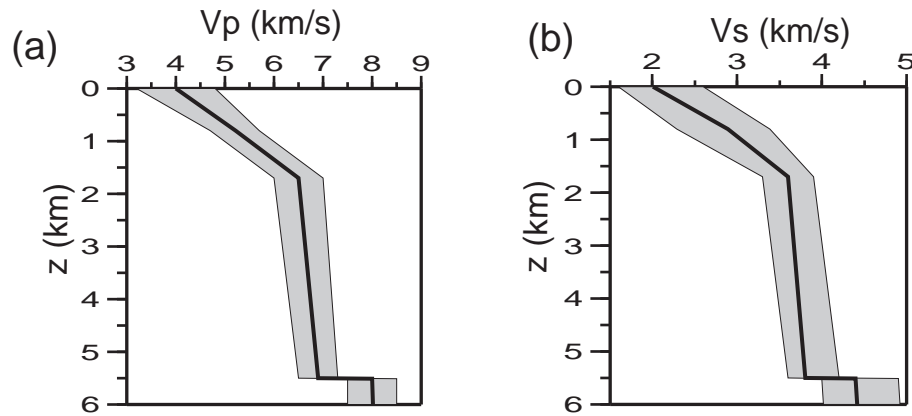


Figure A.1: (a) Velocity reference models for the crustal part of the P-wave velocity models (black line). These models are based on the 1-D velocity models that best fits the  $P_g$  and  $P_mP$  arrivals for each profile. (b) Initial shear wave velocity model and range of velocities for Monte Carlo ensembles. For (a) and (b) velocity-depth profiles are shown beneath sediments, and grey areas represent the possible variations of the velocity randomization.

a trial and error scheme. This velocity model is exhibited in Figure A.1b (black line). Similarly to the P-wave modelling, we perturbed this reference model and generated 100 initial models. Grey regions in Figure A.1b represent the possible variations of the velocity randomization. All of the Monte Carlo inversions converged in less than 5 iterations to  $\chi^2 \sim 1$ . Figures 3.5a and 3.5c show the average final S-wave velocity model and its standard deviations.



## Appendix B

### $S_n$ Traveltime sensitivity

We studied  $S_n$  velocity and different velocity gradients by keeping the shear velocity information above the Moho interface gained from previous crustal seismic tomography. Figure B.1 shows the record section of OBS 02, which displays an example of the onset of the  $S_n$  phase with an offset up to  $\sim 40$  km. The best-fitting shear wave uppermost mantle velocity is about 4.3 km/s, which is slow compared with dry peridotite ( $> 4.7$  km/s). A comparison with a higher  $S_n$  velocity of 4.6 km/s produces a  $S_n$  travel time misfit of  $\sim 0.5$  s, and so we conclude that the seismic data can only be explained by uppermost velocities as slow as 4.3 km/s.

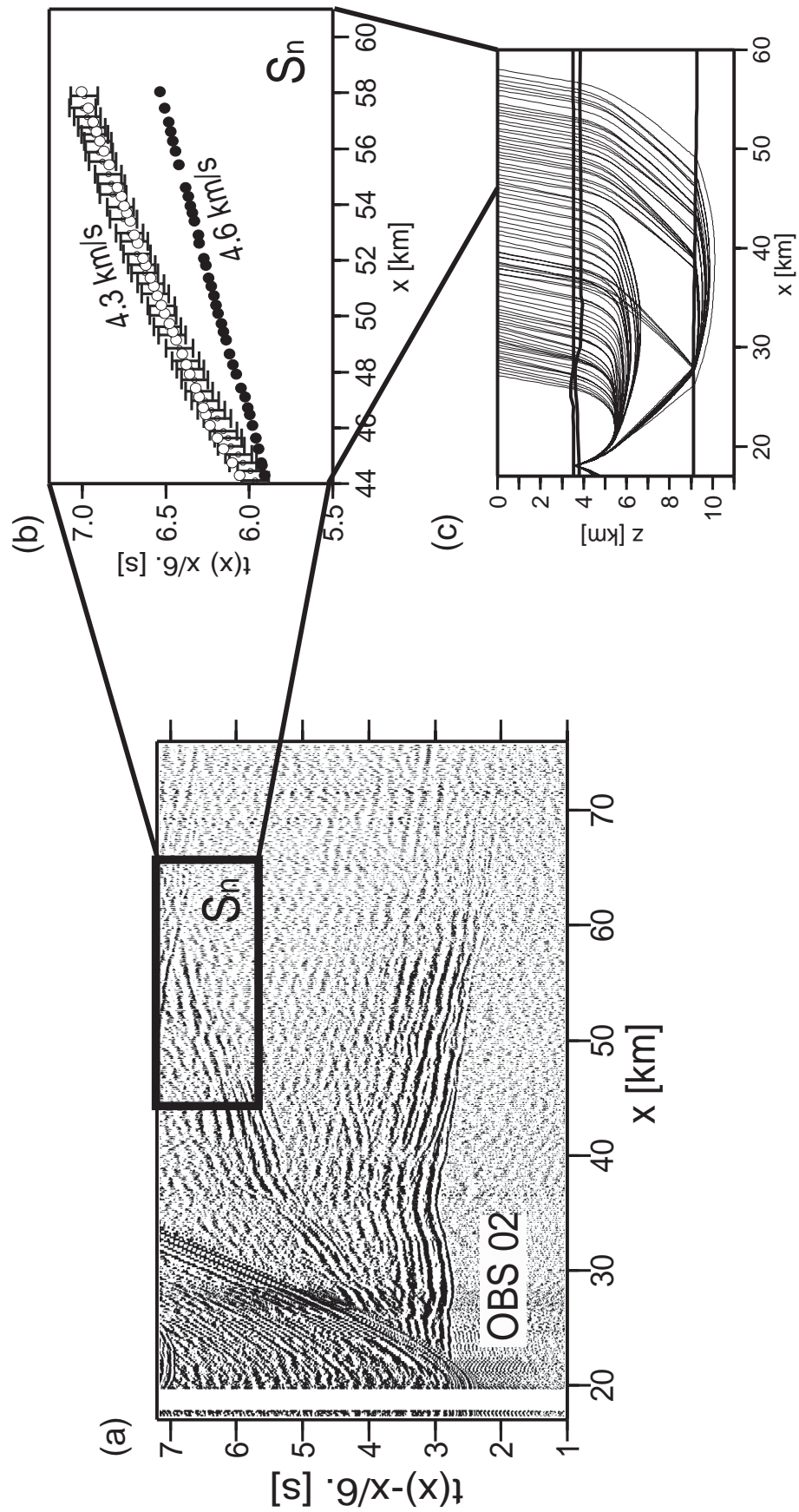


Figure B.1: (a) Detailed forward analysis of  $S_n$  travel times for OBS 02. (b)  $S_n$  oceanic phases can only be predicted with values as slow as 4.3 km/s (white dots), typical uppermost S-wave velocities of 4.6 km/s produce a misfit  $> 450$  ms (black dots). (c) Corresponding ray paths.

## Appendix C

# Amplitude Modelling

We calculated synthetic seismograms using the reflectivity method of *Fuchs and Mueller* [1971]. Because the reflectivity method can deal only with constant-velocity layers, the velocity gradients were approximated using several uniform-velocity layers with a thickness of half the smallest wavelength present [*Chapman and Orcutt*, 1985]. We modelled the most prominent amplitude pattern of the southern branch of OBS 03 based on the final P- and S-wave velocity models derived by the tomographic inversion (Figures 3.4 and 3.5). We have chosen this branch of the station because it is less affected by the influence of the high topography of the basement outcrop (Figure 3.1), which clearly produces 2D effects on the traveltime pattern (see for example Figure 2.2). Nevertheless, two-dimensional effects linked to the variability of the basement topography and diffractions affect adversely the fit between the data and theoretical curves that are computed on a horizontal layer assumption. Figure C.1 exhibits the final 1D velocity model obtained by using the reflectivity method, and quality factors ( $Q_p$  and  $Q_s$ ), and density are shown. Figure C.2 shows the comparison of the data with the synthetic seismograms. In general, all major arrivals were reproduced by the synthetic models. A striking feature of the record section are the high-amplitudes of  $P_mP$  reflections at around 30 km offset, which marks the onset of the bright spot associated with the triplication point of the  $P_g$ ,  $P_mP$  and  $P_n$  phases. This observation is nicely produced by the synthetic seismograms (Figure C.2). Moho S-wave reflections  $S_mS$  of noticeable amplitude between  $\sim 17$  and  $\sim 35$  km offset are also clearly produced by the reflectivity method, as well as all the main P-wave multiples (Figure C.2).

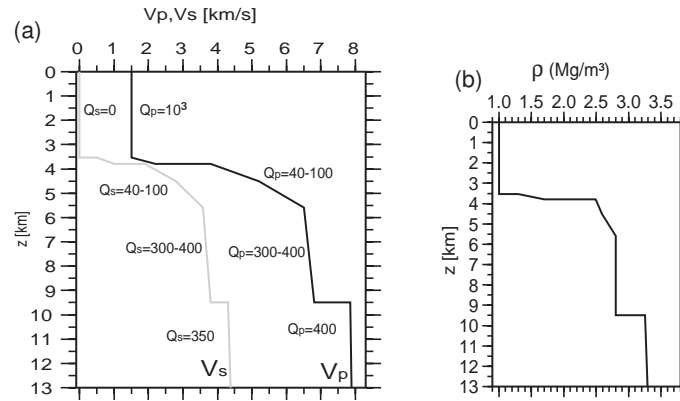


Figure C.1: (a) 1D  $P$ - and  $S$ -wave models determined from the amplitude analysis, and quality factors  $Q_p$  and  $Q_s$  are shown. (b) 1D density model used during the computation of the synthetic seismograms.

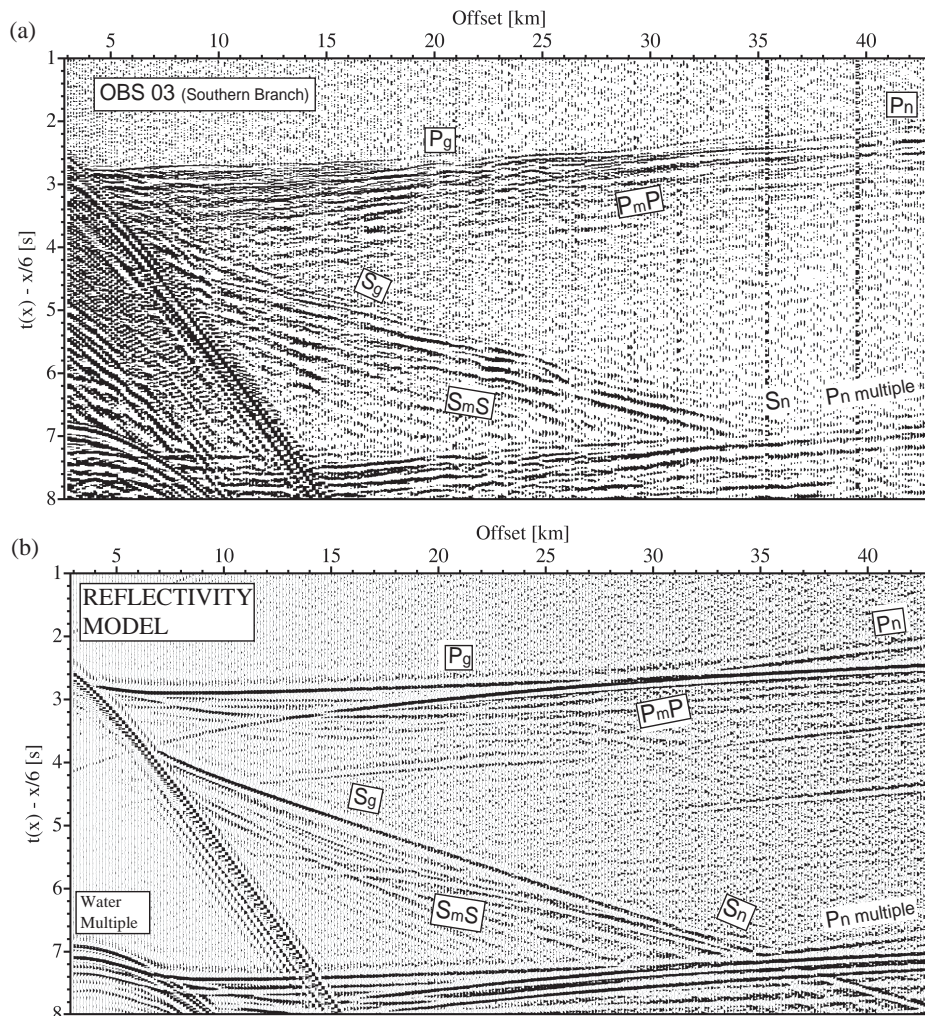


Figure C.2: (a) Southern branch of record section OBS 03 (Hydrophone component) and main arrivals identified. (b) Synthetic seismograms at 150-m spacing computed using the reflectivity method based in our 1D final model shown in Fig. C.1.

## Appendix D

# Structure of the accretionary convergent margin offshore of southern Arauco Peninsula, Chile at $\sim 38^\circ$ S

A joint interpretation of swath bathymetric, seismic refraction, wide-angle reflection and multi-channel seismic data was used to derive a detailed tomographic image of the Nazca-South America subduction zone system offshore southern Arauco peninsula, Chile ( $\sim 38^\circ$ S). Here, the trench basin is filled with up to 2.2 km of sediments and the Mocha Fracture Zone is obliquely subducting underneath the South American plate. The velocity model derived from the tomographic inversion reveals two prominent velocity transition zones characterized by steep lateral velocity gradients, resulting in a seismic segmentation of the marine forearc. The margin is composed of three main domains; (1) a  $\sim 20$  km wide frontal prism below the continental slope with  $V_p < 3.5$  km/s, (2) a  $\sim 50$  km area with  $V_p = 4.5$ - $5.5$  km/s, interpreted as a paleo accretionary complex, and (3) the seaward edge of the Paleozoic continental framework with  $V_p > 6.0$  km/s. Frontal prism velocities are noticeably lower than those found in the northern erosional Chile margin, confirming recent accretionary processes in south central Chile.

### D.1 Introduction

Subduction at convergent margins has a major impact on both the incoming plate, which is forced to subduct, and the overriding block. At the trench, convergence between subducting and overriding plate causes either erosion of the upper plate typically when the sedimentary trench fill is  $< 1$  km and the convergence rate is  $> 6.0$  cm/yr or accretion

when the trench sediment thickness exceeds 1 km and convergence rate is  $< 7.6$  cm/yr [Clift and Vannuchi, 2004]. Seismic data can be used to study the structure of incoming and overriding plate and reveal the interaction between both plates causing continents to grow or shrink as they collide in the trench.

The southern central Chile margin hosted the rupture area of the great 1960 Chilean earthquake ( $M_w \sim 9.5$ ) [Cifuentes, 1989; Barrientos and Ward, 1990] and is characterized by a filled trench confined between two main oceanic features: the Juan Fernandez Ridge and the Chile Rise (Figure 4.1). The southern central Chile margin was characterized by Bangs and Cande [1997] using structural constraints from multichannel seismic reflection data. Main features were a 15-20 km wide accretionary prism and a  $\sim 2$  km thick trench fill. The backstop underlying the continental slope and its velocity structure, however, were poorly resolved. Krawczyk *et al.*, [2006] used seismic refraction and wide-angle reflection data from an amphibious experiment to yield structural constraints of the entire subduction zone system offshore of the southern Arauco peninsula at  $\sim 38^\circ\text{S}$ . Their final velocity-depth model concentrated on the nucleation area of the great 1960 earthquake more than 80 km landwards of the trench and put less emphasis on the marine forearc. To refine the crustal model of the accretionary complex, marine forearc and downgoing plate, we re-analysed a subset of the SPOC (Subduction Process Off Chile) data [Krawczyk *et al.*, 2006] and extended the profile across the trench-outer rise seaward of the trench to study the impact of bending-related faulting on the structure of the incoming plate (see chapter 4). We integrated multi-channel seismic reflection (MCS) data and seismic refraction and wide-angle data into our inversion and performed a joint refraction and reflection travel-time tomography to obtain a detailed velocity model of the marine forearc and the incoming/subducting oceanic lithosphere off Arauco peninsula, south central Chile ( $\sim 38^\circ\text{S}$ ).

An important aspect of this work is the seismic characterization of the continental margin off south central Chile. In this area, south of the Juan Fernandez Ridge (JFR) and north of the Chile Triple Junction (CTJ) the Chilean margin is characterized by accretion (Figure 4.1). Seismic data image up to 2.2 km of trench fill, resulting in an active frontal prism roughly 15-25 km wide [Bangs and Cande, 1997; Diaz-Naveas, 1999]. The proposed contact between the metamorphic/metasedimentary basement (continental backstop) and the young frontal prism is poorly imaged with seismic reflection data, and its crustal structure was mostly conceptual. A detailed tomographic seismic image of the upper plate derived from wide-angle data is presented in this paper for the first time. In addition, the erosional Chile margin to the north of the JFR consists of a frontal prism comprised of slope debris and a middle slope prism of continental basement framework rock [von Huene and Ranero, 2003]. Its crustal structure has been investigated with

multichannel reflection [von Huene and Ranero, 2003] and seismic refraction and wide-angle reflection data [Sallares and Ranero, 2005] and can be compared to the results from this study. We present new geophysical constraints for our understanding of erosion and accretion processes along the Chilean margin.

## D.2 Characterization of geological structures from seismic reflection and bathymetric data

Seismic reflection and swath bathymetric data were acquired offshore Arauco peninsula during the SPOC and TIPTEQ projects using R/V SONNE in 2000/2001 and 2004/2005, respectively [Reichert *et al.*, 2002; Krawczyk and SPOC Team, 2003; Flueh and Greve-meyer, 2005; Scherwath *et al.*, 2006b]. The seismic signals for the seismic reflection experiment were generated by a tuned set of 20 airguns with a total volume of 51.2 litres. The multi-channel seismic reflection data were analysed using standard processing, including re-binning, normal-move out correction, stacking, deconvolution, and post-stack time migration. A predictive deconvolution with two gates, for the shallow sedimentary events and the deeper crustal events, was applied before the stack. A space and time variant frequency filter prior to a post-stack migration completed the processing flow [Reichert *et al.*, 2002]. Seismic reflection data are displayed in Figure D.1.

### D.2.1 The frontal accretionary prism

Seismic reflection data reveal a well-developed frontal thrust and current active off-scraping of the trench fill (Figure D.1c). A succession of small sedimentary ridges define the onset of the pre-accretionary prism, which strikes parallel to the trench axis and coincides with a set of reverse faults imaged in the seismic reflection data (Figure D.1). The thrust faults develop at depth, and some of them reach the seafloor crosscutting the entire trench fill sequence (Figure D.1c). The largest accretionary ridge shown in Figure D.1c marks the onset of the lowermost slope, and its stratigraphy reveals compressional folding.

### D.2.2 The forearc basin

The Arauco forearc basin consists of a depression between the Coastal Cordillera and the horst block of the basement filled with more than 3 km of late Cretaceous and Tertiary clastic sediments in the depocenter [Gonzalez, 1989]. From base to top, the shelf basin consists of (1) Senonian; (2) Paleocene-Eocene; (3) Oligocene-Miocene; and (4) Pliocene to Quaternary clastics [Gonzalez, 1989]. The post-stack time migration cross section shown in Figure D.1a images the sedimentary Arauco basin just 20 km north of the Isla Mocha

(Figure 4.2). Here, the depocenter of the basin lies 50 km landward of the deformation front with maximum sediment thickness of 1.7 s TWT. Some inverted faults cutting the metasedimentary basement can be identified by offsets at the eastern part of the depocenter (Figure D.1a). A striking feature at profile-km  $\sim 276$  is the deep incision left by the path of the paleo-Pellahun submarine canyon. This is manifested by the deep erosion through all substrates, from unlithified shelf sediments to the metasedimentary basement. Another striking feature shown in Figure D.1a is the uplifted shelf that belongs to the uplifted part of the Arauco peninsula [Kaizuka *et al.*, 1973; Nelson and Manley, 1992].

### D.3 Results and Discussion

Our interpretation of the margin structure is summarized in Figure D.2. The seismic segmentation of the continental margin is defined by two high horizontal velocity gradients, one located at the shelf break and the other  $\sim 75$  km from the deformation front. Figure D.2 shows the lateral variation of the uppermost basement velocity within the marine forearc (below the slope sediments and forearc basin). The horizontal velocity gradients define three main domains: (1) a wedged-shaped body of low velocity ( $< 3.5$  km/s) below the trench slope, which is interpreted as an active frontal prism, (2) a paleo accretionary complex or metamorphic basement with  $V_p = 4.5\text{-}5.5$  km/s, and (3) the seaward edge of the Paleozoic continental framework ( $V_p > 6.0$  km/s). The young frontal prism is approximately 20 km wide and hence in close agreement with previous seismic reflection results presented by Bangs and Cande, [1997] and Diaz-Naveas [1999]. The most landward velocity transition zone coincides roughly with the onset of intraplate earthquakes located by Haberland *et al.*, [2006], which are plotted in Figure 4.7b.

#### D.3.1 Seismic segmentation of the accretionary margin

Active frontal accretion processes at the seaward edge of the young accretionary wedge is evident by the style of deformation of the trench fill (Figure D.1c). Here, sediment ridges represent a small fold-and thrust belt caused by compressive sediment deformation (reverse faults). Reverse faults imaged within the trench basin control the current style of accretion. The transition from the upper slope to the continental shelf marks a gradual transition to stronger material, affecting the wedge stability and hence taper of the margin wedge [Davis *et al.*, 1983]. The steep slope of the continental slope ( $\sim 7^\circ$ ) offshore southern Arauco peninsula may indicate a transition from features formed during Miocene tectonic erosion [Encinas *et al.*, 2008] to accretion at the present. Alternatively, the accretionary wedge may have thickened rapidly vertically during the Pliocene as a result of basal accretion beneath the prism and resulted in the steep slope. The accretionary prism is made up of trench sediments added to the toe of the margin, resulting in the seaward migration



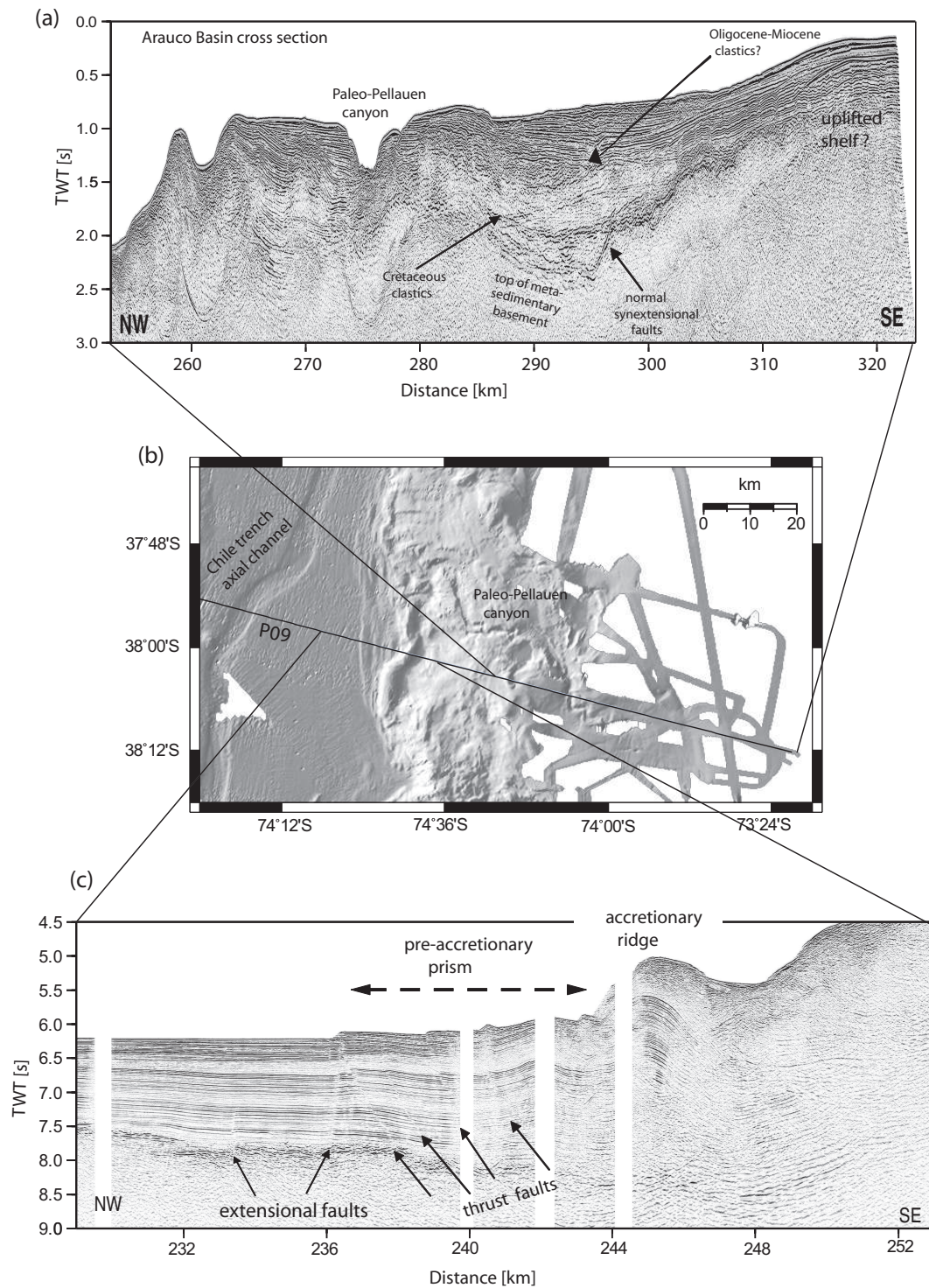


Figure D.1: (a) Shelf section of seismic line P09. (c) Offsets in the sediment-trench stratigraphy indicate the existence of reverse faults cutting the entire sedimentary sequence and some hundred meters of the oceanic basement. The expression of these processes at the seafloor surface corresponds to a set of accretionary ridges seen in the bathymetry (b), and defines the frontal thrust surfaces.

of the trench axis.

The abrupt increase of seismic velocities roughly 60 km landward of the shelf break (at km-312) indicates a change of rock-type (Figure D.2), and might be associated with the seaward edge of the truncated Paleozoic continental framework [Mordohovich, 1974], whereas the inner wedge sandwiched between the frontal prism and this seismic "boundary" may correspond to a paleo accretionary complex. Unfortunately, drilling did not sample crust from this geological unit but is confined to coastal sites, where basement rocks are of Paleozoic age [Mordohovich, 1974]. Based on the location of an exploratory well marked in Figure 4.2, the Paleozoic basement rock found here is located landward of the seaward edge of the continental framework (Figure D.2a). Therefore, the composition and age of the proposed paleo accretionary complex still remains unclear. It is interesting to note that the presence of a similar seismic "boundary" at roughly the same distance from the deformation front (70-80 km) has been observed further to the south [Schervath *et al.*, 2007], and thus may form an integral part of the marine forearc.

The paleo accretionary complex has a higher degree of consolidation and lithification than the frontal prism but lower than the Paleozoic continental framework. Alternatively, the unit interpreted as a paleo accretionary complex might be part of the continental framework deformed and metamorphosed during a phase of tectonic erosion. However, the remarkable high lateral velocity gradient from 5.5 km/s to >6.0 km/s favors a rapid change in rock type (Figure D.2), and hence alternation between accretion and erosional phases. The size of the paleo accretionary complex should have been much larger at the end of the accretion phase, when the complex was formed. Thereafter, an integral part of the accretionary complex was tectonically eroded [Mordohovic, 1981; Melnick and Echtler, 2006; Encinas *et al.*, 2008]. At present, the width of ~50 km of the paleo accretionary complex represents the remaining material left after the last erosional phase, which took place in the Miocene according to Melnick and Echtler, [2006] and Encinas *et al.*, [2008]. Assuming alternation between accretion and erosion phases and based on the age of the oldest shelf sediments (Senonian age), we estimate that the paleo accretionary complex might be formed of Jurassic age.

The location of the seaward edge of the Paleozoic continental framework is well correlated with the onset of intraplate seismicity (Figure 4.7b) [Haberland *et al.*, 2006], reflecting the interseismic transpressional deformation of the forearc due to the subduction of the Nazca plate. In addition, this region coincides with the coastal uplifted area of the Arauco peninsula [Kaizuka, 1973] and belongs to the area of the Mocha block, which is characterized by high rates of modern seismicity [Habermann *et al.*, 1986]. The interrelationship

between intraplate seismicity and uplift of the Isla Mocha is complex, and may be associated to asperities on the plate-interface beneath the Mocha block and the local structures within the upper plate [Kaizuka, 1973; Nelson and Manley, 1992]. Subduction of the Mocha FZ may explain the strength of the asperity beneath the Mocha block [Barrientos and Ward, 1990], which may induce upward stresses propagating through the overriding plate and activating crustal faults. Thus, intraplate seismicity in the upper and fragile part of the overriding plate could be induced, at least in part, by the subduction of the

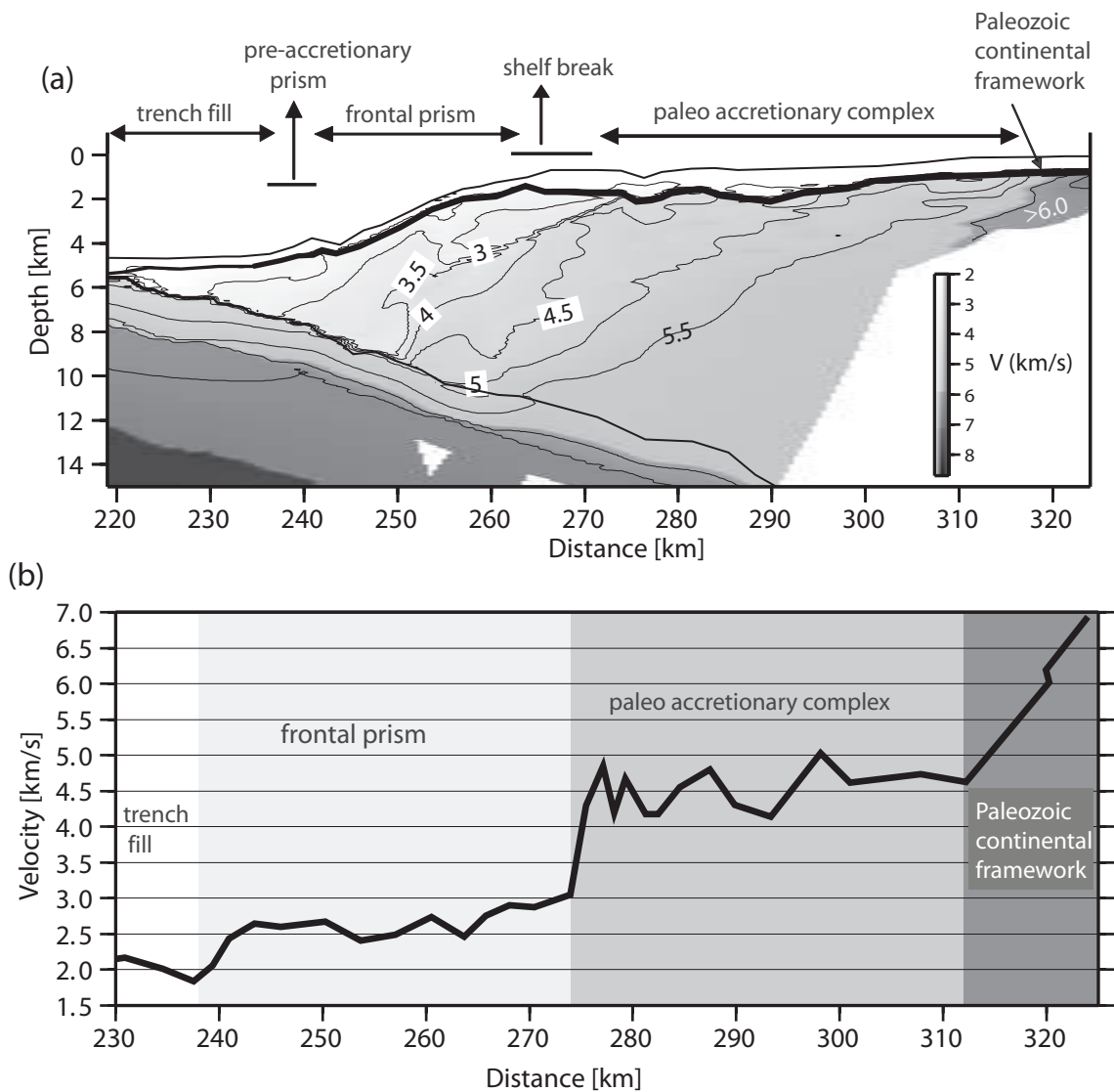


Figure D.2: (a) Detailed tomographic image of the marine forearc complex, showing the seismic segmentation of the accretionary margin wedge. (b) Extracted velocities along the thick black line shown in (a), which landward of the lowermost slope corresponds to the uppermost basement velocities below the slope and forearc basement sediments. Note the strong horizontal velocity gradients at the slope break and seaward edge of the Paleozoic continental framework, which may suggest a change in rock type.

Mocha FZ.

### D.3.2 Subduction of sediments - the subduction channel

Subduction of poorly consolidated sediments (subduction channel) beneath the overriding accretionary prism and crystalline block are usually assumed to be characterized by lower seismic velocities than the overriding structures, and thus may form a low velocity zone (velocity inversion). However, this velocity-contrast has not yet been constrained by seismic refraction experiments. A low velocity layer cannot be resolved by the resolution of our refraction data, especially landward of the accretionary prism where the velocities are poorly constrained as is shown by the high velocity uncertainties in Figures 4.8a and 4.8c. Our model, however, favors a more gradual velocity structure above the plate boundary and hence could not resolve a subduction channel.

The existence of a decollement zone and hence subduction channel is usually derived from multi-channel seismic reflection data (strong reflector, often with reversed polarity) or in ancient accretionary prisms in the form of tectonic melanges and duplex structures [Kitamura *et al.*, 2005]. Diaz-Naveas [1999] used depth migrated MCS data to yield a  $\sim 1$  km thick layer of subducting sediments above the top of the downgoing plate along profile ENAP-4 (Figure 4.1). The velocity-contrast between the overlying prism and subducted sediments was rather small, roughly comparable with the velocity uncertainties of our tomographic model. Krawczyk and SPOC Team [2003] and Gross *et al.*, [2007] used near-vertical reflection data to image a region of high reflectivity with a thickness of 2-5 km above the plate boundary, which is located below the coast line at a depth of about 25 km at  $\sim 38.2^\circ\text{S}$ . These authors interpret this reflectivity pattern as a subduction channel, which extends arcward for roughly 30 km [Gross *et al.*, 2007]. However, in this case the thickness of the subduction channel would exceed the thickness of the trench fill and the thickness of the subduction channel imaged offshore [Dias-Naveas, 1999; Bangs and Cande, 1997]. Therefore, the observed reflectivity pattern may represent laminated lower crust or shear zones within the continental crust, rather than a subduction channel.

### D.3.3 Comparison with the northern erosional Chile margin

Figure D.3 compares 2D-tomographic velocity models from the accretionary southern central and erosional northern Chile margin. von Huene and Ranero, [2003] and Sallares and Ranero, [2005] pointed out that the overriding plate in north Chile is mainly made of arc-type igneous basement, where the front of the margin is probably fluid-saturated, metamorphosed and disaggregated by fracturing as a consequence of frontal subduction erosion. The trench is sediment starved, the margin has no forearc basin, and the extensional regime across the continental slope has caused gravitational destabilization of the

margin framework resulting in steepening of the margin related to progressive subduction erosion [von Huene and Ranero, 2003, Ranero et al., 2006]. Offshore southern Arauco peninsula, in contrast, the trench is shallower and filled with up to 2.2 km of sediments, the continental shelf is broad (70-80 km), and has a well developed forearc basin. Uplift events and focal mechanism of intraplate events suggest that the margin suffers from compressional tectonics [Kaizuka et al., 1973; Barrientos and Ward, 1990; Haberland et al., 2006].

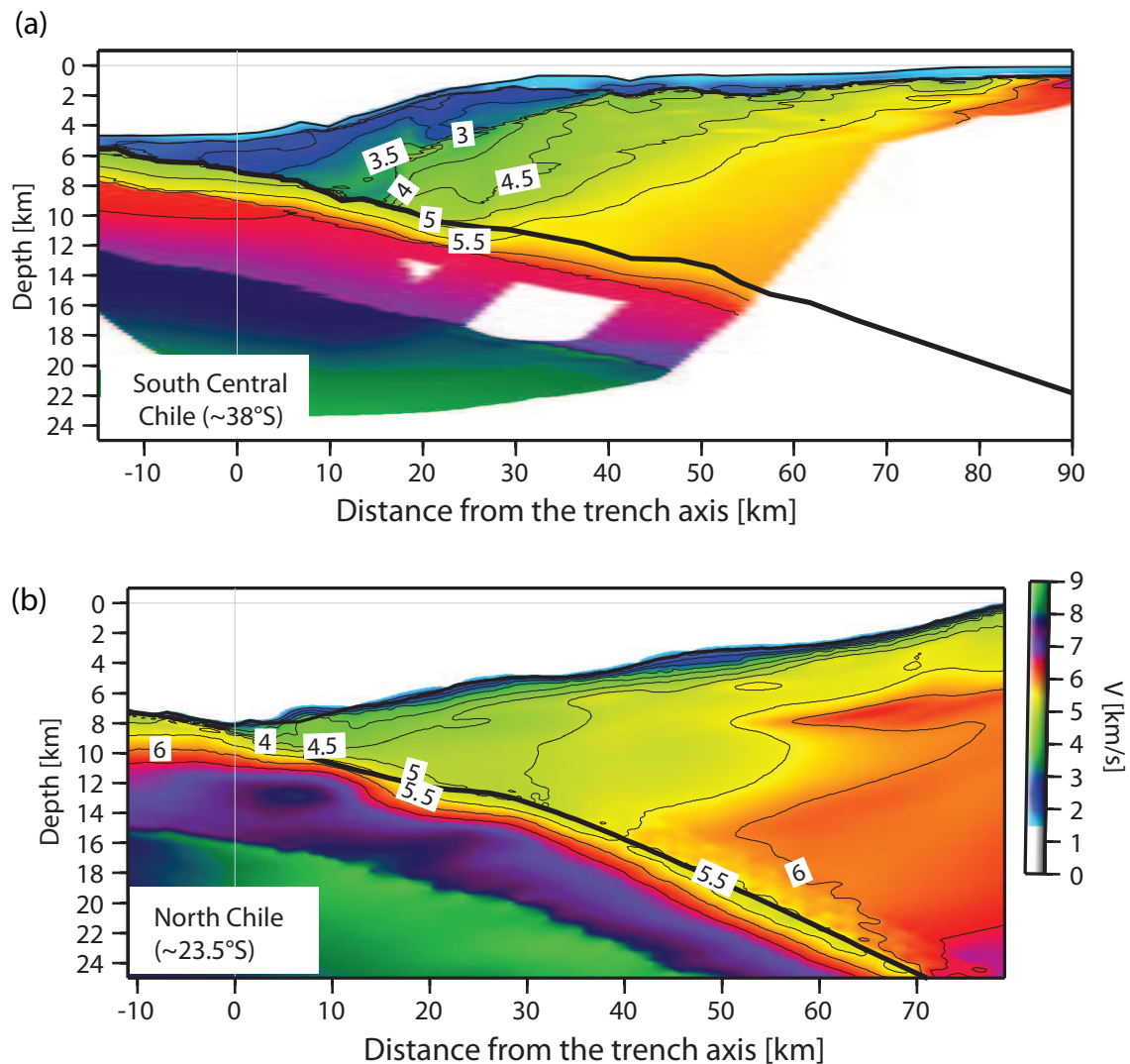


Figure D.3: Direct comparison of the velocity depth-models between (a) the young accretionary margin offshore of southern Arauco peninsula and (b) the northern erosional margin off Antofagasta [Sallares and Ranero, 2005].

A clear difference between these margins inferred from our tomographic model is the velocity structure at the front of the margin wedge. The frontal prism seaward of the

shelf break off south central Chile has seismic velocities lower than 4 km/s, while off north Chile velocities are faster than 4 km/s (Figure D.3). This observation indicates that the front of the southern central Chile margin is composed of sediments, indicating accretionary processes. Off north Chile, in contrast, velocities  $>4$  km/s are characteristic of igneous rocks rather than sedimentary rocks [Sallares and Ranero, 2005]. Velocities in the paleo accretionary complex (seaward of the shelf break) are  $>4$  km/s (Figure D.3a) and hence similar to the metamorphosed igneous continental crust off north Chile (Figure D.3b). Metasedimentary and metamorphosed rocks are therefore indistinguishable in terms of seismic velocities. Nevertheless, the seismic tomography for the accretionary southern central Chile margin suggests a clear seismic segmentation, supporting episodes of accretion. In contrast, at the erosional northern Chilean margin, fracturing, alteration, and erosion have continuously lowered the velocity to the seaward edge of the margin, providing a gradual change of seismic velocity within the margin wedge.

#### D.4 Summary

- A lateral seismic segmentation of the margin wedge was inferred from the tomographic model. Three main units are imaged: (1) a 15-20 km wide frontal accretionary prism below the continental slope with  $V_p < 3.5$  km/s, (2) a  $\sim 50$  km wide block with  $V_p = 4.5$ -5.5 km/s, perhaps representing a paleo accretionary complex or metamorphic basement, and (3) the truncated seaward edge of the Paleozoic continental framework with  $V_p > 6.0$  km/s.

- The seaward edge of the Paleozoic continental framework coincides with the onset of continental intraplate seismicity and the uplifted shelf offshore southern Arauco peninsula.

- Frontal prism velocities are clearly lower than in the seaward section of the northern erosional Chile margin, where rocks are of metamorphosed igneous composition rather than sediments. Thus, the southern central accretionary Chile margin is characterized by a clear seismic segmentation, in contrast to the northern erosional margin, where seismic velocities gradually decrease towards the trench, interpreted to be linked to hydro-fracturing and erosional processes [von Huene and Ranero, 2003; Sallares and Ranero, 2005].

# Bibliography

- [1] ANCORP Working Group (2003), *Seismic imaging of a convergent continental margin and plateau in the central Andes (Andean Continental Research Project 1996 (ANCORP'96))*, J. Geophys. Res, 108(B7), 2328, doi:10.1029/2002JB001771.
- [2] Angermann, D., J. Klotz, and C. Reigber (1999), *Space-geodetic estimation of the Nazca-South America Euler vector*, Earth Planet. Sci. Let: (171),3, 329-334.
- [3] Alt, J. C., J. Honnorez, C. Laverne, and R. Emmermann (1986), *Hydrothermal alteration of a 1 km section through the upper oceanic crust, Deep Sea Drilling Project Hole 504B: Mineralogy, chemistry, and evolution of seawater-basalt interactions*, J. Geophys. Res, 91, 10,309-10,335.
- [4] Au, D., and R.M. Clowes (1984), *Shear-wave velocity structure of the oceanic lithosphere from ocean bottom seismometers studies*, Geophys. J. R. astr. Soc, 77, 105-123.
- [5] Barrientos, S. E., and S. N. Ward (1990), *The 1960 Chile earthquake: Inversion for slip distribution from surface deformation*, Geophys. J. Int, 103, 589-598.
- [6] Bialas, J., and E. R. Flueh (1999), *Ocean bottom seismometers* Sea Technol, 40(4), 41-46.
- [7] Bangs, N. L., and S. C. Cande (1997), *Episodic development of a convergent margin inferred from structures and processes along the Southern Chile margin*. Tectonics, 16, 489-503.
- [8] Bourgois, J., C. Guivel, Y. Lagabrielle, T. Calmus, J. Boulague and V. Daux (2000), *Glacial-interglacial trench supply variation, spreading-ridge subduction, and feedback controls on the Andean margin development at the Chile triple junction area (45-48°S)*, J. Geophys. Res, 105(B4), 8355-8386.
- [9] Byrne, D. E., W. Wang, and D. M. Davis (1993), *Mechanical role of backstops in the growth of forearcs*, Tectonics, 12(1), 123-144.
- [10] Cande, S. C., and R. B. Leslie (1986), *Late Cenozoic tectonics of the southern Chile Trench*, J. Geophys. Res, 91, 471-496.

- [11] Carbotte, S., and D. S. Scheirer (2004), *Variability of ocean crustal structure created along the global mid-ocean ridge*, In E.E. Davis, H. Elderfield (Eds.), *Hydrogeology of Oceanic Lithosphere*, Cambridge University Press, 128-150.
- [12] Carlson, R.L., and D. J. Miller (2003), *Mantle wedge contents estimated from seismic velocities in partially serpentinized peridotites*, *Geophys. Res. Lett.*, 30 doi:10.1029/2002GL016600.
- [13] Carlson, R. L., and D. J. Miller (2004), *Influence of pressure and mineralogy on seismic velocities in oceanic gabbros: Implications for the composition and state of the lower oceanic crust*, *J. Geophys. Res.*, 109, B09205, doi:10.1029/2003JB002699.
- [14] Chapman, C.H., and J. A., Orcutt (1985), *The computation of body wave synthetic seismograms in laterally homogeneous media*, *Rev. Geophys.*, 23, 105-163.
- [15] Chapple W. M., and D. W. Forsyth (1979), *Earthquakes and bending plates at trenches*, *J. Geophys. Res.*, 84: 6729-6749.
- [19] Christensen, N. I (1996), *Poisson's ratio and crustal seismology*, *J. Geophys. Res.*, 101(B2), 3139-3156.
- [17] Christensen, N. I., and M. H. Salisbury (1975), *Structure and constitution of the lower oceanic crust*, *Rev. Geophys.*, 13, 57-86.
- [18] Christensen D. H., and L.J. Ruff (1983), *Outer-rise earthquakes and seismic coupling*, *Geophys. Res. Lett.*, 10: 697-700.
- [19] Christensen N. I., and M. H. Salisbury (1975), *Structure and constitution of the lower oceanic crust*, *Rev. Geophys.*, 13, 57-86.
- [20] Christensen N. I., and M. H. Salisbury (1979), *Seismic anisotropy in the oceanic upper mantle: evidence from the Bay of Islands ophiolite complex*, *J. Geophys. Res.*, 4601-4610.
- [21] Christensen N. I., and J. D. Smewing (1981), *Geology and seismic structure of the northern section of the Oman ophiolite*, *J. Geophys. Res.*, 86, 2545-2555.
- [22] Cifuentes, I. L. (1989), *The 1960 Chilean earthquakes*, *J. Geophys. Res.*, 94(B1), 665-680.
- [23] Cisternas, M., et al. (2005), *Predecessors of the giant 1960 Chile earthquake*, *Nature*, 437(15), 404-407, doi:10.1038/nature03943.
- [24] Clift, P., and P. Vannucchi (2004), *Controls on tectonic accretion versus erosion in subduction zones: Implications for the origin and recycling of the continental crust*, *Rev. Geophys.*, 42: RG2001, doi:10.1029/2003RG000127.



- [25] Clouard, V., J. Campos, A. Lemoine, A. Perez, and E. Kausel (2007), *Outer rise stress changes related to the subduction of the Juan Fernandez Ridge, central Chile* J. Geophys. Res., 112, B05305, doi:10.1029/2005JB003999.
- [26] Clowes, R.M., and D. Au (1982), *In-situ evidence for a low degree of S-wave anisotropy in the oceanic upper mantle*, Geophys. Res. Lett., 24, 1311-1314.
- [27] Collier, J.S., and S. C. Singh, (1998), *Poisson's ratio structure of young oceanic crust* J. Geophys. Res., 103(B9), 20981-20996.
- [28] Contreras-Reyes, E., I. Grevemeyer, E. R. Flueh, M. Scherwath, and M. Heese-  
mann (2007), *Alteration of the subducting oceanic lithosphere at the south-  
ern central Chile trench-outer rise*, Geochem. Geophys. Geosyst., 8, Q07003,  
doi:10.1029/2007GC001632.
- [29] Contreras-Reyes, E., I. Grevemeyer, E. R. Flueh, M. Scherwath, and J. Bialas (2008a),  
*Effect of trench-outer rise bending-related faulting on seismic Poisson's ratio and  
mantle anisotropy: a case study offshore of Southern Central Chile*, Geophys. J. Int,  
173, 142-156, doi:10.1111/j.1365-246X.2008.03716.x.
- [30] Contreras-Reyes, E., I. Grevemeyer, E. R. Flueh, and C. Reichert (2008b), *Upper  
lithospheric structure of the subduction zone offshore southern Arauco Peninsula,  
Chile at  $\sim 38^\circ S$* , J. Geophys. Res, doi:10.1029/2007JB005569, in press.
- [31] Davis, E. E. and R. D. Hyndman (1989), *Accretion and recent deformation of sedi-  
ments along the northern Cascadia subduction zone*, Geol. Soc. Am. Bull., 101, 1465-  
1480.
- [32] Davis, D. M., J. Suppe, and F. A. Dahlen (1983), *Mechanics of fold-and-thrust belts  
and accretionary wedges*, J. Geophys. Res, 88, 1153-1172.
- [33] Detrick, R. S., R. S. White, and G. M. Purdy (1993), *Crustal structure on North  
Atlantic fracture zones*, Rev. Geophys., 31(4), 439-458.
- [34] Diaz-Naveas, J. L (1999), *Sediment subduction and accretion at the Chilean convergent  
margin between  $35^\circ$  und  $40^\circ S$* , Ph.D. Thesis, Ch.-A.-Universität, Kiel, Germany.
- [35] Encinas, A., K. L. Finger, S. N. Nielsen, A. Lavenu, L. A. Buatois, D. E. Peterson  
and J. P. Le Roux (2008), *Rapid and major coastal subsidence during the late Miocene  
in south-central Chile*, J. South American Earth Sci, , (25), 2, 157-175.
- [36] DeMets, C., R. G. Gordon, D. F. Argus, S. Stein (1994), *Effect of recent revisions to  
the geomagnetic reversal time scale on estimates of current plate motions*, Geophys.  
Res. Lett., 21(20), 2191-2194, 10.1029/94GL02118.

- [37] Fisher, A. T., C. A. Stein, R. N. Harris, K. Wang, E. A. Silver, M. Pfender, M. Hutnak, A. Cherkaoui, R. Bodzin, and H. Villinger (2003a), *Abrupt thermal transition reveals hydrothermal boundary and role of seamounts within the Cocos plate*, *Geophys. Res. Lett.*, 30, 1550, doi: 10.1029/2002GL016766.
- [38] Fischer, A. T., E. E. Davis, M. Hutnak, V. Spiess, L. Zuehlsdorff, A. Cherkaoul, L. Christiansen, K. Edwards, R. Macdonald, H. Villinger, M. J. Mottl, C. G. Wheat, and K. Becker (2003b), *Hydrothermal recharge and discharge across 50 km guided by seamounts on a young ridge flank*, *Nature*, 421, 618-621.
- [39] Flueh, E. R., and J. Bialas (1996), *A digital, high data capacity ocean bottom recorder for seismic investigations* *Int. Underwater Syst. Design*, 18(3), 18-20.
- [40] Flueh, E.R., Koop,H., Schreckenberger, B (edts), (2002), *Subduction processes off Chile. Cruise Report, Geomar*.
- [41] Flueh, E. R., and I. Grevemeyer (2005), *TIPTEQ SONNE Cruise SO-181 (Eds.), from the Incoming Plate to mega Thrust EarthQuakes*, Geomar Rep. 102, Geomar, Kiel, Germany.
- [42] Fuchs, K., and G. Mueller (1971), *Computation of synthetic seismograms with the reflectivity method and comparison with observations*, *Geophys. J. R. astr. Soc.*, 23, 417-433.
- [43] Gill, J (1981), *Orogenic Andesites and Plate Tectonics EarthQuakes*, Springer, New York.
- [44] Gonzalez, E. (1989) *Hydrocarbon resources in the coastal zone of Chile*, in *Ericksen, G., et al., eds., Geology of the Andes and its relation to hydrocarbon and mineral resources: Houston, Texas, Circum-Pacific Council for Energy and Mineral Resources*, pp. 383-404.
- [45] Grevemeyer, I., and W. Weigel (1996), *Seismic velocities of the uppermost igneous crust versus age*. *Geophys. J. Int*, 124: 631-635.
- [46] Grevemeyer I., and W. Weigel (1997), *Increase of seismic velocities in upper oceanic crust: The "superfast" spreading East Pacific Rise at 14° 14'S.*, *Geophys. Res. Lett.*, 24: 217-220.
- [47] Grevemeyer, I., and A. Bartetzko (2004), *Hydrothermal ageing of oceanic crust: inferences from seismic refraction and bore hole studies*, In *E.E. Davis, H. Elderfield (Eds.)*, Cambridge University Press, pp:128-150.

- [48] Grevemeyer, I., W. Weigel, R. B. Whitmarsh, F. Avedik, G. A. Dehghani (1997), *The Aegir Rift: Crustal structure of an extinct spreading axis*, Mar. Geophys. Res, 19, 1-23.
- [49] Grevemeyer, I., Weigel W., and C. Jennrich (1998), *Structure and ageing of oceanic crust at 14°S on the East Pacific Rise*, Geophys. J. Int, 135, 573-584.
- [50] Grevemeyer, I., N. Kaul, H. Villinger, and W. Weigel (1999), *Hydrothermal activity and the evolution of the seismic properties of upper oceanic crust*, J. Geophys. Res, 104(B3), 5069-5080.
- [51] Grevemeyer, I., N. Kaul, J. L. Diaz-Naveas, H. Villinger, C. R. Ranero, C. Reichert (2005), *Heat flow and bending-related faulting at subduction trenches: case studies offshore of Nicaragua and Central Chile*, Earth Planet. Sci. Lett: 236, 238-248.
- [52] Grevemeyer, I., E. R. Flueh, C. R. Ranero, D. Klaeschen, J. Bialas (2007), *Passive and active seismological study of bending-related faulting and mantle serpentinization at the Middle America trench*, Earth Planet. Sci. Lett:doi:10.1016/j.epsl.2007.04.013.
- [53] Groß, K., U. Micksch, and TIPTEQ Research Group, Seismic Team (2007), *The reflection survey of project TIPTEQ-the inventory of the Chilean subduction zone at 38.2°S*, Geophys. J. Int, doi:10.1111/j.1365-246X.2007.03680.
- [54] Haberland, C., A. Rietbrock, D. Lange, K. Bataille, and S. Hofmann (2006), *Interaction between forearc and oceanic plate at the south-central Chilean margin as seen in local seismic data*, Geophys. Res. Lett., 33, L23302, doi:10.1029/2006GL028189.
- [55] Habermann, R. E., W. R. McCann, and B. Perin (1986), *Spatial seismicity variations along convergent plate boundaries*, Geophysical Journal of the Royal Astronomical society, 85, 43-68.
- [56] Hacker, B. R., S. M. Peacock, G. A. Abers, and S. D. Holloway (2003), *Subduction factory 2. Are intermediate-depth earthquakes in subducting slabs linked to metamorphic dehydration reactions?* J. Geophys. Res, 108(B1), 2030, doi:10.1029/2001JB001129
- [57] Hayward, N., G. K. Westbrook, and S. Peacock (1976), *Shear-wave velocity versus depth in marine sediments: a review*, Geophysics, 41(5), 985-996.
- [58] Hayward, N., G. K. Westbrook, and S. Peacock (2003), *Seismic velocity, anisotropy, and fluid pressure in the Barbados accretionary wedge from an offset vertical seismic profile with seabed sources*, J. Geophys. Res, 108(B11), 2515, doi:10.1029/2001JB001638.

- [59] Herve, F. E, F. Munizaga, M. A. Parada, M. Brook, R. Pankhurst, N. Spelling, and R. Drake (1988), *Ganitoids of the coast range of central Chile: Geochronology and geologic setting*, S. Am. Earth Sci. J., 1, 185-194.
- [60] Herron, E. M., S. C. Cande, and B. R. Hall (1981), *An active spreading center collides with a subduction zone, a geophysical survey of the Chile margin triple junction*, Geological Society of America Memories, G Vol. 154, p. 683-701.
- [61] Hess, H. H., (1962), *History of ocean basins*, in *Petrological Studies: A Volume in Honor of A. F. Buddington*, edited by A.E. Engel, H.L. James, and B. F. Leonard, pp. 599-620, Geol. Soc. of Am., Boulder, Colo.
- [62] Hyndman, R. D., (1979), *Poisson's ratio in the oceanic crust: a review*, Tectonophysics, 59, 321-333.
- [63] Jung, H., and S. Karato, (2001), *Water-induced fabric transitions in Olivine*, Science, 293, 1460-1463.
- [64] Ivandic, M., I. Grevemeyer, A. Berhorst, E. R. Flueh, and K. McIntosh (2008), *Impact of bending related faulting on the seismic properties of the incoming oceanic plate offshore of Nicaragua*, J. Geophys. Res, in press.
- [65] Kaizuka, S., T. Matsuda, M. Nogami and N. Yonekura (1973), *Quaternary tectonic and recent seismic crustal movements in the Arauco Peninsula and its environs, central Chile*, Geographical Report vol. 8, Tokyo, Metropolitan University, Tokyo, 1-49, 1973.
- [66] Kanamori, H (1971), *Seismological evidence for lithospheric normal faulting: the Sanriku earthquake of 1933*, Phys. Earth planet. Inter. 4: 289-300.
- [67] Karson, J. A (1998), *Internal structure of oceanic lithosphere: A perspective from tectonic windows*, in *Faulting and Magmatism at Mid-Ocean Ridges*, edited by W. R. Buck et al., Geophys. Monogr. Ser., vol. 106, pp. 177-218, AGU, Washington, D. C.
- [68] Kirby, S., E. Engdahl, and R. Denlinger (1996), *Intermediate-depth intraslab earthquakes and arc volcanism as physical expressions of crustal and uppermost mantle metamorphism in subducting slabs*, in *Subduction: Top to Bottom*, Geophys. Monogr. Ser., vol. 106, pp. 195-214, AGU, Washington, D. C.
- [69] Kitamura et al. (2005), *Melange and its seismogenic roof decollement: A plate boundary fault rock in the subduction zone-An example from the Shimanto Belt, Japan*, Tectonics, 24, TC5012, doi:10.1029/2004TC001635.

- [70] Korenaga, J., W. S. Holbrook, G. M. Kent, P. B. Kelemen, R. S. Detrick, H.-C. Larsen, J. R. Hopper, and T. Dahl-Jensen (2000), *Crustal structure of the southeast Greenland margin from joint refraction and reflection seismic tomography*, J. Geophys. Res., 104(B3), 105, 21,591-21,614.
- [71] Kopp, H., and N. Kukowski (2003), *Backstop geometry and accretionary mechanics of the Sunda margin*, Tectonics, 22(6), 1072, doi:10.1029/2002TC001420.
- [72] Kopp, C., J. Fruehn, E.R. Flueh, C. Reichert, N. Kukowski, J. Bialas and D. Klaeschen (2000), *Structure of the Makran subduction zone from wide-angle and reflection seismic data*, Tectonophysics, (329), 171-191.
- [73] Kopp, H., E. R. Flueh, C. Papenberg, and D. Klaeschen (2004), *Seismic investigations of the O'Higgins Seamount Group and Juan Fernandez Ridge: Aseismic ridge emplacement and lithosphere hydration*, Tectonics, 23, TC2009, doi:10.1029/2003TC001590.
- [74] Krawczyk C. M., SPOC Team (2003), *Amphibious seismic survey images plate interface at 1960 Chile earthquake*, EOS, 84(32):301, 304-305.
- [75] Krawczyk et al., (2006), *Geophysical signatures and active tectonics at the south-central Chilean margin*, In: The Andes - active subduction orogeny, Editors: Oncken, O, et al. Frontiers in Earth Sciences, Springer Press, Berlin, Heidelberg, pp. 171-192.
- [76] Lallemand, S. E., P. Schnuerle, and J. Malavieille (1994), *Coulomb theory applied to accretionary and nonaccretionary wedges: Possible causes for tectonic erosion and/or frontal accretion*, J. Geophys. Res, 99(B6), 12,033-12,056.
- [77] Lefeldt, M., and I. Grevemeyer (2008), *Centroid depth and mechanism of trench-outer rise earthquakes*, Geophys. J. Int, 172, 240-251.
- [78] Lewis, B. T. R., and J. McClain, (1977), *Converted shear waves as seen by ocean bottom seismometers and surface buoys*, Bull. seism. Soc. Am., 67, 1291-1302.
- [79] Masson, D.G (1991), *Fault patterns at outer trench walls*, Mar. Geophys. Res., 13, 209-225.
- [80] McClain, J. S., and C.A. Atallah (1986), *Thickening of oceanic crust with age*, Geology, 14, 574-805.
- [81] Mithal R., and J. C. Mutter, (1989), *A low-velocity zone within the layer 3 region of 118 Myr old oceanic crust in the western North Atlantic*, Geophys. J., 97, 275-294.
- [82] Melnick, D., and H. Echtler (2006), *Inversion of forearc basins in south-central Chile caused by rapid glacial age trench fill*, Geology, 34 (9), 709-712.

- [83] Mikumo, T., Y. Yagi, S.K. Singh, and M. A. Santoyo (2002), *Coseismic and postseismic stress changes in a subducting plate: Possible stress interactions between large interplate thrust and intraplate normal-faulting earthquakes*, J. Geophys. Res, 107(B1), 2023, doi:10.1029/2001JB000446.
- [84] Moore, G. F., T. H. Schiopley, P. L. Stoffa and D. E. Karig (1990), *Structure of the Nankai Through Accretionary Zone from Multichannel Seismic Reflection Data*, J. Geophys. Res, 95(B6), 8753-8765.
- [85] Mordohovich, C (1974), *Geology of a part of the Pacific margin of Chile*, In:C.A. Burk and C.L. Drake, eds., *The geology of continental margins*: New York, Springer Verlag, p. 591-598.
- [86] Mueller, S., G. L. Choy, and W. Spence (1996a), *Inelastic models of lithospheric stress-I. Theory and application to outer-rise plate deformation*, Geophys. J. Int, 125 (1), 39-53 doi:10.1111/j.1365-246X.1996.tb06533.x
- [87] Mueller, S., W. Spence, and G. L. Choy (1996b), *Inelastic models of lithospheric stress-11. Implications for outer-rise seismicity and dynamics*, Geophys. J. Int, 125 (1) , 54-72 doi:10.1111/j.1365-246X.1996.tb065
- [88] Mueller, R. D., W. R. Roest, J.-Y. Royer, L. M. Gahagan, and J. G. Sclater (1997), *Digital isochrons of the world's ocean floor*, J. Geophys. Res, 102(B2), 3211-3214.
- [89] Nelson A. R., and W. F. Manley (1992), *Holocene coseismic and aseismic uplift of Isla Mocha, south-central Chile. Impacts of tectonics on Quaternary coastal evolution*, Quaternary International, 15-16, 61-76.
- [90] Nicolas, A., and N. Christensen (1987), *Composition, Structure and Dynamics of the Lithosphere-Asthenosphere*, System eds Fuchs, K. & Froidevaux, C., pp. 111-123, Am. Geophys. Union, Washington, DC.
- [91] Peacock, S. M (1990), *Fluid processes in subduction zones*, Science, 248, 329-337.
- [92] McClain, J. S., and C. A. Atallah (2001), *Are the lower planes of double seismic zones caused by serpentine dyhydration in subducting oceanic mantle?*, Geology, 29, 299-302.
- [93] Peacock, S. M (2004), *Insight into the hydrogeology and alteration of oceanic lithosphere based on subduction zones and arc volcanism*, In *E.E. Davis, H. Elderfield (Eds.)*, Cambridge University Press, pp: 659-676.
- [94] Precliz, R. M (2005), *Seismic anisotropy in peridotites from the Western Gneiss Region (Norway), laboratory measurements at high PT conditions and fabric based model predictions*, PhD thesis, Swiss Federal Institute of Technology Zurich, Switzerland.

- [95] Ranero, C. R., and V. Sallares (2004), *Geophysical evidence for alteration of the crust and mantle of the Nazca Plate during bending at the north Chile trench*, *Geology*, 32, 549-552.
- [96] Ranero, C. R., J. Phipps Morgan, K. McIntosh, and C. Reichert (2003), *Bending, faulting, and mantle serpentinization at the Middle America trench*, *Nature*, 425, 367-373.
- [97] Ranero, C. R., A. Villaseñor, J. Phipps Morgan, and W. Weinrebe (2005), *Relationship between bend-faulting at trenches and intermediate-depth seismicity*, *Geochem. Geophys. Geosyst.*, 6, Q12002, doi:10.1029/2005GC000997.
- [98] Ranero, C. R., R. von Huene, W. Weinrebe, and C. Reichert (2006), *Tectonic Processes along the Chile Convergent Margin*, In: Oncken, O., Chong, G., Franz, G., Giese, P., Götze, H.-J., Ramos, V., Strecker, M., Wigger, P. (eds): *The Andes - Active Subduction Orogeny*. *Frontiers in Earth Sciences*, vol. 1, XXII, 570pp, Springer, Berlin, Heidelberg.
- [99] Rauch (2005), *Cyclicality of Peru-Chile trench sediments between 36° and 38°S: A footprint of paleoclimatic variations?*, *Geophys. Res. Lett.*, 32, L08302, doi:10.1029/2004GL022196.
- [100] Reichert, C., B. Schreckenberger, and SPOC Team (2002), *Fahrtbericht SONNE-Fahrt SO-161 Leg 2 and 3 SPOC, Subduktionsprozesse vor chile-BMBF-Forschungsvorhaben 03G0161A- Valparaiso 16.10.2001-Valparaiso 29.11.2001*, Bundesanstalt für Geowissenschaften und Rohstoffe, Hannover, Germany.
- [101] Ruepke, L. R., Morgan, J. P., Hort, M., and J. A. D. Connolly (2004), *Serpentine and the subduction zone water cycle*, *Earth Planet. Sci. Lett.*, Vol 223, 1-2, 17-34.
- [102] Sallares, V., and C. R. Ranero (2005), *Structure and tectonics of the erosional convergent margin off Antofagasta, north Chile (23° 30'S)*, *J. Geophys. Res.*, 110, B06101, doi:10.1029/2004JB003418.
- [103] Salisbury, M. H., and Christensen, N. I (1978), *The seismic velocity structure of a traverse through the Bay of Islands ophiolite complex, Newfoundland: an exposure of oceanic crust and upper mantle*, *J. Geophys. Res.*, 83(2), 805-817.
- [104] Savage, J. C., (1969), *The mechanics of deep-focus faulting*, *Tectonophysics*, 8, 115-127.
- [105] Scherwath, M., E. R. Flueh, I. Grevemeyer, F. Tilmann, E. Contreras-Reyes, and R. W. Weinrebe (2006a), *Investigating Subduction Zone Processes in Chile*, *EOS Transactions*, 87, Nr. 27, 265-272.

- [106] Scherwath, M., E. Contreras-Reyes, I. Grevemeyer, E. R. Flueh, R. W. Weinrebe, and the TIPTEQ Working Group (2006b): *Structural images of the Southern Chile subduction zone system offshore*, *European Geosciences Union (Veranst.)*, Geophysical Research Abstracts, (3rd EGU General Assembly Vienna 02.-07. April 2006b). Bd.8.
- [107] Scherwath, M., E. Contreras-Reyes, I. Grevemeyer, E. R. Flueh, W. Weinrebe, and TIPTEQ Research Group (2007), *Upper lithosphere structure of the subduction zone in southern Chile- comparison of differently aged incoming plate*, *Geophysical Research Abstracts*, 9, S.06798.
- [108] Seno, T., and Y. Yamanaka (1996), *Double seismic zones, compressional deep trench-outer rise events and superplumes*, in *Subduction: Top to Bottom*, *Geophys. Monogr. Ser.*, vol. 96, edited by G. Bebout et al., pp.347-355, AGU, Washington, D. C.
- [109] Shaw, P. R., (1994), *Age variations of oceanic crust Poisson's ratio: inversion and a porosity evolution model*, *J. Geophys. Res.*, 99(B2), 3057-3066.  
Shearer, P. M., (1988), *Synthetic seismogram modeling of shear-wave splitting in VSP data from the Geysers, California*, *Geophys. Res. Lett.*, 15(10), 1085-1088.
- [110] Spudich, P. and J. A. Orcutt (1980), *Petrology and Porosity of an oceanic crustal site: results from wave form modelling of seismic refraction data*, *J. Geophys. Res.*, 81(5), 899-904.
- [111] Ulmer, P., and V. Trommsdorff (1995), *Serpentine stability to mantle depths and subduction-related magmatism*, *Science*, 268, 858-861.
- [112] Takei, Y., (2002), *Effect of pore geometry on  $V_P/V_S$ : FROM equilibrium geometry to crack*, *J. Geophys. Res.*, 107(B2), 2043, doi:10.1029/2001JB000522.
- [113] Tarantola, A (1987), *Inverse Problem Theory: Methods for Data Fitting and Model Parameter Estimation*, 613 pp., Elsevier, New York.
- [114] Tebbens, S. F., S. C. Cande, L. Kovacs, J. C. Parra, J. L. LaBrecque and H. Vergara (1997), *The Chile ridge: A tectonic framework*, *J. Geophys. Res.*, 102(B6), 12035-12060, doi: 10.1029/96JB02581.
- [115] Thornburg, T. M., and D. M. Kulm (1987), *Sedimentation in the Chile Trench: Depositional morphologies, lithofacies, and stratigraphy*, *Geol. Soc. Am. Bull.*, 98, 33-52.
- [116] Thornburg, T. M., D. M. Kulm, and D. M. Hussong (1990), *Submarine-fan development in the southern Chile trench: a dynamic interplay of tectonics and sedimentation*, *Geol. Soc. Am. Bull.*, 102, 1658-1680.



- [117] Tibi, R., G. Bock, and C. H. Estabrook (2002), *Seismic body wave constraint on mechanisms of intermediate-depth earthquakes*, J. Geophys. Res, 107, 101029/2001JB000361.
- [118] Tilmann, F. J., Grevenmeyer, I, Flueh, E. R., T. Dahm, and J. Gossler (2008), *Seismicity in the outer rise offshore southern Chile: indication of fluid effects in crust and mantle*, Earth Planet. Sci. Let: (in press).
- [119] Toomey, D. R., and G. R. Foulger (1989), *Tomographic inversion of local earthquake data from the Hengill-Grensdalur central volcano complex, Iceland*, J. Geophys. Res, 94, 17,497-17,510.
- [120] Trummer, I., (2002), *S-wave processing and interpretation of wide-angle seismic refraction data, Malpelo ridge, eastern Panama basin*, PhD thesis, Christian-Albrechts University, Kiel, 40-44 pp.
- [121] Turcotte, D., and G. Schubert (1982), *Geodynamics-Applications of Continuum Physics to Geological Problems*, John Wiley, Hoboken, N. J.
- [122] van Avendonk, H. J. A., A. J. Harding, and J. A. Orcutt (1998), *A two-dimensional tomographic study of the Clipperton transform fault*, J. Geophys. Res, 103, 17,885-17,899.
- [123] van Avendonk, H. J. A., A. J. Harding, J. A. Orcutt, and J. S. McClain (2001), *Contrast in crustal structure across the Clipperton transform fault from travel time tomography*, J. Geophys. Res, 106(B6), 10,961-10,982.
- [124] Vera, E. E., J. C. Mutter, P. Buhl, J. A. Orcutt, A. J. Harding, M. E. Kappus, R. S. Detrick and T. M. Brocher (1990), *The structure of 0- to 0.2-m.y.-old oceanic crust at 9°N on the East Pacific Rise from expanded spread profiles*, J. Geophys. Res, 95(B10), 15529-15556, doi:10.1029/90JB00230.
- [125] Villinger, H., I. Grevenmeyer, N. Kaul, J. Hauschild, M. Pfender (2002), *Hydrothermal heat flux through aged oceanic crust: where does the heat escape?*, Earth Planet. Sci. Let: 202 159-170.
- [126] Voelker, D, M., S. Wiedicke, C. Ladage, C. Gaedicke, C. Reichert, K. Rauch, W. Kramer, and C. Heubeck, (2006), *Latitudinal variation in sedimentary processes in the Peru-Chile Trench off Central Chile. In: The Andes - active subduction orogeny,*, Editors: Oncken, O, et al. Frontiers in Earth Sciences, Springer Press, Berlin, Heidelberg, p. 193-216.
- [127] von Huene, R., Corvalán, J., Flueh, E.R., Hinz, K., Korstgard, J., Ranero, C. R., Weinrebe, W., and the CONDOR Scientists (1997). *Tectonic Control of the subducting*

- Juan Fernández Ridge on the Andean margin near Valparaíso, Chile.* *Tectonics*, 16 (3), 474 - 488.
- [128] von Huene, R., and D.W. Scholl (1991), *Observations at convergent margins concerning sediment subduction, subduction erosion, and the growth of continental crust*, *Rev. Geophys.*, 29(3), 279-316, doi:10.1029/90JB00230.
- [129] von Huene, R., L. D. Kulm, and J. Miller (1985), *Structure of the frontal part of the Andean convergent margin*, *J. Geophys. Res.*, 90(7), 5429-5442.
- [130] Walter, C., E. R. Flueh, C. R. Ranero, R. von Heune, W. and Strauch, (2000) *Crustal structure across the Pacific margin of Nicaragua: evidence for ophiolitic basement and a shallow mantle sliver*, *Geophys. J. Int.*, 141, 759-777.
- [131] White, R. S., D. McKenzie, and R. K. O’Nions (1992), *Oceanic crustal thickness from seismic measurements and rare earth element inversions*, *J. Geophys. Res.*, 97, 19,683-19,715.
- [132] Wilkens, R. H., G. J. Fryer, J. Karsten (1991), *Evolution of porosity and seismic structure of upper oceanic crust: Importance of aspect ratios*, *J. Geophys. Res.*, 97(B6), 9297-9305.
- [133] Wilkens, R. H., C. H. Cheng, and J. A. Meredith (1992), *Evaluation and prediction of shear wave velocities in calcareous marine sediment and rocks*, 97(B6), 9297-9305.
- [134] Yáñez, G., C. R. Ranero, and J. Díaz (2001), *Magnetic Anomaly interpretation across the southern central Andes (32° – 34°S): The role of the Juan Fernández Ridge in the late Tertiary evolution of the margin*. *J. Geophys. Res.*, 106 (B4), 6325 - 6345.
- [135] Yuan, X., et al. (2000), *Subduction and collision processes in the Central Andes constrained by converted seismic phases*, *Nature*, 408, 958-961.
- [136] Zelt, C. A, and R. B. Smith (1992), *Seismic travelttime inversion for 2-D crustal velocity structure*. *Geophys. J. Int.*, 108, 16-34.
- [137] Zhang, S. and Karato, S., (1995), *Lattice preferred orientation of olivine deformed in simple shear*, *Nature*, 375, 774-777, doi:10.1038/375774a0.

# Acknowledgments

I would like to thank PD. Dr. Ingo Grevemeyer for his valuable scientific guidance, motivation, positiveness, support, time and mainly for appreciation of my work. I thank Prof. Dr. Ernst R. Flüh who provided helpful discussions which often clarified important aspects of seismic modeling, and for his positive assessment of my results, and my work in general.

I am very grateful to Martin Scherwath for his advices, constructive comments and revision of my manuscripts. I thank Prof. Dr. Wolfgang Rabbel for inmediately agreeing to act as co-referee.

This dissertation was financed by the German Academic Exchange Service (DAAD). The support from DAAD is gratefully acknowledged not only for giving me the opportunity to become a Doctor, but also for having the experience to live in Germany. I am very thankful to Mrs. Maria Hartmann for her help, specially in the beginning of my PhD.

Cesar Ranero, Frederik Tilmann, Heidriun Kopp, David Völker, Andrés Tassara, Arnim Berhorst, Daniel Melnick, Juan Diaz-Naveas and Lars Planert helped me with tectonic interpretation and seismic modeling, many thanks for their discussions. Special thanks to Eduard Mezhyrov and Wilhelm Weinrebe for the computing assistance.

I am grateful to Masters Kull and Mallon and their officers and crew of R/V Sonne and all scientists who assisted in data collection during cruise SO181, from which I got a valuable high quality data set. The financial support was provided by the German GEOTECHNOLOGIEN program jointly funded by the German Ministry of Education, Science, Research, and Technology (BMBF) and German Science Foundation (DFG).

My best thanks to my PhD mates David Pesquer, Markus Fink, Alexey Shulgin, Jun-jiang Zhu, Andreas Wittwer, Anke Danowsky, Ivone Arroyo, Wendy Perez and Monika Ivandic. Thanks for the nice times lived over the past years in Kiel. The time that I spent in Germany was also a good chance to meet nice people from all over the world. I thank

the company of Anthony Nonciaux, Andre Terwei, Björn Mildahn, Jürgen Gossler, Michal Wójcicki, Eduardo "Pajarito" Rodriguez, Michal Kolodziejcki, Carlos Rivas, Tomke Gottschlich, Kerstin Hesse, Yvonne Verlinde, Claudia Grötschel, Manuela Meyer, Daniel Matias, and many others. I thank them for the nice and unforgettable times lived in Europe.

I would also like to mention all my friends in Chile who encouraged and motivated me for carrying out this PhD: Diego Olivares, Mark Falvey, Juan Riquelme, Andres Massa, Rene Alvarado, Lucia Villar, Sergio Contreras-González, Mauricio Olea, Ulises Vazquez and Felipe Orellana. I want also to express my acknowledgments to Emilio Vera, who was my supervisor during my Master thesis at the Department of Geophysics in Santiago de Chile. I thank him for teach me and properly prepare me for my Doctoral studies in Germany.

Finally, I want to express my best thanks to my family: Digna Reyes (Mother), Eliseo Contreras (Father), Carolina Contreras-Reyes (Sister) and Javier Contreras-Reyes (Brother). I thank them for their unconditional love, positiveness, and moral support specially in the hardest times. I am very thankful to my parents to facilitate my initiation in Geosciences, and I dedicate this PhD thesis to them.

*Muchas gracias por todo, un abrazo fuerte a la distancia. !!!*

**Eduardo**

# Eidesstattliche Erklärung

Hiermit erkläre ich, daß die von mir für das Promotionsverfahren vorgelegte Abhandlung "*Evolution of the Seismic Structure of the Incoming/Subducting Oceanic Nazca Plate off South Central Chile*", abgesehen von der Beratung der Betreuer nach Inhalt und Form, meine eigene Arbeit ist. Bisher ist die Arbeit noch nicht an anderer Stelle im Rahmen eines Prüfungsverfahrens vorgelegt worden.

Eduardo Contreras-Reyes.



# Curriculum Vitae

Name: Eduardo Eliseo Contreras Reyes

Date and Place of birth: 14<sup>th</sup> of September 1977 in Santiago de Chile

Citizenship: Chilean

1997-2002: B.Sc. in Geophysics, Universidad de Chile

2002-2003: M.Sc. in Geophysics, Universidad de Chile

2004: Research Assistant at the Centre Mathematics for Modelling (CMM), Universidad de Chile

since April, 2005: PhD Student at the Leibniz-Institute of Marine Sciences IFM-GEOMAR at the University of Kiel, Germany